The Thesis Committee for Eric Youngwoong Kim

Certifies that this is the approved version of the following thesis:

INVESTIGATION OF CO_2 SEEPS AT THE CRYSTAL GEYSER SITE USING NUMERICAL MODELING WITH GEOCHEMISTRY

Approved by

Supervising Committee:

_____

Sanjay Srinivasan, Supervisor

_____

Peter Eichhubl

INVESTIGATION OF CO_2 SEEPS AT THE CRYSTAL GEYSER SITE USING NUMERICAL MODELING WITH GEOCHEMISTRY

by

Eric Youngwoong Kim, B.S.

Thesis

Presented to the Faculty of the Graduate School of

The University of Texas at Austin

in Partial Fulfillment

of the Requirements

for the Degree of

Masters of Science in Engineering

The University of Texas at Austin

May 2012

Dedication

This thesis is dedicated to my loving family.

Acknowledgements

This thesis is based upon work supported as part of the Center for Frontiers of Subsurface Energy Security, an Energy Frontier Research Center funded by the U.S. Department of Energy, Office of Science, Office of Basic Energy Sciences under Award Number DESC0001114.

I would like to express my sincere gratitude to my supervising professor, Dr. Sanjay Srinivasan. His inspiration and guidance helped me to learn and explore new ideas, challenge unsolved problems, and gain valuable experiences. I feel very fortunate for getting the opportunity to work with him and I sincerely appreciate his supervision, advice and motivation throughout my time at the University of Texas at Austin.

I would also like to express my thanks to my committee member, Peter Eichhubl, for his suggestions and advices. His thoughtful reviews and comments have been very helpful for my research.

I am very thankful to all the renowned faulty members at the University of Texas at Austin for the learning experience and sharing their knowledge with me. I would like to thank Dr. Bommer and Dr. De Regge for assistances. I would like to thank all the staff members for their help and support: Arletta Tompkins, Cheryl Kruzie, Erin Gandy, Frankie Hart, Jin Lee, and Dr. Roger Terzian. I am also pleased to acknowledge the support of CMG Ltd. for the simulation software.

I would like to express my gratitude to all my friends for their love and sharing unforgettable memories with me. I would like to thank to my dearest friend, Yuri Song, for her support. I would like to thank to Galen Kragas, HoonYoung Jeong, and Jonathan Lee for their friendship and support. I would also like to thank my colleagues, Doohyun Chung, Jongsoo Hwang, Changmin Jung, Heesong Koh, Dongkeun Lee, Hunjoo Lee, Hyungjoo Lee, Kwangjin Lee, and Kyunghaeng Lee for sharing unforgettable memories with me over the last two years.

I greatly appreciate my research group and officemates, Sayantan Bhowmik, Harpreet Singh, Selin Erzybek, Travis Hampton, Brandon Henke, Dhananjay Kumar, Aarti Punase, and Prince Azom for valuable discussions and chats.

Lastly, I would like to express my sincere thanks to my family, Yong Tae Kim, Soon Ok Kim, Young Joo Kim, and Michelle Kim, for their never-ending support and love. Without doubt, I would not have made it through this far without them.

Abstract

INVESTIGATION OF CO_2 SEEPS AT THE CRYSTAL GEYSER SITE USING NUMERICAL MODELING WITH GEOCHEMISTRY

Eric Youngwoong Kim, M.S.E.

The University of Texas at Austin, 2012

Supervisor: Sanjay Srinivasan

Carbon Dioxide (CO_2) sequestration requires that the injected CO_2 be permanently trapped in the subsurface and not leak from the target location. To accomplish this, it is important to understand the main mechanisms associated with CO_2 flow and transport in the subsurface once CO_2 is injected. In this work CO_2 seeps at the Crystal Geyser site were studied using modeling and simulation to determine how CO_2 geochemically reacts with formation brines and how these interactions impact the migration of CO_2. Furthermore different scenarios for CO_2 migration and seepage along the Grand Wash fault are studied and the possible outcomes for these different scenarios are documented. The GEM (Generalized Equation-of-State Model) from CMG Ltd. was used to perform the simulation studies. A 2-D model was built without geochemical reactions to mainly study the mechanism associated with dissolution of CO_2 gas. The process of CO_2 release from the brine as the fluid mixture flows up along the fault was modeled. Then, 3-D models with geochemical reactions were built for CO_2 migration corresponding to two different sources of CO_2 - deep crustal CO_2 and CO_2-dissolved in groundwater. In both these cases, CO_2 reacted with the aqueous components and minerals

of the formation and caused carbonate mineralization. In the case of deep crustal CO_2 source, there were vertical patterns of calcite mineralization simulated along the fault that indicated that calcite mineralization might be localized to isolated vertical flow paths due to vertical channeling of CO_2 from the crust. In the case of CO_2-dissolved groundwater flowing along the sandstone layers, calcite mineralization is spread over the entire fault surface. In this case, the groundwater flow is interrupted by the fault and there is vertical flow along the fault until a permeable sandstone layer is encountered on the other side of the fault. This vertical migration of CO_2-saturated brine causes a release in pressure and subsequent ex-solution of CO_2. As a result, modeling allowed us to establish difference in surface expression of CO_2 leakage due to two different CO_2 migrations scenarios along the fault and helped develop a scheme for selecting appropriate model for CO_2 leakage based on surface observation of travertine mounds.

A key observation at the Crystal Geyser site is the lateral migration of CO_2 seep sites over time. These migrations have been confirmed by isotope studies. In this modeling study, the mechanism for migration of seep sites was studied. A model for permeability reduction due to precipitation of calcite was developed. It is shown using percolation calculations that flow re-routing due to permeability alterations can result in lateral migration of CO_2 seeps at rates comparable to those established by isotope dating.

Table of Contents

List of Tables

List of Figures

Chapter 1 : Introduction

1.1 Overview

With large amounts of Carbon Dioxide (CO_2) in the atmosphere from emissions and consequential problems such as a rise in temperature around the globe, many methods have been proposed to reduce atmospheric CO_2. One of the most viable methods is to sequester CO_2 in the subsurface. Injecting CO_2 under supercritical condition into saline aquifers can possibly store a significant amount of atmospheric CO_2 in the subsurface for a long period. There are many potential sites for CO_2 storage such as depleted oil and gas reservoirs and deep aquifers. However, a general lack of knowledge about CO_2 transport mechanisms in the subsurface is one of the main source of concern about CO_2 sequestration; namely, the migration of injected CO_2 may not behave as predicted and consequently, it may not be trapped permanently. Therefore, it is important to understand the main CO_2 transport mechanisms in the subsurface.

There are different types of mechanisms involved in CO_2 sequestration such as mineral trapping (Ghanbarnezhad, 2011). In mineral trapping, the injected CO_2 dissolves in aquifer brine and reacts with rock minerals which typically dissolve carbonates. Then, these carbonates precipitate subsequently because of changes in the pH condition. The precipitated carbonate reduces the permeability of the rock formation and traps CO_2. Many laboratory experiments and simulation studies have attempted to understand the impact of geochemistry on CO_2 transport in the subsurface and on sequestration (Perkins and Gunter, 1995; Nghiem, 2004; Druckenmiller, 2005; Johnson, 2004; Xu et al., 2001; Mito et al., 2008). Leakages of CO_2 gas have been observed on the surface as a possible result of mineral trapping of CO_2. Several CO_2-charged geysers and evidence of calcite precipitations in forms of travertine mounds around the geysers have also been reported. Thus, many studies have focused on the cause of the phenomena and to identify potential leakage scenarios (Moore et al., 2004; Heath et al., 2008). This thesis focuses on modeling CO_2 gas emissions from seeps at the Crystal Geyser site in Utah and numerically modeling potential leakage scenarios to link with actual events in the field. This allows us to predict the main mechanisms of CO_2 transport in subsurface and the

role of the fault system in the activity of geysers at this site. Significant uncertainties and a lack of understanding about the observations of CO_2 seeps remain such as the source of the CO_2 and the properties of the fault fill material. Modeling these uncertainties and attempting to calibrate them against field observations are essential for understanding the primary factors that controls the subsurface migration and potential leakage of CO_2 from storage sites. This study provides much needed information on CO_2 transport mechanism in the subsurface and ultimately the CO_2 sequestration process.

1.2 Research Objectives

The objective of this research is to model and investigate the mechanisms controlling the spatial and temporal observations of CO_2 seeps at the Crystal Geyser site in Utah using the flow reservoir simulator, GEM (Generalized Equation-of-State Model). Different hypotheses about the source of the CO_2 are presumed and incorporated into the simulator. The behavior of CO_2 leakage along the fault and its effects on the surface expression of CO_2 seeps are studied. A geostatistical approach is used to determine the uncertain fault properties such as permeability and model the fault system. The fault properties are also altered for sensitivity studies. The modeling also includes aspects of geochemistry associated with CO_2 interaction with minerals. Important effects such as the lateral migration of CO_2 seeps due to plugging of pore space by precipitation of chemicals are investigated and an attempt is made to understand if such flow diversion can cause migration of seeps at geological time scales established by isotope studies.

1.3 Thesis Outline

Chapter 2 presents a literature review of the previous works on the mechanisms of CO_2 transport in the subsurface including numerical modeling of laboratory experiments. Previous field studies investigating CO_2-driven geysers at natural CO_2 storage sites are also reviewed. Chapter 3 gives a description of the materials and methods used in

modeling the Grand Wash fault system at the Crystal Geyser site. The geology of the field site is described. Also, the geochemical model used in the numerical model is explained.

Chapter 4 illustrates CO_2 gas release mechanism along the fault and a sensitivity study by varying the fault properties in a cross-sectional model. Chapter 5 demonstrates CO_2 flow and transport in subsurface and the results corresponding to two scenarios of CO_2 source in 3-D model. In Chapter 6, the mechanism for flow diversion due to plugging of pore space by chemical precipitate is investigated. In Chapter 7, conclusions and key findings drawn from the research studies and suggestions for future work are presented.

Chapter 2 : Literature Review

2.1 Overview

In this chapter, the literature and previous research related to the proposed theories, experimental laboratories, and simulation and field studies of natural CO_2 sequestration analogs is reviewed. First, relevant subsurface mechanisms proposed at these sites and involved geochemical reactions are discussed. Then, previous studies that present various interpretations of subsurface mechanisms associated with CO_2 are reviewed. Finally, the literature specifically related to CO_2-driven geyser activities is reviewed to gain a better understanding of the phenomenon.

2.2 Mechanism of CO_2 Sequestration: Mineral Trapping

CO_2 sequestration process, which captures and stores the carbon dioxide (CO_2) in the subsurface, has become one of the most viable methods for reducing the greenhouse gas effect because it has many advantages over alternative methods such as low costs and capability to remove large amounts of atmospheric CO_2. Various subsurface mechanisms for CO_2 sequestration process are proposed in the literature; one of the most controversial mechanisms is mineral trapping. When CO_2 is injected in a saline aquifer, it dissolves in the aquifer and reacts with rock minerals to form calcite. At a certain pH condition, the calcite precipitates and this results in the mineral trapping mechanism by reducing rock permeability and trapping the injected CO_2. CO_2 sequestration with mineral trapping involves numerous geochemical reactions and there have been a surprising number of studies devoted to the specialized topic of geochemical reactions associated with CO_2 in different environments and their possible outcomes. In the following section, previous studies on geochemical reactions associated with CO_2 migration in the subsurface are reviewed.

2.2.1 Geochemical Reactions

Table 2-1 shows one of the most frequently suggested geochemical reactions associated with the mineral trapping mechanism; CO_2 gas dissolves in brine and carbonic

acid forms. This further dissociates into bicarbonates and carbonate ions that react with Ca, Mg, and Fe to form mineral precipitations such as calcite, dolomite, and magnesite. However, the actual geochemical reactions that may happen in the subsurface vary because these reactions could be affected by many other factors including pH of the system, rock and brine compositions, minerals, temperature, and pressure (Druckenmiller et al., 2005).

$$CO_2(g) \rightleftarrows CO_2(aq)$$
$$CO_2(aq) + H_2O \rightleftarrows H_2CO_3$$
$$H_2CO_3 \rightleftarrows H^+ + HCO_3^-$$
$$HCO_3^- \rightleftarrows H^+ + CO_3^{2-}$$
$$Ca^{2+} + CO_3^{2-} \rightleftarrows CaCO_3$$
$$Mg^{2+} + CO_3^{2-} \rightleftarrows MgCO_3$$
$$Ca^{2+} + Mg^{2+} + CO_3^{2-} \rightleftarrows CaMg(CO_3)_2$$

Table 2-1. Suggested geochemical reactions in mineral trapping.

Different geochemical reactions involved in mineral trapping have been outlined by a number of researchers. Johnson et al. (2004) studied CO_2 storage in a shale-capped sandstone aquifer. They suggested that dawsonite precipitation and cementation take place with dissolution of K-feldspar which reduces the shale porosity and permeability. The reaction equation is the following;

$$\text{K-feldspar} + Na^+ + CO_{2(aq)} + H_2O \rightleftarrows \text{dawsonite} + SiO_2 + K^+$$

Also, shale that has a high concentration of Fe-Mg due to clay rich mineralogy reacts with CO_2 as shown in the following equation and causes significant amounts of magnesite cementations. Johnson et al. (2004) also argue that the drop in porosity and permeability from these reactions is severe within shale.

$$\text{K-feldspar+Mg-chlorite+}CO_{2(aq)} \rightleftarrows \text{muscovite+kaolinite+magnesite+}SiO_2+H_2O$$

For the rocks with Na/K or Ca/Mg/Fe minerals, Gunter et al. (1996) postulates that the injected CO_2 forms bicarbonate brines and results in siderite, calcite or dolomite. These reactions are assumed to lead to trapping and immobilization of CO_2. The reactions with Ca/Mg/Fe-bearing silicate minerals can be summarized as follows (Saylor et al., 2001).

$$\text{Ca/Mg/Fe feldspar+clays+}CO_2+H_2O=\text{kaolinite+Ca/Mg/Fe carbonate+quartz}$$

A case study of geochemical reactions performed at the Nagaoka site in Japan revealed (Mito et al., 2008) an increase in cations of Ca, Mg and Fe with dissolution of plagioclase and chlorite in early stage of CO_2 storage as shown in Table 2-2. Dissolution of plagioclase and chlorite help neutralize the acidic formation water and eventually results in an increase in the carbonate mineral precipitation:

$$CO_2(\text{supercritical}) \longrightarrow CO_2(aq)$$
$$CO_2(aq)+H_2O \longrightarrow H^+ + HCO_3^-$$
$$\text{plagioclase}+2H^+ +3H_2O \longrightarrow Ca^{2+} + 2Al(OH)_3 + 2H_4SiO_4 + NaAlSi_3O_4$$
$$\text{chlorite}+20H^+ + \longrightarrow 5Mg^{2+} + 5Fe^{2+} + 4Al(OH)_3 + 6H_4SiO_4$$
$$\text{Calcite}+H^+ \longrightarrow Ca^{2+} + HCO_3^-$$

Table 2-2. Geochemical processes at Nagaoka during an early stage of CO_2 storage (Mito et al., 2008).

There have been numerous studies on the effect of the pH on geochemical reactions. Drunkenmiller et al. (2005) found that the pH determines which geochemical reaction in Table 2-1 dominates. For example, at low pH the dominant product is H_2CO_3 while at high pH, CO_3^{2-} is dominant. Thus, the dissolution of carbonate minerals is favored due to the insufficient carbonate ions when pH of the system is acidic. Soong et al. (2004) investigated the CO_2 reactions with brine samples and the effect of pH, temperature and CO_2 pressure on the reactions. Soong et al. (2004) also found that the pH

of the brine changes the precipitation species and reaction rates and mineral precipitation increases as pH of the system becomes basic.

2.2.2 Laboratory Experiments and Simulation Studies

Studies on mineral trapping mechanism have yielded conflicting findings; some researchers (Gunter et al., 1993; Johnson et al., 2004; Zerai et al., 2006) proposed it as an effective long-term CO_2 trapping mechanism due to carbonate mineral precipitation, while others (Heath et al., 2009; Urquhart, 2011) disputed it to be ineffective for long-term sequestration of CO_2.

Gunter et al. (1996) performed both experiments and modeling for a glauconitic sandstone aquifer in the Alberta Sedimentary Basin and stated that geochemical reactions of CO_2 are effective in trapping CO_2. Even though the CO_2 trapping reactions occur very slowly, Gunter et al. (1997) argues it to be sufficient for CO_2 sequestration process due to the slow flow velocity of the aquifer. Geochemical modeling results based on the code PATHARC.94 and rate data from the literature also showed that near-well pressure buildups could be avoided by injecting CO_2 in a local high permeability zone.

Simulation studies have been done by many researchers for various fields using geochemical models (Cantucci et al., 2009; Liu et al., 2010; Zerai et al., 2006). First, a case study was carried out using the PRHEEQC (V2.14) Software Package, a geochemical model, for the Weyburn project, Canada. Cantucci et al. (2009) claimed that the geochemical simulations for the injected CO_2 at the Weyburn Oil Field showed favorable results for mineral trapping through dawsonite precipitation. Also, Zerai et al. (2006) conducted the path-of-reaction and kinetic modeling for CO_2 injection in the Rose Run Sandstone. These authors argued that mineral trapping in the Rose Run Sandstone is viable to capture and store large amounts of CO_2. Lastly, CO_2 injection was simulated using a coupled reactive flow and transport model in the Mt. Simon sandstone formation, Midwest U.S. As a result, Liu et al. (2010) concluded that the Mt. Simon siliciclastic sandstone was an appropriate site for CO_2 storage and mineral trapping would be effective for trapping CO_2 over longer time scales.

Heidaryan et al. (2008) asserted that both laboratory experiments and simulated results for a CO_2 injection coreflood indicated geochemical reactions that were favorable for CO_2 sequestration. The results showed an increase in porosity for the first half of the core due to mineral dissolution and a decrease in porosity for the second half of the core due to the mineral precipitation. These changes in porosity could be correlated with permeability through the Kozeny-Carman equation or the Civan Power Law, and/or empirical correlations by Wellman et al. (2003) and Izgec et al (2006).

However, uncertainties regarding the mineral trapping mechanism remain. Parameters such as mineral kinetic properties and reactive surface areas are very difficult to measure so that it is almost impossible to calculate the accurate time frame for geochemical reactions to occur in CO_2 sequestration process. Also, decrease in porosity around the wellbore due to carbonate mineral precipitation could lower the injectivity of CO_2 as detected in CO_2 injection process for enhanced oil recovery (Xu et al., 2001). This in turn could lead to formation of fractures that could provide leakage paths for the CO_2. In CO_2 sequestration process, it is important to monitor the injected CO_2 so that we can prevent an undesirable leakage from happening. In order to gauge the long term fate of stored CO_2, some researchers have focused on activities of CO_2-driven geysers because they could provide clues about CO_2 gas leakage and migration. Importantly, there are indications on the surface for occurrences of geochemical reactions and carbonate mineralization associated with CO_2 in subsurface such as travertine mounds observed at the Crystal Geyser site.

2.3 CO_2-driven Geysers

There have been a number of studies devoted to the specialized topic of CO_2 leakage risk (Shipton et al., 2004). To have a better understanding of risk of CO_2 leakage and migration from the subsurface, many researchers have studied naturally occurring CO_2 storage system, and their surface expression in the form of CO_2-driven geysers. Exploratory or abandoned wells drilled into these natural CO_2 storage sites result in

geysers that are characterized by intermittent eruption of CO_2-enriched gas and waters as shown in Figure 2-1. Figure 2-1 shows an eruption from the Crystal Geyser, which is located on the bank of the Green River in the Colorado Plateau, Utah.

Figure 2-1. An eruption at the Crystal Geyser (Gouveia et al., 2005).

Surface seeps could possibly be appropriate sites for identifying CO_2 gas leakage in CO_2 sequestration process if we completely understand the scenarios for the source of CO_2 and the mechanism of transportation to the site. Geochemical data suggest that CO_2 in most of these surface seep sites either originated from a deep subsurface source such as the Earth's crust or regional groundwater that transports dissolved CO_2 (Shipton et al., 2004). At the Crystal Geyser site, most of the CO_2 seeps occur along the Little Grand Wash and Salt Wash faults shown in Figure 2-2 (Shipton et al., 2004). The probable origins of CO_2 gas and the location of the seep spots in the fault regions indicate a possibility of the fault acting as conduits for CO_2 migration to the surface.

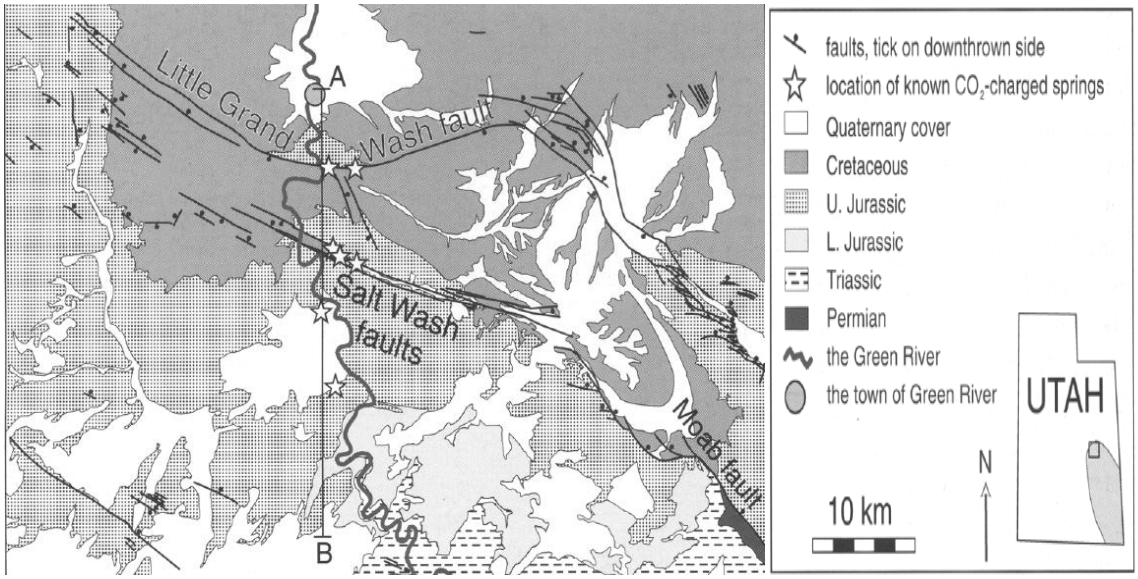

Figure 2-2. Location of CO_2-driven geysers in the Colorado Plateau, Utah (Shipton et al., 2004).

There are travertine mounds and carbonates around springs at the Little Grand Wash fault region. Figure 2-3 shows the ancient, active and inactive travertine mounds (Shipton et al., 2004). Figure 2-4 shows travertine platform deposited on surface caused by calcite precipitation and subsequent biogeochemical effects (Urquhart, 2011). Although carbonate mineralization occurs in the subsurface and results in the form of travertine deposits on the surface, there is also leakage of CO_2 gas to the surface (Heath et al., 2009). Thus, Heath et al. (2009) argued that the geochemical reactions associated with CO_2 in mineral trapping mechanism do not self-seal the leakage path of CO_2. However, there is a lack of rigorous modeling and simulation studies that can help us have a better understanding of the mechanisms controlling the location and temporal evolution of the CO_2-seepage sites. It is necessary to integrate field observations at these natural CO_2 sequestration sites in order to develop a better understanding of subsurface processes. Simulation studies with geochemical models could also investigate whether pore plugging due to chemical precipitation can cause temporal migration of seepage sites.

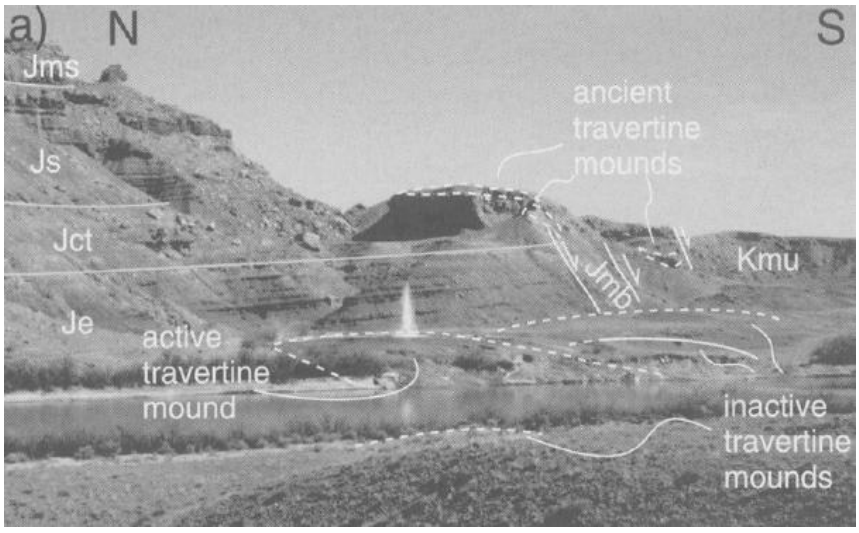

Figure 2-3.Ancient, active and inactive travertine mounds and carbonates along the Grand Wash fault in Utah (Shipton et al., 2004).

Figure 2-4. Crystal Geyser and travertine platform (Urquhart, 2011).

2.4 Numerical Model of Subsurface Transport of CO_2

Previous research studies on numerical models of subsurface transport of CO_2 such as EOS (equation-of-state) models and relative permeability model are reviewed in this section. Negahban et al. (2010) used the PVT data to develop the EOS model that

would reproduce the phase behavior of a reservoir fluid subject to injection of CO_2. The Peng-Robinson equation-of-state (Peng and Robinson, 1976) with volume correction was used for EOS model with CO_2. Jessen et al. (2005) also compared the two most commonly used fluid characterization methods for CO_2 sequestration: Whitson et al. (1989) with the modified PR EOS (Peng-Robinson equation-of-state) and Pedersen et al. (1989) with the Soave-Redlich-Kwong equation-of-state (Soave et al., 1972).

Understanding the relative permeability of a reservoir system in CO_2 sequestration is also important because the relative permeability impacts the storage, migration, and injectivity of CO_2 (Bennion and Bachu, 2005). Bennion and Bachu (2005) performed the experiments with three sandstones and three carbonate formations from the Wabamun Lake in Alberta to investigate the relative permeability of CO_2-brine systems and the displacement of CO_2. Spiteri et al. (2005) also studied models of trapping and relative permeability hysteresis and their impact in CO_2 sequestration. Wettability is also studied in previous research because it is one of the most important parameters in CO_2 storage process which affects relative permeability, fluid saturations and capillary pressure of a system. Chalbaud et al. (2007) carried out the laboratory experiments to investigate the effects of wettability in case of CO_2 injection.

Numerical schemes for CO_2 sequestration are reviewed. Yang et al. (2005) investigated a proper grid system for numerical simulation of CO_2 injection. Different numerical simulation models such as GEM (Generalized Equation-of-State Model) and STARS (Steam, Thermal, and Advanced Processes Reservoir Simulator) from CMG (Computer Modeling Group) and PATHARC 94 were used by many researchers in the literature on CO_2 sequestration (Izgec et al., 2006; Pruess et al., 2003). In Chapter 3, the numerical models with reactive transport elements are examined in detail.

Chapter 3 : Methodology for Modeling

3.1 Overview

It is essential to have a scientific understanding of the subsurface processes associated with the flow and transport of carbon dioxide (CO_2) in the subsurface so that its long-term fate can be predicted. However, it is not possible to physically monitor or observe these processes in the subsurface and instead, we have to rely on surface expressions of these processes in order to infer characteristics of the processes and for calibrating numerical models. Thus, simulation studies and modeling are performed to integrate the field observations and predict the possible physical, chemical, and biological processes in the subsurface. Moreover, modeling can investigate the possible consequences of CO_2 sequestration and long-term storage at the field scale whereas experimental methodologies, such as laboratory experiments, can explain the subsurface processes at shorter length scales and over a short period of time.

3.2 Modeling Method

3.2.1 Field Site

The area of focus is the Colorado Plateau region in east-central Utah, especially around the fault system, The Little Grand Wash fault, shown in Figure 3-1.

Figure 3-1. The Little Grand Wash fault zone in Utah (Urquhart, 2011).

Several CO_2 seeps have been detected in this region; some active and others inactive. These CO_2-driven seeps are localized along the Little Grand Wash fault. Figure 3-2 shows the location of the CO_2 seeps along the fault system in Utah (Urquhart, 2011). One of the most active indicators of the subsurface CO_2 storage systems is the Crystal Geyser which is located on the east bank of the Green River. CO_2 charged groundwater flow is observed at that location along an abandoned well and several researchers (Gouveia et al., 2006; Nishi et al., 2000) have studied the characteristics of the geyser eruptions. All CO_2 seeps are located within the Little Grand Wash fault zone, which indicates that the fault system has regional control on the locations of CO_2 seeps. Shipton et al. (2004) stated that the geological and geochemical data were consistent with the faults being conduits for CO_2 moving to the surface.

Figure 3-2. Active and fossil CO_2 seeps along the Little Grand Wash fault (Urquhart, 2011).

Several researchers have worked on both advanced geological interpretations of the Crystal Geyser area as well as laboratory analyses using samples from that site (Gouveia et al., 2006; Heath et al., 2009; Shipton et al., 2004; Urquhart, 2011). In addition to the previous research studies, analyzing the surface expressions of the CO_2

seep events using numerical models will help us understand the dominant subsurface processes.

3.2.2 Geology

The Little Grand Wash fault system is located in the Colorado Plateau near Green River, Utah. The fault system and its geological settings are illustrated in Figure 3-3. The fault system is about 200 meter wide and comprises of hundreds of subparallel fault segments. All these small segments have different offsets ranging from 1 meter to over 100 meter; we assumed that the total throw of the fault system is 80 meter in our numerical models. We also assumed that the regional groundwater flow is restricted to the Navajo Sandstone that is about 500 meter deep (Shipton et al., 2004). We assumed that this groundwater is being recharged from the San Rafael Swell which is located in the northwest side of the Little Grand Wash fault.

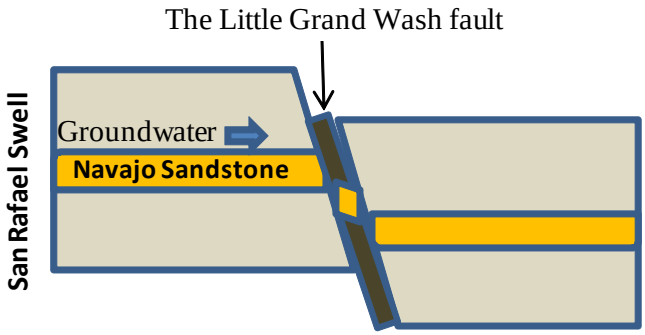

Figure 3-3. Illustration of The Little Grand Wash fault system and the main aquifer zone.

The Navajo Sandstone is presumed to be composed of multiple sand layers which the aquifer flows through. Thickness and permeability about the sand layers are listed in Table 3-1 and incorporated into the modeling.

Lithology	Thickness (meter)	Permeability (md)
sand 5	5	100
shale	5	0
sand 4	5	375
shale	5	0
sand 3	5	215
shale	15	0
sand 2	11	37
shale	10	0
sand 1	5	100

Table 3-1. Stratigraphy of the Navajo Sandstone.

3.2.3 Geochemical Model

3.2.3.1 Description

Several equilibrium geochemical models have been developed and used in literature to study geochemical reactions in simulation; WATEQ4F, MINTEQA2, etc. (Saylor et al., 2001). However, geochemical models need to be fully coupled with reactive transport models to characterize the reservoir and processes at field scale. For this we used GEM (Generalized Equation-of-State Model), which is one of the well-known reservoir flow simulators in the oil industry that has a reactive transport model. The simulator was improved for modeling CO_2 storage by coupling with geochemical and compositional Equation-of-State (EOS) models. Nghiem et al. (2004) give details on the geochemical compositional EOS modeling. The main elements of the model include components material balance equation, chemical equilibrium equations, and the rate law for the mineral dissolution and precipitation reaction.

3.2.3.2 Fluid and Reaction Parameters

The settings for the geochemical model are described in this section. Two components are included in the model, CO_2 and C_1. C_1 is used as a trace component to prevent gas or oil phase from absolutely disappearing in the water zone when gas solubility is activated. The PVT properties for the two components are obtained from literature (Nghiem et al., 2004) and shown in Table 3-2. A phase diagram of CO_2 with

initial conditions is also shown in Figure 3-4. The geochemical reaction equations are selected so as to be consistent with the surface observation of travertine mounds at the Crystal Geyser site. The values for the parameters in chemical equilibrium reactions are not directly obtained from the field sampling in the Colorado Plateau, Utah, but extracted from the literature. There are also several assumptions made regarding uncertain properties such as initial mineral compositions and aqueous component concentrations. However, simulation results from case studies and sensitivity analysis could still give us a valuable interpretation of ongoing subsurface processes in the field.

	CO_2	C_1
Molecular Wt. (g/gmole)	44.01	16.04
Critical Pressure (atm)	72.8	45.4
Critical Temperature (K)	304.2	109.6
Acentric factor	0.225	0.008
Critical Volume (m^3/kgmole)	0.094	0.099
Parachor	78	77
Specific Gravity	0.818	0.3
Boiling Point (˚C)	-78.45	-161.45
EOS omega A	0.457	0.457
EOS omega B	0.0778	0.0778
Binary Interaction Coefficient	0.103	

Table 3-2. PVT properties for component CO_2 and C_1 (Nghiem et al., 2004).

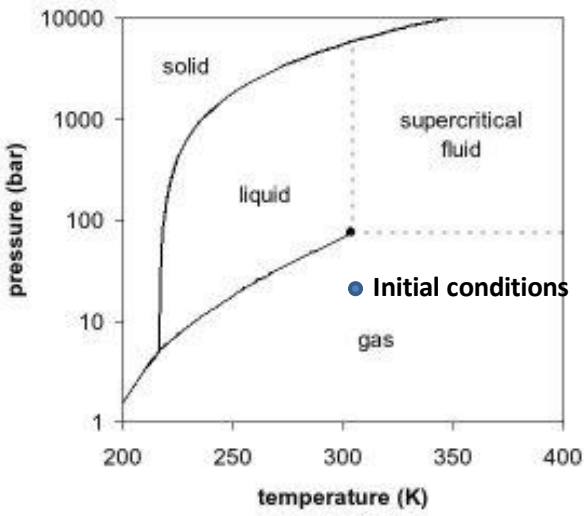

Figure 3-4. Phase diagram of CO_2 with initial conditions (Moore et al., 2008).

First of all, three geochemical reactions and three mineral dissolution and precipitation reactions are selected as shown in Table 3-3 for modeling the surface CO_2 seeps in the Colorado Plateau, Utah. Three mineral reactions are chosen with emphasis on carbonate mineralization because travertine mounds are observed in the field which are formed by the process of calcium carbonate precipitation.

$H_2O=H^+ +OH^-$

$CO_2(aq)+H_2O=H^+ +HCO_3^-$

$CO_3^{--}+H^+ =HCO_3^-$

$Calcite+H^+ =Ca^{++}+HCO_3^-$

$Kaolinite+6H^+ =5H_2O+2SiO_2+2Al^{+++}$

$Anorthite+8H^+ =Ca^{++}+2Al^{+++}+2SiO_2(aq)+4H_2O$

Table 3-3. Chemical and mineral dissolution/precipitation reactions in simulation (Nghiem et al., 2004).

Next, seven aqueous components are chosen excluding the gaseous solutes in the geochemical model as follows: H^+, Ca^{++}, SiO_2 (aq), Al^{+++}, OH^-, HCO_3^-, CO_3^{--}. Initial aqueous phase concentrations for these components are listed in Table 3-4. Also, the

aqueous chemical equilibrium reactions and mineral reaction parameters are shown in Table 3-5 and Table 3-6, respectively (Nghiem et al., 2004; Shrivastava et al., 2004). The reference temperature at which the rate constants are specified is 25˚C. The dissolution of minerals or the precipitation of solutes is controlled in the simulator using a super-saturation-index. In the numerical models for the Crystal geyser area, the simulator was allowed to determine this index internally (without user input) based on considerations such as the pH of the reservoir fluid system. For instance, precipitation of carbonate minerals dominates in areas with a basic pH because carbonate ions form and become available in that condition.

Aqueous species	Molality
H^+	1.0000E-07
Ca^{++}	9.1185E-05
SiO_2 (aq)	2.3454E-08
Al^{+++}	2.3178E-11
OH^-	5.4563E-07
HCO_3^-	2.4893E-02
CO_3^{--}	1.1703E-05

Table 3-4. Initial aqueous species concentration in simulation (Nghiem et al., 2004).

Reactions	log K^a_{eq}
$H_2O=H^++OH^-$	-13.2631
CO_2 (aq)+$H_2O=H^++HCO_3^-$	-6.3221
$CO_3^{--}+H^+=HCO_3^-$	-10.2342

Table 3-5. Aqueous chemical equilibrium reaction parameter in simulation (Nghiem et al., 2004).

Mineral	$\log K^{m}_{eq}$	$\log K_{\beta}$	$\hat{A}_{\beta}$	$E_{a\beta}$	Initial volume fraction
Calcite	1.356	-8.79588	88	41870	0.0088
Anorthite	23.0603	-12	88	67830	0.0088
Kaolinite	5.4706	-13	17600	62760	0.0176

Table 3-6. Mineral reaction parameters in simulation (Nghiem et al., 2004).

3.2.3.3 Limitations

There is a major challenge in representing the Grand Wash fault system in the simulator. As mentioned before, the Little Grand Wash fault system comprises of hundreds of subparallel fault segments that are composed of different filling materials. Rather than representing all these fault segments and there consequent offsets, a stochastic modeling approach was adopted for assigned properties within the fault region.

Xu et al. (2001) suggest that the range of problems related to CO_2 sequestration in subsurface environments is far more extensive and complex than any code currently accommodates due to uncertainties in the kinetics of heterogeneous reactions and reactive surface areas, and a lack of geochemical data at field sites. Therefore, simulation results could possibly be biased depending on what physical and chemical modeling capabilities are incorporated in the simulator. Consequently, simulation results require careful interpretation and analysis.

Chapter 4 : Modeling CO_2 Leakage through a Fault System

4.1 Overview

A number of CO_2-seepage sites have been observed along the Little Grand Wash fault in the Colorado Plateau, Utah. The Little Grand Wash fault is composed of multiple subparallel fault segments that could help transport dissolved CO_2 from depth. When brine with dissolved CO_2 migrates to a shallower depth through the fault system, the solubility of CO_2 in water decreases due to the drop in pressure. As a result degassing of CO_2 gas may occur that in turn results in CO_2 gas driven geyser eruptions such as the Crystal Geyser.

The solubility of CO_2 in water is a function of temperature, pressure and salt composition. Wiebe et al. (1940) conducted laboratory experiments to study the effects of temperature and pressure on the solubility of CO_2 in water and Duan et al. (2002) calculated CO_2 solubility (mol/kg water) in water at different temperature and pressure. The experimental data showing that the solubility of CO_2 in water decreases as pressure decreases is shown in Figure 4-1. Therefore, the solubility of CO_2 in water is expected to decrease as CO_2 dissolved groundwater flows up along the fault and consequently, this decrease in solubility of CO_2 in water can lead to release of CO_2 gas.

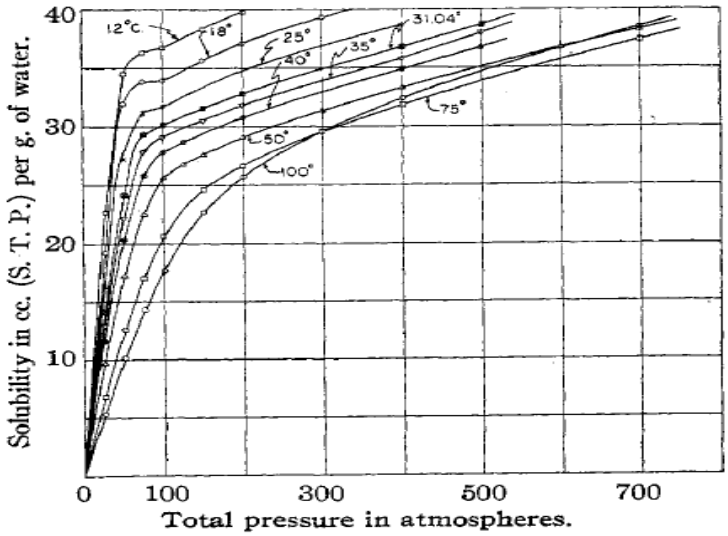

Figure 4-1. Pressure vs. solubility of CO_2 in water (Wiebe et al., 1940).

A generic 2-D model with sand layers and a vertical fault was built to study the gas release mechanism as the groundwater with dissolved CO_2 flows up through a homogeneous fault system. For the reasons mentioned in the previous chapter, it is difficult to exactly represent the flow of transport along the Grand Wash fault. Instead, the flow of CO_2-saturated brine through a generic transmissive fault modeled after the Grand Wash fault is attempted in this and subsequent chapter. Then, sensitivity analyses are performed to understand the extent to which the fault systems can influence the amount of CO_2 gas released in the surface. The effect of two parameters, fault offset and fault permeability, are examined for the sensitivity analyses.

4.2 Flow of CO_2-dissolved Groundwater up a Fault System

To understand and model the process of CO_2 gas release, a simple 2-D grid with a general vertical fault was set up. Geochemical reactions were not included in this model.

Dissolution of CO_2 gas was simulated in a 2-D model with variation only in pressure. Temperature is assumed to be constant at 140˚F everywhere in the simulation. It is assumed that CO_2 dissolved groundwater is at shallow depth and its temperature does not change substantially as it leaks up to the surface. The salt composition of the groundwater is also assumed to be unchanging. Figure 4-2 illustrates the generic 2D model with sand layers and a vertical fault. The properties of sand layers are mentioned in Chapter 3, Table 3-1. Reservoir has the dimensions of 25x1x30 in the x, y, and z directions and each grid block is 100 ft long in the x and y direction with thickness of 50 ft for shale layers. Porosity is 0.2 uniformly. The fault region has the dimensions of 1x1x30 and the fault offset is 200 ft. Injectors are placed in each sand layer far away from the fault plane to mimic the regional flow of groundwater. The ground water is assumed to be made up of 0.012 mole fraction of CO_2 and 0.988 mole fraction of H_2O flowing in each sand layer at the rate of 10 ft^3/day to mimic the natural flow of CO_2-dissolved groundwater.

Monitoring wells were placed on the top layer and the right side of each sand layer to minimize the pressure build-up. Volume modifiers of 30,000 were used in all boundary blocks to create infinite-acting boundaries. These infinite-acting boundaries reduce any undesirable pressure build-up from injecting CO_2 in the reservoir. The permeability of the fault was 5 md uniformly in all grid blocks and the permeability of sand layers are listed in Table 3-1. The simulation ran for 400 years from 1901 to 2301. Pressure profiles at the start and end of the simulation are shown in Figure 4-3; pressure varied with depth and pressure buildup during the simulation was minimal indicative of a flowing groundwater system.

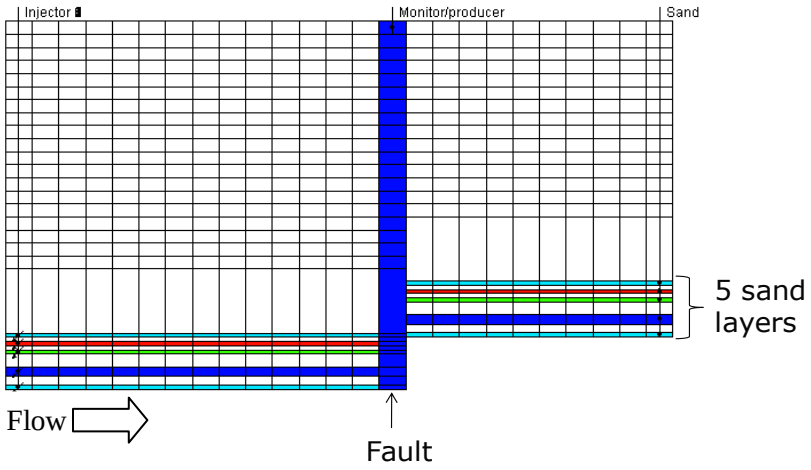

Figure 4-2. Illustration of the 2-D model with sand layers and a vertical fault.

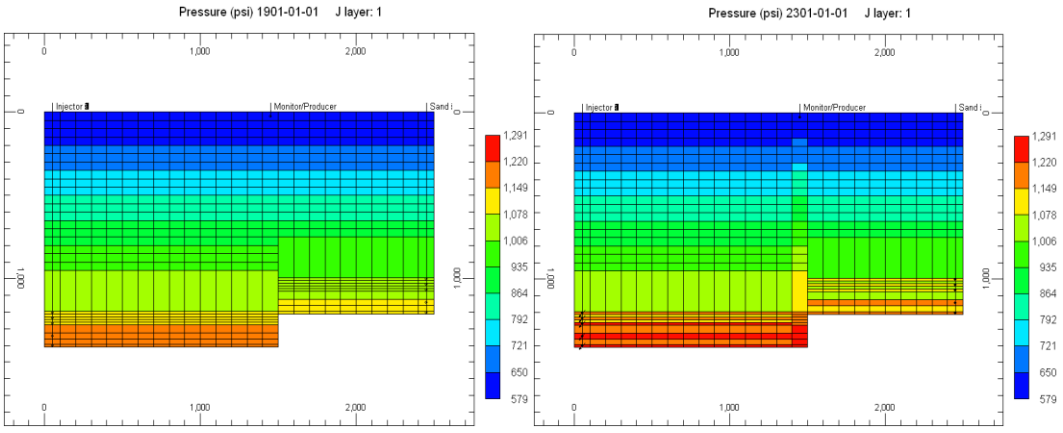

Figure 4-3. Initial and final pressure profiles of the simulation.

CO_2-dissolved solvents were injected at a very low rate to imitate the slow groundwater flow system in the field. As a result, this injected fluid took about 300 years in our case to flow up the fault system and reach the surface in 2200. Figure 4-4 shows the mole fractions of CO_2 in groundwater in year 2000, 2100, 2200 and 2250; The dissolved mole fraction of CO_2 in 2250 was lower at the shallower depth than it was at a deeper depth; illustrating that solubility of CO_2 in water decreased as the groundwater travelled up the fault. This decrease in solubility of CO_2 in water causes the CO_2 to be released from groundwater. Since the temperature and salt composition of the groundwater were fixed, the decrease in pressure as groundwater leaked up along the fault was the main cause for the release of CO_2.

Figure 4-5 shows the gas mole fraction of CO_2 in year 2240, 2250, 2260 and 2270. CO_2 gas did not appear until 2250 when the groundwater made its way to the fault and during its transit up the fault gas was released out of groundwater and started filling up the fault blocks. This appearance of CO_2 gas is also shown in the gas saturation profile. Figure 4-6 shows the gas saturation in year 2240, 2250, 2260 and 2270. Gas saturation increased slowly from zero in 2250 as CO_2 gas dissolved out of groundwater.

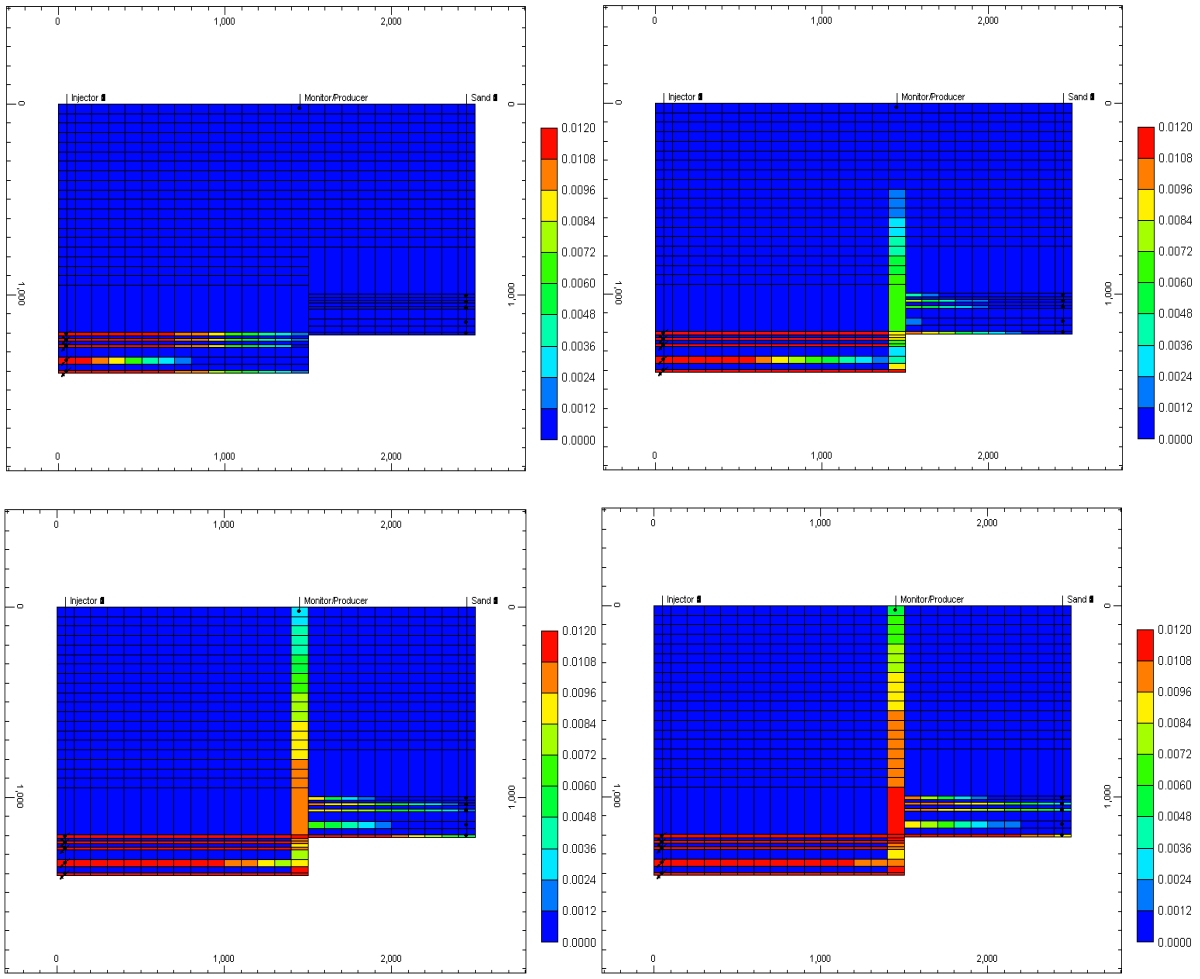

Figure 4-4. CO_2 mole fraction in groundwater in year 2000, 2100, 2200 and 2250.

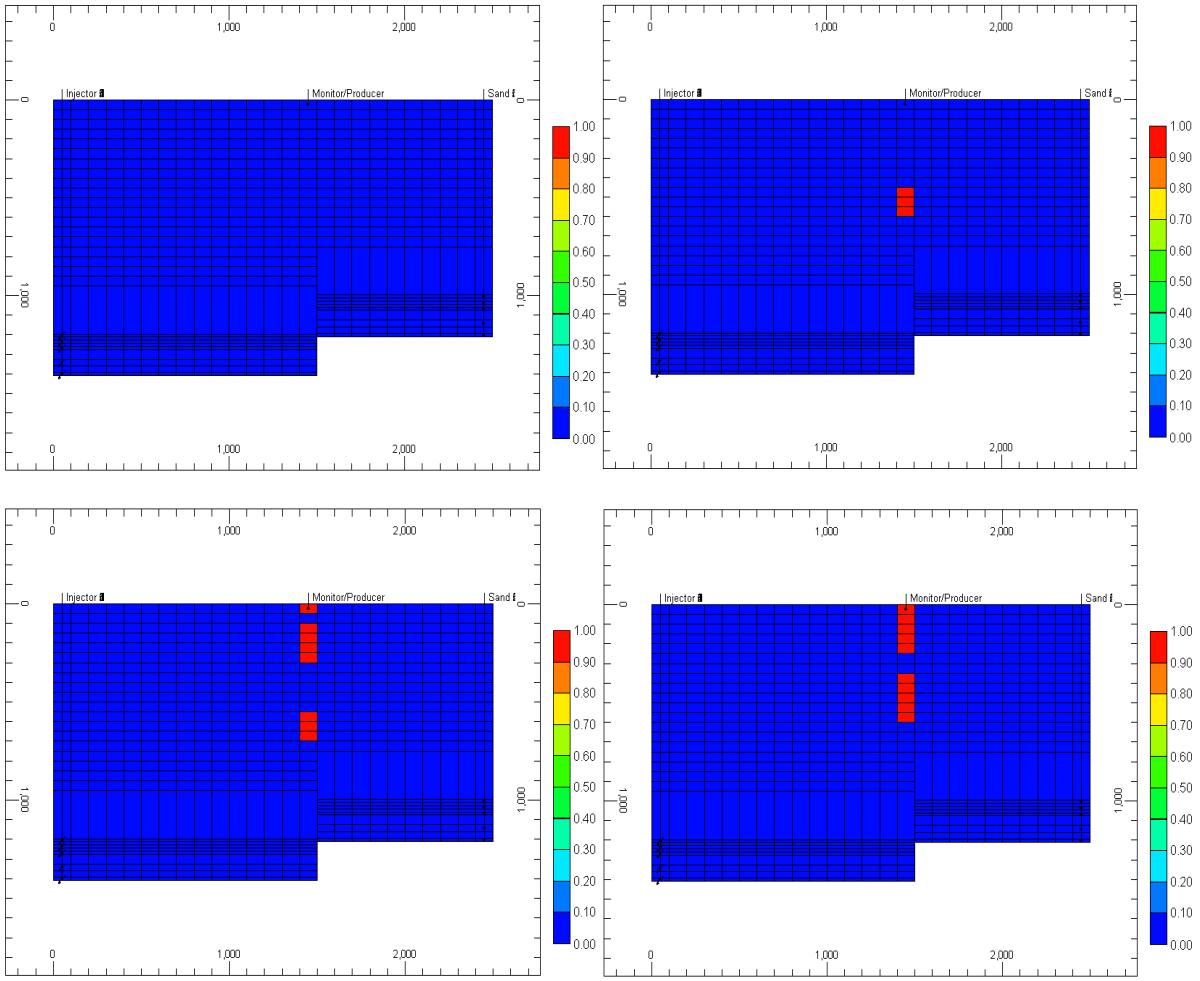

Figure 4-5. Gas mole fraction of CO_2 in year 2240, 2250, 2260 and 2270.

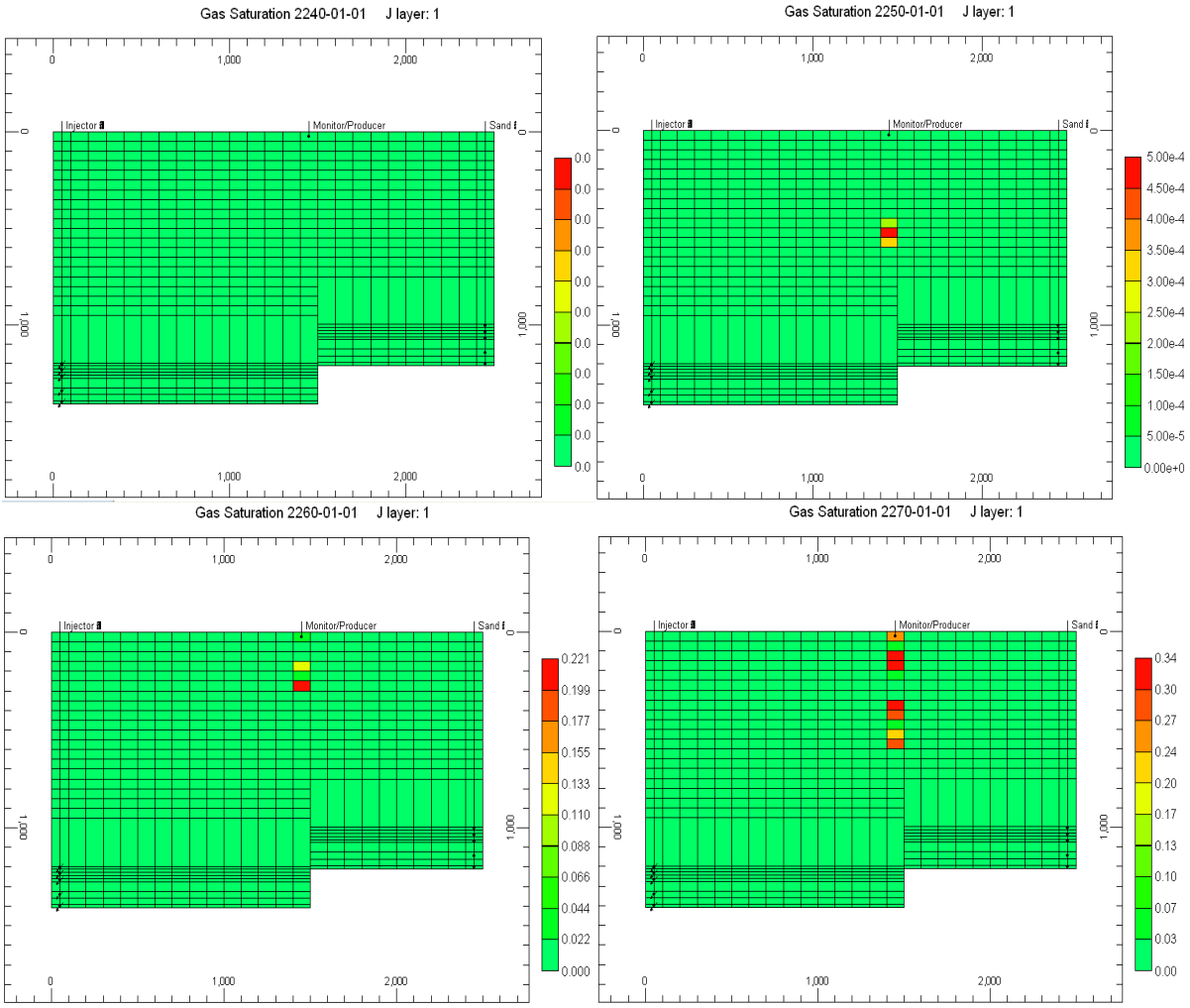

Figure 4-6. Gas saturation in year 2240, 2250, 2260 and 2270.

4.3 Sensitivity Analysis on the Amount of CO_2 Gas Leakage

The amount of CO_2 gas that leaks through the fault system and appears on the surface may be controlled by several parameters such as fault properties and subsurface structure and it is impossible to fully ascertain these parameters from surface or subsurface measurements. Therefore, the amount of CO_2 leakage can never be deterministically estimated. However, the impact of variations in these parameters on the amount of CO_2 gas leakage can be studied using simulation. In this section, the effect of fault offset and fault flow properties on the amount of CO_2 leakage are discussed.

4.3.1 Effect of Fault Offset

We studied the effect of fault offset on the amount of CO_2 leakage based on simulation. We predict less amounts of CO_2 leakage to the surface with a smaller fault offset because fault with a smaller offset would result in less vertical rise of the ground water before it finds a permeable layer to flow through. Several cases were run with different fault offsets in the 2-D base model and the amount of CO_2 liberated in gram-moles was recorded at the surface. It is assumed that the fault is composed of only one subparallel fault segment. Figure 4-7 shows the amount of CO_2 leaked in gram-moles on the surface corresponding to different fault offsets. The amount of CO_2 leaked on the surface decreased with smaller fault offsets. This confirms that the smaller the fault offset, the smaller the vertical rise of the CO_2-dissolved groundwater and consequently the smaller the pressure drop. This is also shown in the velocity profile of the flow up along the fault. Figure 4-8 shows velocity magnitude of the CO_2-dissolved groundwater in year 2020 with two different fault offsets; the smaller the fault offset, the smaller the vertical velocity of the CO_2-dissolved groundwater.

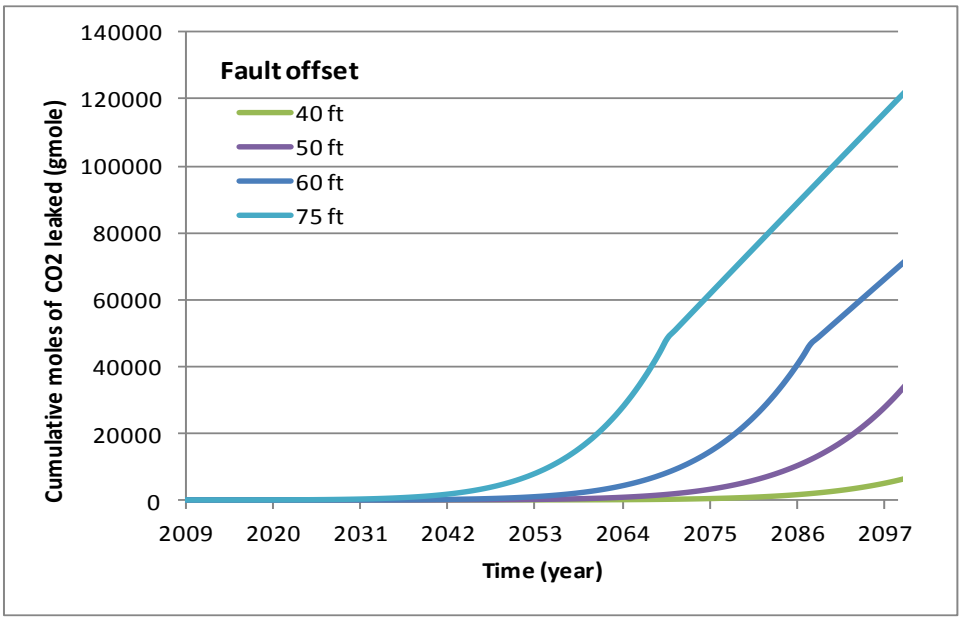

Figure 4-7. Cumulative amount of CO_2 leaked in gram-mole corresponding to different fault offsets.

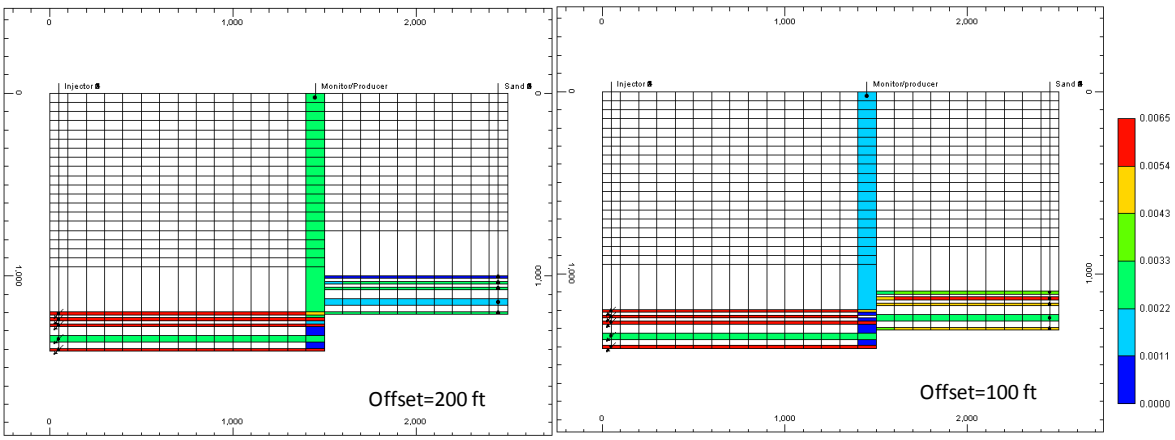

Figure 4-8. Velocity of CO_2-dissolved groundwater in ft/day corresponding to different fault offsets in year 2020.

4.3.2 Effect of Fault Permeability

Permeability determines the extent to which a rock can transmit fluids. Thus the amount of CO_2 leakage through a fault system is very likely to depend on the permeability of the fault fill material. In this section, the effect of fault permeability on the amount of CO_2 leakage was studied. Less CO_2 gas leakage was expected with lower permeability. A simulation was run with different sets of fault permeabilities in a 2-D base model. Figure 4-9 shows the amount of CO_2 leaked in aqueous and gas phases with different levels of fault permeabilities. Declines in the amount of CO_2 produced were observed in both aqueous and gas phases of CO_2 as permeability of the fault decreases. The slope of the graph in Figure 4-9, which indicates the effect of permeability change on the amount of CO_2 leaked change, is larger at a lower permeability because same amount of change in permeability would impact more with low initial permeability than with high initial permeability.

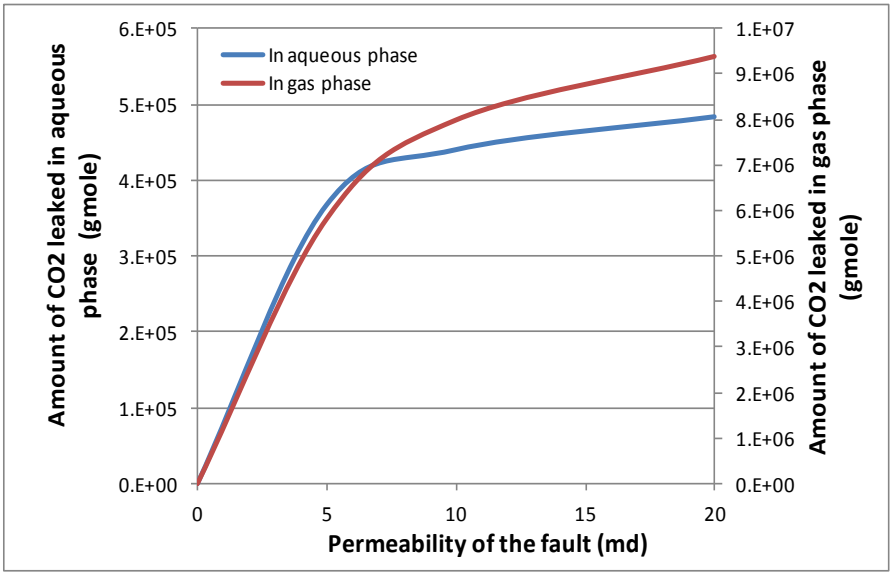

Figure 4-9. Amount of CO_2 leaked in aqueous and gas phases as a function of the permeability of the fault.

In reality, the permeabilities of fault sub-segments around shale layers are low due to the smearing of the shearing action of the fault. The shale layers wear down and plug up the fault system. In our model, shale layers are smeared up and down in both side due to the fault offset as shown in Figure 4-10. However, smearing of the shale layers might happen preferentially to only up or down according to the dip direction of the fault. To examine the potential impact of this phenomenon, the simulation was run with the permeability reduced from 20 md to 3 md in the fault sub-segments around the shale layers and the results were compared with the results in case of the homogeneous fault with uniform permeability of 20 md and no shale smearing effect. Figure 4-11 compares the CO_2 gas mass rates from the cases with non-homogeneous fault using reduced permeability around the shale layers against the result for the homogeneous fault. The CO_2 gas mass rate with the reduced permeability around the shale layers was higher than that with the homogeneous permeability. Also, CO_2 gas production at the monitoring well starts at an earlier date due to the erosion of shale layers into fault system, which indicates that CO_2 gas reached the surface earlier. The shale drape effectively reduces the area of cross section available to flow and that in turn cause a higher pressure drop over

the fault offset. The higher pressure drop in turn results in an increase in the gas ex-solution rate. The gas rates on the surface are sporadic because CO_2 gas is dissolving out of the solution arbitrarily due to unsteady condition of the simulation wherever CO_2 is fully saturated along the fault.

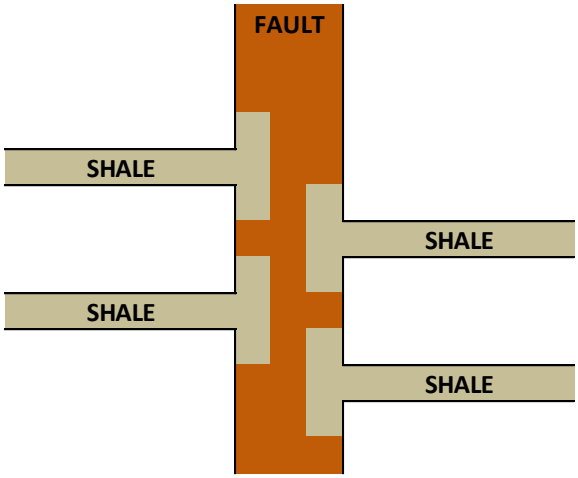

Figure 4-10. Illustration of eroded shale layers in the fault system

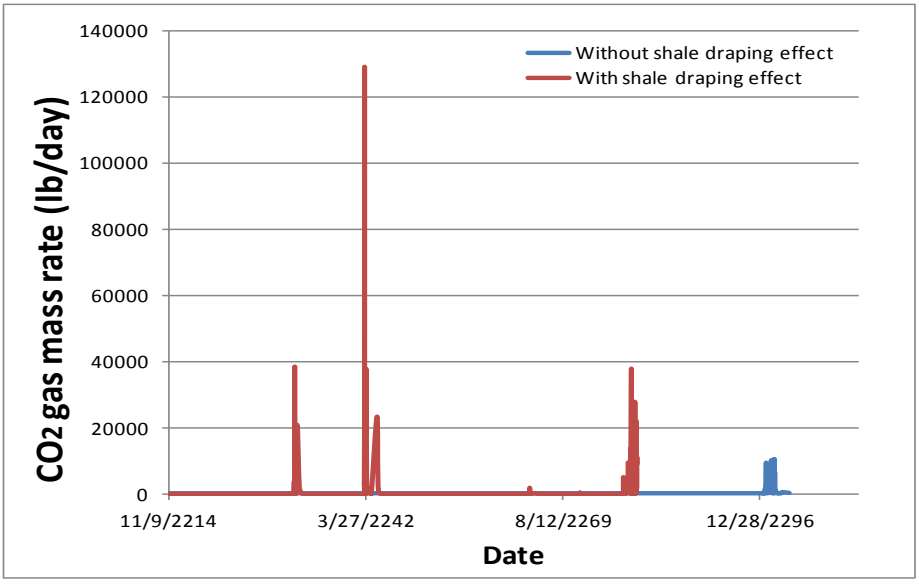

Figure 4-11. CO_2 gas mass rates from the simulation cases with and without the shale drape along the fault plane.

4.4 Conclusions

The study in this chapter reports two major findings. The simulation results for the effect of pressure on the solubility of CO_2 in water agreed with our prior conjecture based on the solution characteristics of CO_2 established in literature. We found that when the CO_2-dissolved groundwater flows up along the fault, the solubility of CO_2 in water is reduced due to the pressure drop and as a result, CO_2 gas dissolves out of the groundwater. On the basis of the simulation, our investigation of the effects of the fault offset and permeability on the amount of CO_2 leakage found an increasing trend in the amount of CO_2 gas leakage with increase in fault offset and increase in fault permeability. The smearing of clays along the fault plane significantly impacts the amount of CO_2 gas leakage. Our simulation results showed that CO_2 gas reached the surface through the fault faster and the amount of CO_2 gas leakage increased due to the presence of shale drapes.

The simulation results suggest that the release of CO_2 gas from groundwater due to the pressure drop during vertical transit through the fault could be a mechanism for CO_2 gas leakage along the fault. Also, sensitivity analysis on the fault parameters suggests that several parameters such as fault offset and fault fill material properties affect the amount of CO_2 leakage. The simulation studies may not accurately predict the amount of CO_2 leakage through the fault system; however, it gives valuable insights on the role of the fault parameters and its impact on the amount of CO_2 gas leakage. In the next chapter, we specify actual field observations in modeling and develop a detailed 3-D model. Moreover, the effects of geochemical reactions involved in CO_2 sequestration processes are investigated using simulation.

Chapter 5 : Modeling Source of CO_2 at the Seep Location

5.1 Overview

Understanding how Carbon Dioxide (CO_2) migrates after injection is vital for successful CO_2 sequestration process. For this purpose, we investigate the CO_2 seeps along the Little Grand Wash fault region and their spatial and temporal characteristics. Specifically, we focus on the origin of the CO_2 so that we can understand the migration and leakage path of CO_2 gas in subsurface. Many processes for CO_2 generation in subsurface are proposed in literature such as mantle degassing, the degradation of organic matter, and decarbonation of carbonates (Selley 1998). Two possible CO_2 sources in the Little Grand Wash fault region are suggested based on previous research - i) a deep crustal CO_2 source and, ii) the CO_2-dissolved groundwater as illustrated in Figure 5-1. Helium isotope data from the Crystal Geyser indicates that a crustal CO_2 source is probable (Heath et al., 2009). The surface expression corresponding to such a source is contrasted against that corresponding to regional flow of CO_2-dissolved groundwater flowing vertically through the fault because of the vertical offset of sandstone layers.

In this chapter, 3-D simulation models with geochemical reactions are constructed together with geological information for the two possible CO_2 sources and the results from two different case studies are described and discussed. We anticipate that modeling could allow us to establish difference in a surface expression of CO_2 leakage due to these two hypotheses and develop a scheme for selecting appropriate model for CO_2 leakage based on a surface observation of travertine mounds. Also, the effect of the fault system on CO_2 flow and transport is further studied using these geochemical models.

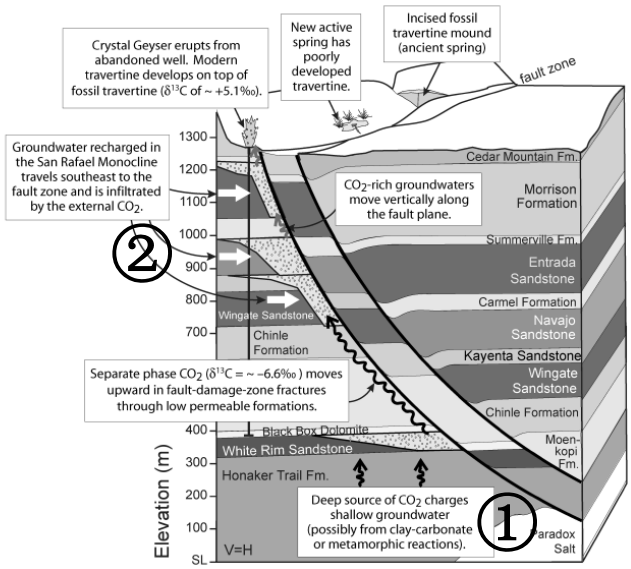

Figure 5-1. Illustration of CO_2 migrations in the Little Grand Wash fault region from the two probable CO_2 sources: (1) Deep Crustal CO_2 (2) regional flow of CO_2-dissolved Groundwater (Vrolijk et al., 2005).

5.2 Case 1: Deep Crustal CO_2

5.2.1 Simulation Setup

A 3-D simulation model with geochemical reactions is constructed for CO_2 migration from the deep Earth's crust in the Little Grand Wash fault region. In previous chapter, a more generic case with up-dip fault is modeled to study the gas release mechanism as the groundwater with dissolved CO_2 flows up through a homogeneous fault system. In this chapter, down-dip fault as the Little Grand Wash fault is modeled. Basic parameters for the simulation setup are shown in Table 5-1. Also, the geochemical reactions and the stratigraphy of the formation used for the modeling are listed in Table 3-1 to Table 3-5. In order to render the flow properties along the fault heterogeneous, sequential Gaussian simulation (Deutsch and Journel, 1992) was used; the method to generate the realization of the fault system used in this chapter is explained in detail in Appendix A. Figure 5-2 shows the permeability for the top layer of the simulation model.

Producers are placed on the top layer as monitoring locations similar to the CO_2 seeps along the Grand Wash fault; producers are only constrained to the minimum bottomhole pressure which is equal to initial reservoir pressure so that they will not deplete any initial reservoir pressure other than pressure build-up due to the injections and will behave as monitoring wells. Figure 5-3 shows the permeability for the bottom layer of the simulation model and Figure 5-4 illustrates the well locations of CO_2 injectors. These injectors are analogous to possible CO_2 sources in the deep Earth's crust; CO_2 is injected below the lowest sand layer and its vertical migration to the fault is observed. The fault offset for this model is 80 meter and is illustrated in Figure 5-4. Values for pore volume modifiers in GEM are specified as 30,000 at all the boundary blocks. In our case, the pore volumes for all the boundary blocks of the model except injection locations are multiplied by 30,000 in the simulation to establish infinite acting reservoir boundaries and to minimize any pressure buildup. Lastly, the simulation runs from 2000 to 2500 for 500 years.

Model dimensions	15 m x 7.5 m x 15 m
Grid	20 x 19 x 19
CO_2 injection rate	10 m^3/day
Porosity	0.2
Temperature	20-40 ˚C
Pressure on surface	101 kPa
Pressure on bottom	2687 kPa

Table 5-1. Simulation setup in the case of deep crustal CO_2.

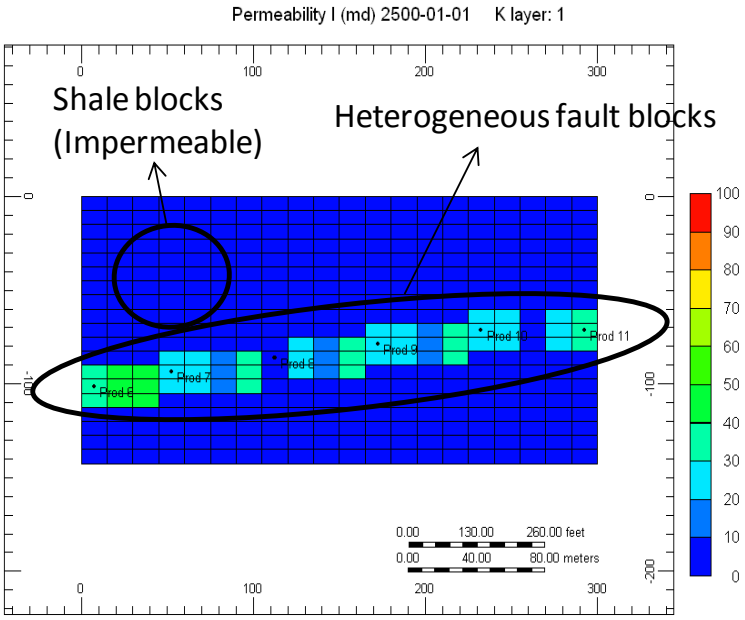

Figure 5-2. Permeability of a top layer from top view in the case of the deep crustal CO_2 and regional flow of CO_2-dissolved groundwater: producers are placed on the top layer as monitoring locations similar to the surface seeps at the field site.

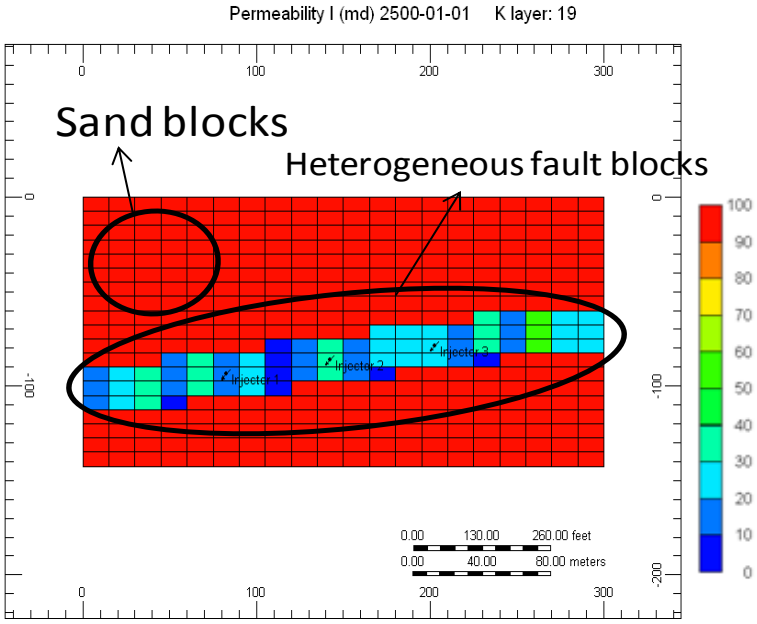

Figure 5-3. Permeability of the bottom layer showing the location of injectors used to mimic the vertical rise of CO_2 gas from the Earth's crust.

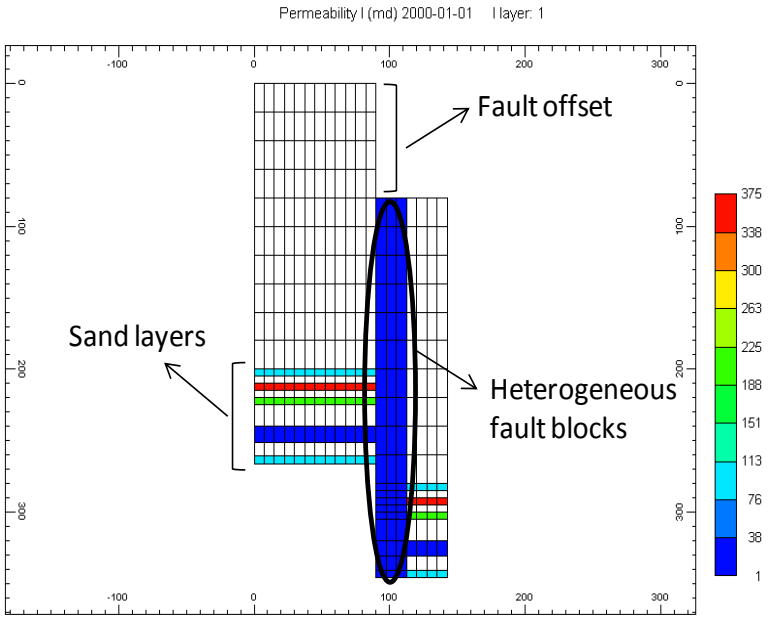

Figure 5-4. Permeability distribution from side view in the case of deep crustal CO_2.

5.2.2 Results and Discussion

Gas migration along the fault due to CO_2 migration from deep Earth's crust is studied in the simulation. CO_2 gas is produced at the monitoring wells on the surface mimicking surface seep and calcite precipitations form along the fault due to the geochemical reactions associated with CO_2. These calcite precipitations reduce the pore volume and effective porosity of the formation accordingly.

Calcite precipitation occurs along the fault as CO_2 flows and reacts with initial aqueous components and minerals in the formation. Figure 5-5 shows the calcite mineralization in gram-mole formed at the end of the simulation in the top layer. It shows a non-uniform distribution of calcite mineralization formed along the fault; this indicates that calcite precipitations are localized to isolated vertical flow paths in case of the deep crustal CO_2. This may have been caused by vertical channeling of CO_2 due to heterogeneity in fault fill material when CO_2 release is from the deep Earth's crust. Figure 5-6 shows calcite mineralization along the cross section AB. It clearly illustrates the localized calcite precipitation in the vertical flow paths of CO_2.

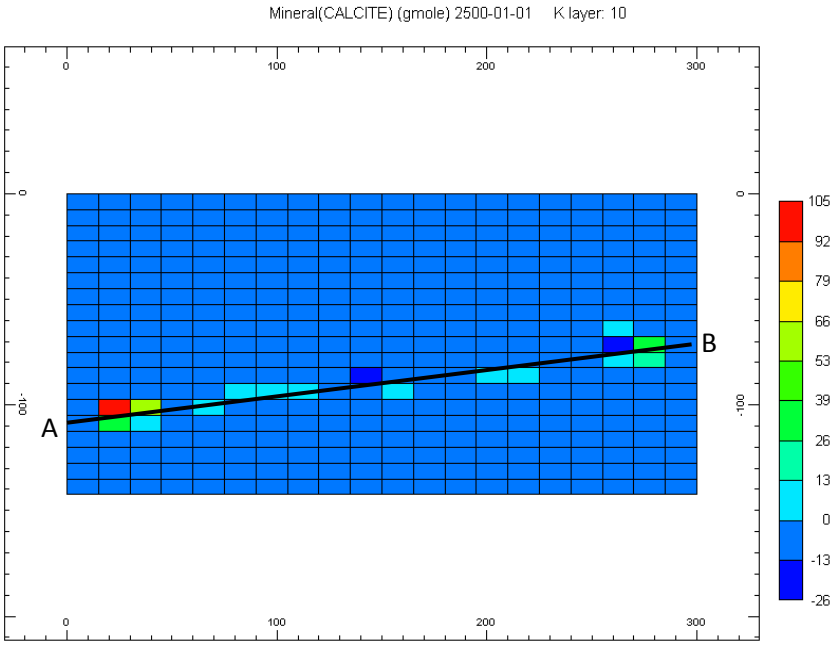

Figure 5-5. Calcite mineralization in gram-mole in the top layer for the case of vertical migration of deep crustal CO_2.

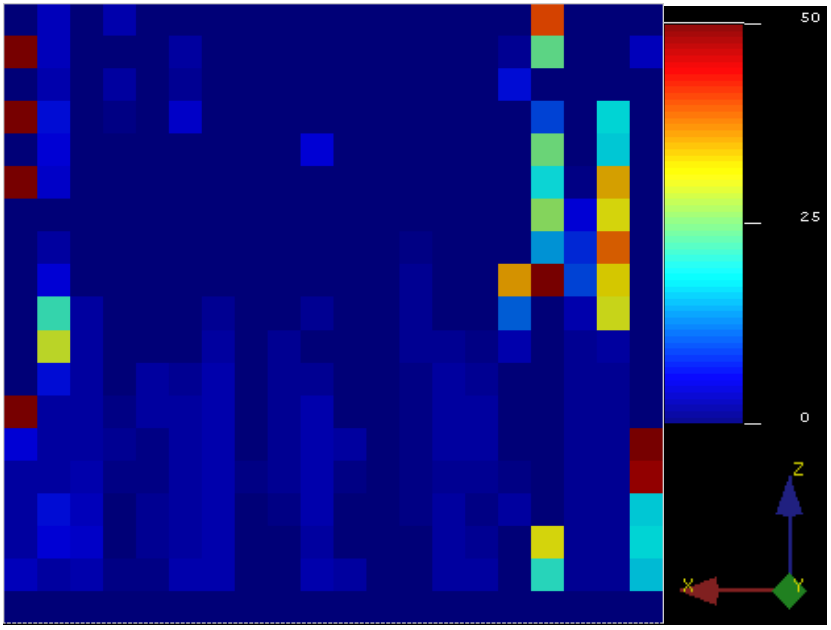

Figure 5-6. Cross sectional along the section AB in Figure 5-5 showing the calcite mineralization in gram-mole.

The simulation results also captured the effects of calcite mineralization on effective porosity. Figure 5-7 and 5-8 show effective porosity and calcite mineralization with respect to time for a grid block, (X=12, Y=10, Z=2), in the fault region. Effective porosity has an inverse relationship to calcite precipitation because creation of calcite minerals in the formation reduces the pore volume of the rock. This demonstrates the capability of the simulator to account for the effects of mineral precipitation on effective porosity of the reservoir. Precipitation of calcite minerals may influence subsequent CO_2 flow and transport because it affects the porosity and permeability. There are numbers of correlations that express the relationship between porosity and permeability such as the Carman-Kozeny equation. However, the simulator used for this study (GEM) is not capable of relating the changes in effective porosity to effective permeability; therefore actual fluid flow and transport was not affected by the mineral reactions associated with CO_2. This important issue will be addressed in Chapter 6.

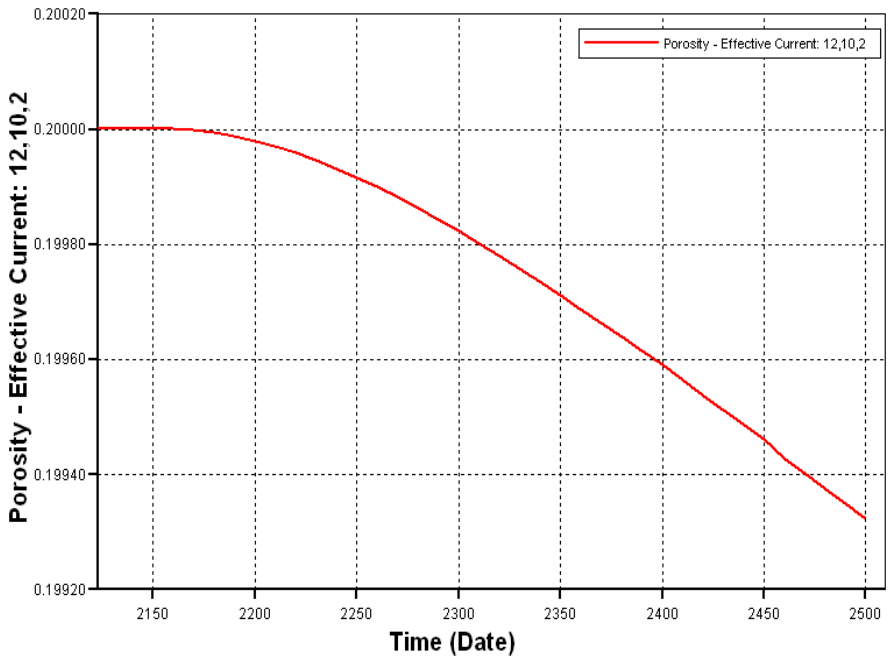

Figure 5-7. Effective porosity vs. time for a fault block in the case of deep crustal CO_2.

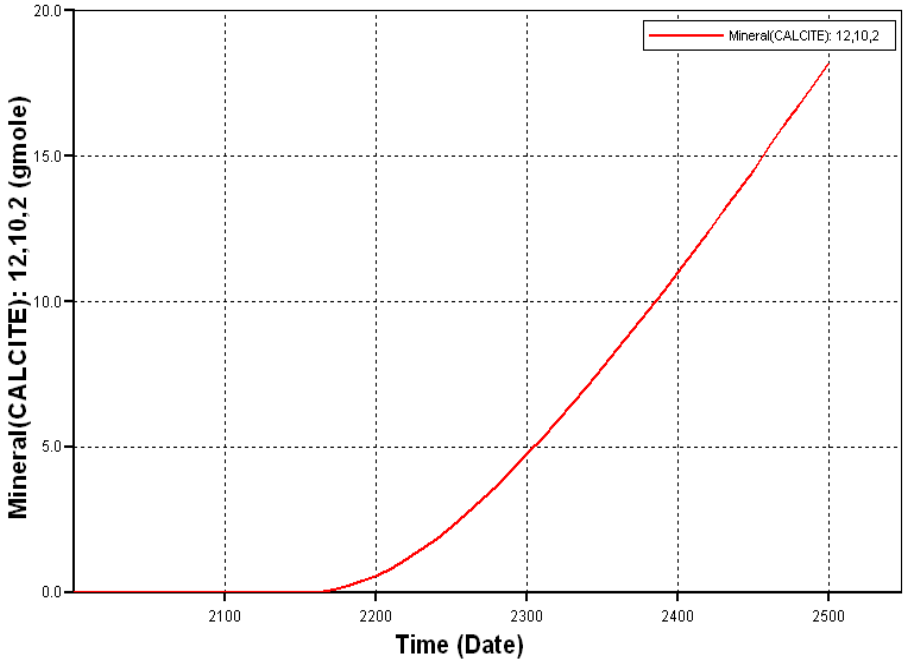

Figure 5-8. Calcite mineralization vs. time for a fault block in the case of deep crustal CO_2.

5.3 Case 2: CO_2-dissolved Groundwater

5.3.1 Simulation Setup

A 3-D model incorporating geochemistry is built for the case of regional flow of CO_2-dissolved groundwater intersecting the Little Grand Wash fault. Basic parameters for the simulation setup are shown in Table 5-2. The geochemical reactions parameters and stratigraphy used in modeling are listed in Table 3-1 to Table 3-5 as well. Producing wells are placed on the top layer as monitoring locations similar to the CO_2 seeps at the Crystal Geyser site as shown in Figure 5-2. A naturally flowing groundwater in the region, or an aquifer, is supposed to have dissolved CO_2 in the aqueous phase. To mimic the natural flow system of the CO_2-groundwater, aqueous solutions are injected into each sand layer with 0.1 molality of CO_2 and 0.9 molality of H_2O. The well locations are shown in Figure 5-9 and reservoir conditions are superimposed in the phase diagram of CO_2 in Figure 5-10. CO_2 is initially injected in the aqueous phase and does not partition

into the gas phase because of the initial pressure and temperature conditions assumed. Aqueous solutions are injected at a slow rate of 2 m^3/day and to avoid any significant pressure build-up around the wellbore. The offset, or throw, of the fault system is 80 meter, same as in Case 1. The simulation runs from 2000 to 2500 for 500 years.

Model dimensions	15 m x 7.5 m x 15 m
Grid	20 x 19 x 19
Aqueous solution injection rate	2 m^3/day
Porosity	0.2
Temperature	20-40 ˚C
Pressure on surface	101 kPa
Pressure on bottom	2687 kPa

Table 5-2. Simulation setup in the case of CO_2-dissolved groundwater.

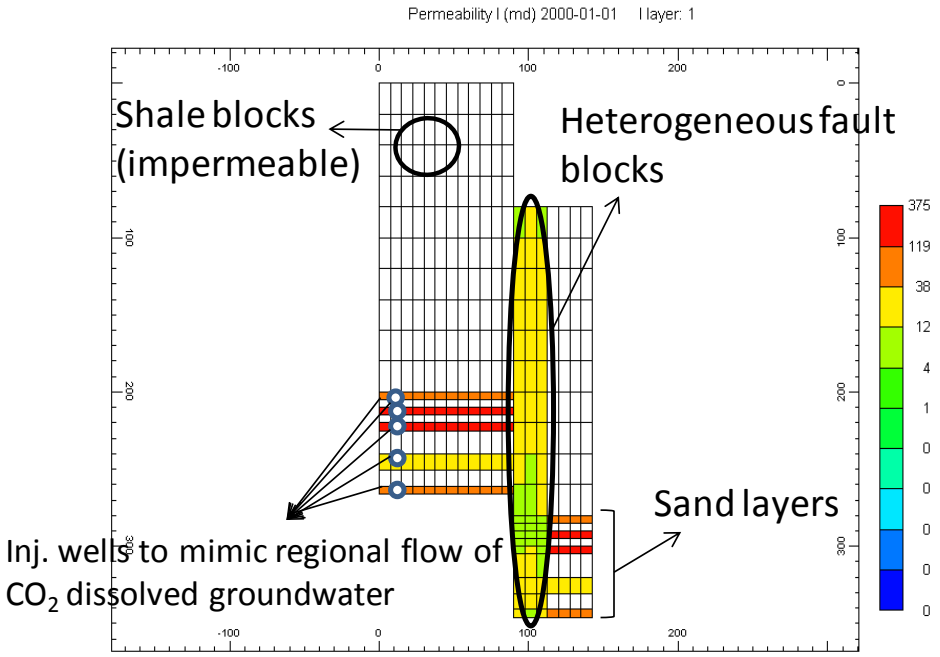

Figure 5-9. Permeability from side view in the case of regional flow of CO_2-dissolved groundwater: injectors are placed in sand layers to imitate natural flow of groundwater system.

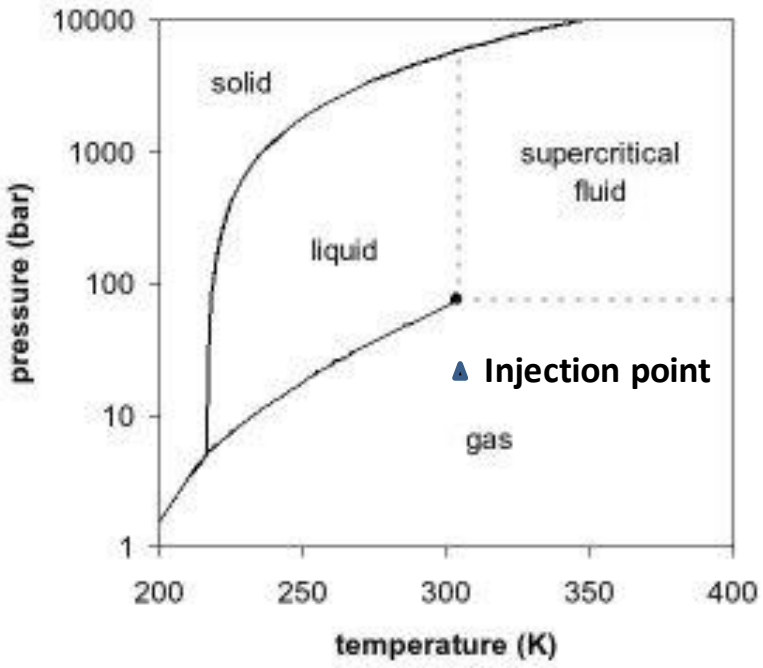

Figure 5-10. Phase diagram of CO_2 with injection conditions in both cases (Moore et al., 2008).

5.3.2 Results and Discussion

Subsurface transport of CO_2 gas in the case of regional flow of CO_2-dissolved groundwater is studied in this simulation. CO_2 is in the aqueous phase in each sand layer and calcite mineralization occurs when the CO_2 comes out of solution. There was a different pattern of calcite mineralization observed along the fault in the case of the CO_2-dissolved groundwater from the pattern observed in case of the deep crustal CO_2. Figure 5-11 shows amounts of calcite mineralization in gram-mole in the top layer for case of the deep crustal CO_2. Calcite precipitation is spread evenly over the entire fault surface. This indicates that calcite precipitation along the fault may have been heavily affected by vertical migration of CO_2-saturated brine along the entire cross section of the fault system which causes a release in pressure and subsequent ex-solution of CO_2. Figure 5-12 shows the cross sectional view for calcite mineralization in gram-mole along the cross section

from C to D. It clearly illustrates that calcite precipitation spreads over the entire fault system.

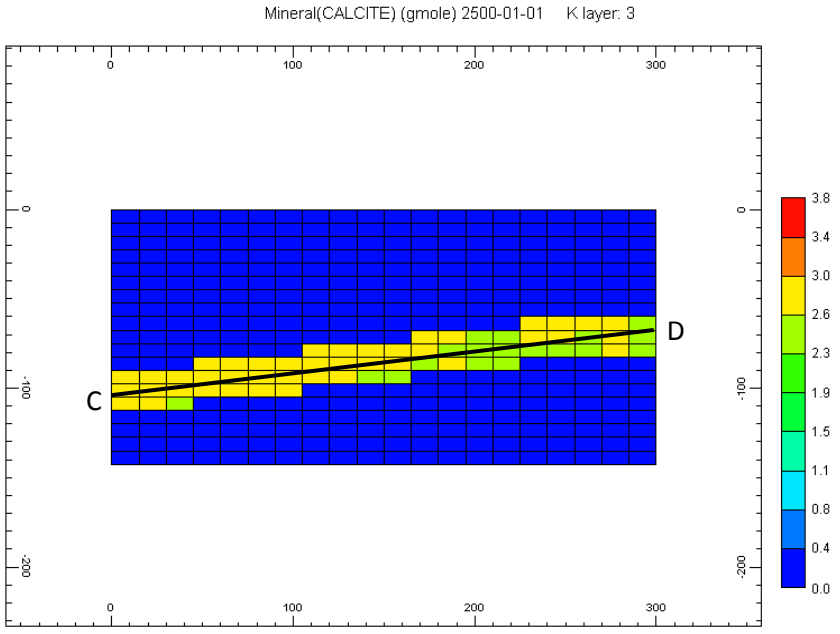

Figure 5-11. Calcite mineralization in gram-mole along the top layer in the case of regional flow of CO_2-dissolved groundwater.

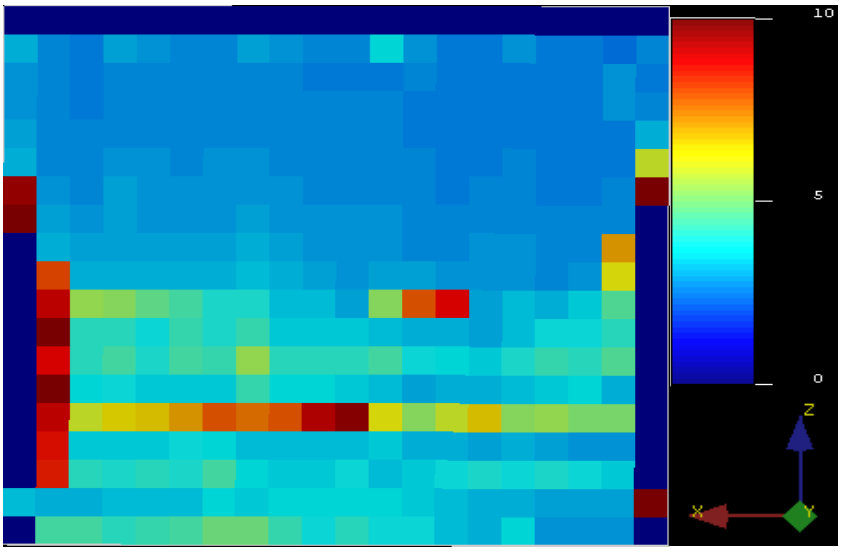

Figure 5-12. Cross sectional view along section CD in Figure 5-11 indicating calcite mineralization in gram-mole for the case of regional flow of CO_2-dissolved groundwater.

5.4 Spatial Distribution of CO_2 Gas Release on Surface

The effects of a heterogeneous fault system on the spatial observation of CO_2 seeps on surface at the Crystal Geyser site are studied in this section. First, monitoring wells are placed at every single fault block on the surface for both the deep crustal CO_2 and CO_2-dissolved groundwater cases to measure the amount of CO_2 gas reaching the surface all along the fault region. It is obvious that the amount of CO_2 gas reaching the surface is directly related to the amount of CO_2 injection, which is very subjective and arbitrarily determined. Therefore the actual amount of CO_2 gas reaching the surface is not the main focus of this study. Instead, the spatial distributions of CO_2 gas released on the surface for these two cases were different even though the same permeability distribution was assumed for the fault system. Figure 5-13 and Figure 5-14 show the amounts of CO_2 gas reaching the surface through the same fault system in the case of regional flow of CO_2-dissolved groundwater and in the case of CO_2 migration from the deep; red indicates higher amounts of CO_2 gas release. In both cases, amounts of CO_2 gas release through the fault system at different locations are mainly affected by the permeability distribution of the fault system. The spatial distribution of CO_2 gas release on the surface in case of the CO_2-dissolved groundwater looks similar to, and is thus largely affected by, the overall permeability distribution of the fault system while the spatial distribution of CO_2 gas release on the surface in case of the deep crustal CO_2 was mainly affected by the location of the high permeability features and their location in relation to the location where CO_2 is introduced into the system. The permeability heterogeneity in that case is highlighted due to the vertical channeling of gas.

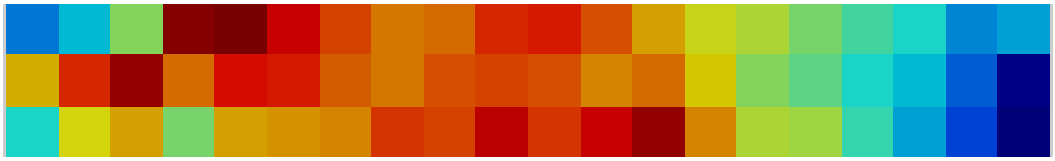

Figure 5-13. Spatial distribution of CO_2 gas release at the surface along the fault system in the case of the regional flow of CO_2-dissolved groundwater.

Figure 5-14. Spatial distribution of CO_2 gas release at the surface along the fault system in the case of deep crustal CO_2.

5.5 Conclusions

Results presented in this chapter indicate that the origin or source of CO_2 has significant effects on the surface expression of CO_2 leakage along the fault system. Different observations corresponding to the two hypotheses for CO_2 source were found by modeling. However, the models for the CO_2 seeps at the field site lack accurate field data. Thus, the simulation studies in this chapter are more intended to provide an insight into probable CO_2 transport and flow mechanisms in subsurface. A more robust and precise modeling is recommended with accurate field data including brine and formation composition, CO_2 production with time, CO_2 seep locations, and topography. More information about the fault system is also necessary for more accurate flow characterization.

Chapter 6 : Modeling Diversion of CO_2 Flow

6.1 Overview

Variations in spatial locations of the Carbon Dioxide (CO_2) seeps with time are observed at the Crystal Geyser site. The migration of CO_2 seeps indicates that migration paths of CO_2 in subsurface have changed over time. We suspect that the change in paths of CO_2 flow may have been caused by mineral dissolution and subsequent precipitation that alter the pore structure of rocks that CO_2 migrates through. The changes in pore structure results in permeability change that will affect the dynamics of CO_2 flow. In this chapter, the diversion of CO_2 flow due to mineral precipitation in rocks is studied using simulation.

6.2 Porosity vs. Permeability with Mineralization

The void volume of the porous medium can be altered by mineral dissolution and precipitation. In order to express the relationship between mineral dissolution and precipitation and porosity, consider the following: $\hat{\phi}_{\text{ref}}$ is the reference porosity with mineral precipitation or dissolution, ϕ is the porosity, ϕ_{ref} is the reference porosity without mineral precipitation or dissolution, N_β is the total moles of mineral β per bulk volume, N_β^0 is the total moles of mineral β per bulk volume at time 0, ρ_β is the mineral molar density, c_ϕ is the rock compressibility, and p_{ref} is the reference confining pressure. The relationship between the porosity and mineral precipitation or dissolution can be expressed as:

$$\hat{\phi}_{\text{ref}} = \phi_{\text{ref}} - \sum_{\beta=1}^{\mathrm{n_m}} \left(\frac{\mathrm{N}_\beta}{\rho_\beta} - \frac{\mathrm{N}_\beta^0}{\rho_\beta} \right)$$

The porosity at any confining pressure p different from p_{ref} can be written as:

$$\phi = \hat{\phi}_{\text{ref}} [1 + c_\phi (p_{\text{confining}} - p_{\text{ref,confining}})]$$

The change in porosity due to mineral dissolution and precipitation can be related to the change in absolute permeability for example through the Kozeny-Carman equation. In the following equation, k^0 and ϕ^0 are initial permeability and porosity, respectively.

$$\frac{k}{k^0} = \left(\frac{\phi}{\phi^0}\right)^3 \cdot \left(\frac{1-\phi^0}{1-\phi}\right)^2$$

However, changes in absolute permeability from mineral precipitation and dissolution cannot be modeled using the GEM (© CMG) simulator. Thus, these changes are manually calculated in a spreadsheet and inserted into the simulation to observe the effect of mineral precipitation and dissolution on fluid transport of CO_2.

It can be speculated that the temporal evolution of CO_2 seeps is caused by complete plugging of CO_2 flow path due to mineral precipitation. However, complete plugging of CO_2 flow path, which reduces a grid block porosity to zero, cannot be modeled using a flow simulator because this would make the flow simulation unstable. As a result, a drastic change in direction of CO_2 flow path could not be modeled properly due to the limitation of the simulator. However, flow velocity could still be affected by a partial plugging of grid blocks that CO_2 flows through due to mineral precipitation.

6.3 Simulation Setup

A 2-D simulation model was built to investigate the migration of CO_2 fluid due to mineral precipitation. Figure 6-1 illustrates a 2-D model with 1 injector and 9 producers from a top view; the effect of gravity on CO_2 flow is disregarded with a 2-D horizontal plane. Table 6-1 shows the basic simulation setup parameters. Pore volume of grid blocks is reduced by choosing a small porosity of 0.001; this will help us to observe the impact of mineral precipitation or dissolution on porosity and flow transport. Aqueous solution is injected with 0.2 molality of CO_2 and 0.8 molality of H_2O. Initial conditions of aqueous components, minerals, and others components in the formation are the same as in Chapter 5 and shown in Tables 3-1 to 3-5. The first simulation is run from 2000 to 2010 for a

period of 10 years. The output, effective porosity in 2010, is extracted and used to update the absolute permeability of the grid blocks based on the Kozeny-Carman equation. Then, the updated absolute permeability is input in simulation for next 10 years of simulation from 2010 to 2020 using the restart command in GEM. The results are analyzed and discussed in the subsequent section.

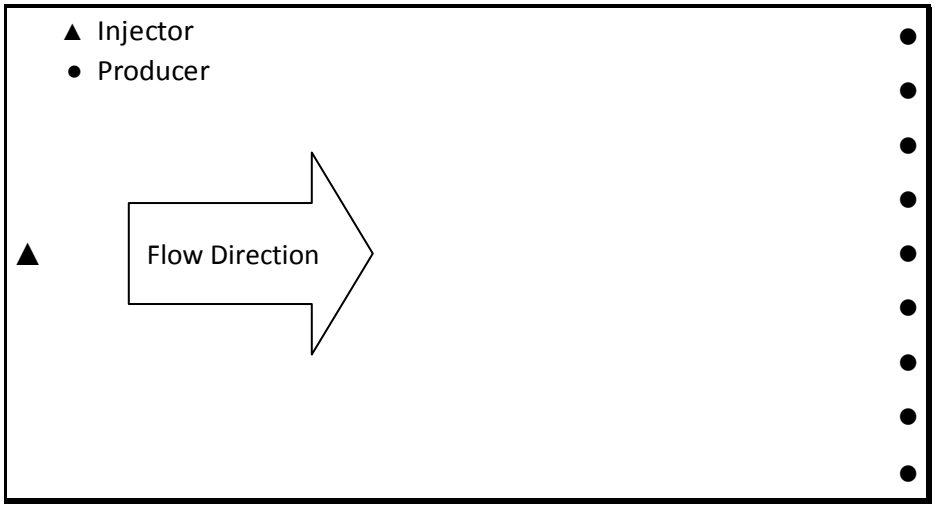

Figure 6-1. Illustration of the 2-D model with 1 injector and 9 producers from a top view.

Model dimensions	10 m x 10 m x 10 m
Grid	20 x 9 x 1
CO_2 injection rate	0.1 m^3/day
Porosity	0.001
Temperature	19.375 ˚C
Pressure	150.1 kPa

Table 6-1. Simulation setup of the 2-D model.

6.4 Results and Discussion

The results from the 2-D model are described and discussed in this section. First, calcite and kaolinite mineralizations for the whole reservoir are shown in Figure 6-2 and Figure 6-3, respectively. Figure 6-2 and Figure 6-3 also illustrate the locations where

kaolinite and calcite precipitations formed in 2010 after 10 years of simulation. Most of the calcite and kaolinite precipitations formed in the upper-right part of the model. Consequently, the biggest reduction in effective porosity was observed in the same area due to mineral precipitation; Figure 6-4 shows the effective porosity in 2010. Then, absolute permeability in 2010 is updated by the effective porosity in 2010 based on the Kozeny-Carman equation. The simulation carried on for next 10 years from 2010 to 2020 using the updated absolute permeability to find out the influence of mineral precipitation on CO_2 transport. Figure 6-5 shows the total velocity magnitude in the x-direction, which is the main direction of flow, at the end of simulation; it shows the decrease in velocity where mineral precipitation formed significantly. Complete plugging of the formation and complete diversion of fluid flow would require running this explicitly-coupled simulation several times over a long duration. However, we were still able to observe the change in fluid flow velocity from mineral precipitation associated with CO_2 which indicates mineral precipitation influences the flow and transport of CO_2.

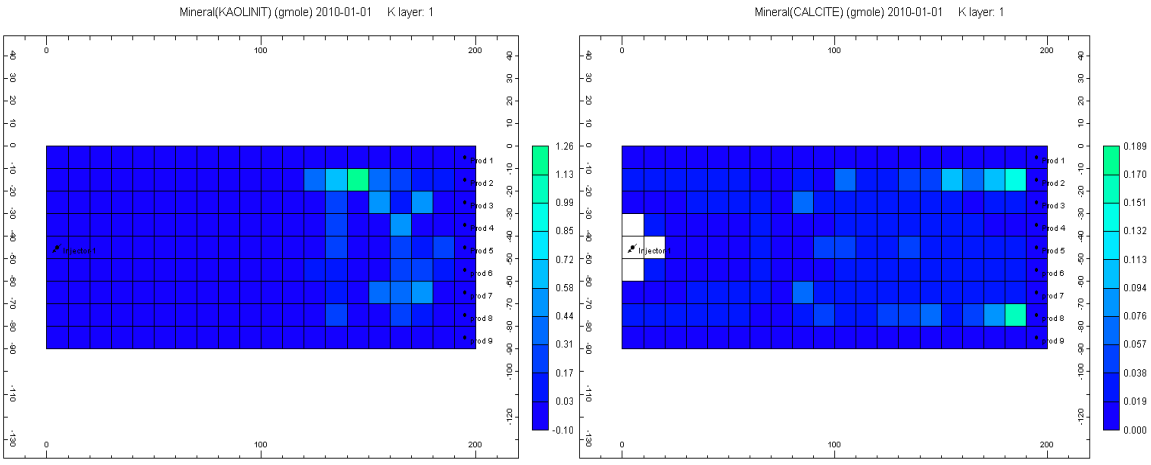

Figure 6-2. Kaolinite mineral precipitation in gram-mole in year 2010.

Figure 6-3. Calcite mineral precipitation in gram-mole in year 2010.

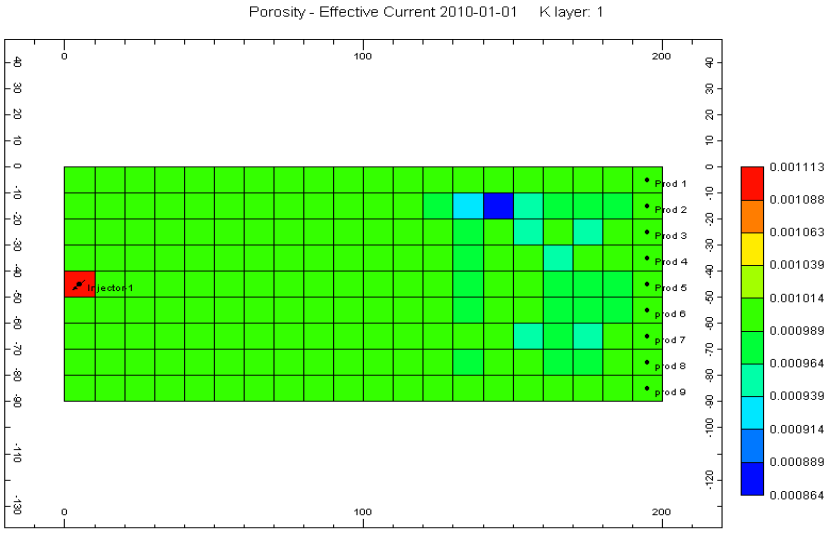

Figure 6-4. Effective porosity in gram-mole in year 2010.

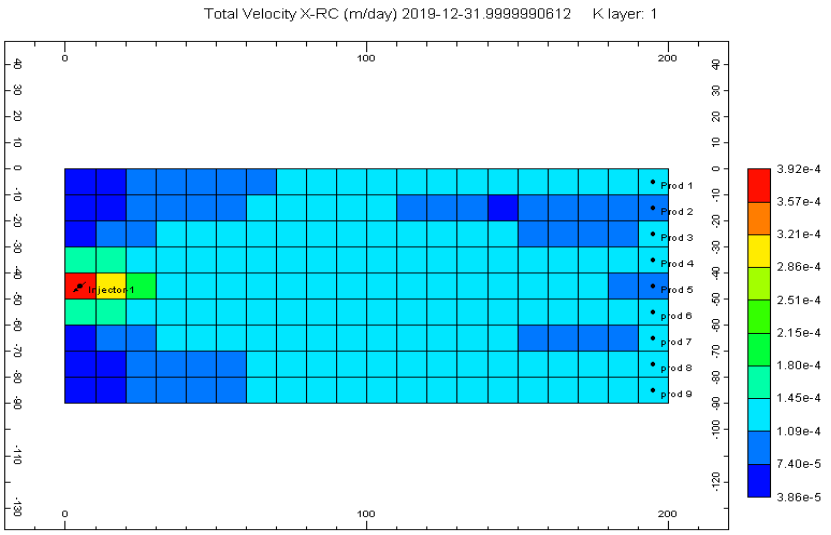

Figure 6-5. Total velocity magnitude in the x-direction in year 2020.

The relationships between calcite and kaolinite precipitations and porosity are obtained using the analytical equations shown in Chapter 6.2. The current size for each grid block is 1000 m^3 with initial porosity of 0.001. Thus, the void volume of the each grid block used in the calculations is 1 m^3 or 1,000,000 cm^3. Table 6-2 shows the density and molar weight of calcite and kaolinite used in the calculations. These data allow us to determine the volume of the mineral precipitation and ultimately relate it to the change in

porosity. As a result, plots of variation in porosity vs. amount of precipitation of calcite and kaolinite are shown in Figure 6-6 and Figure 6-7, respectively. The porosity vs. permeability plot is also acquired based on the Kozeny-Carman equation in Figure 6-8. According to Figure 6-6 and Figure 6-7, about 10 moles of kaolinite or 27 moles of calcite precipitations are needed to plug the whole void volume for each grid block which will reduce permeability of the grid block to zero. However, kaolinite and calcite precipitations stop at some point in the numerical simulation. In other words, mineral precipitations do not increase after some duration of the simulation. This is due to the fact that quantities of calcite and kaolinite precipitations that can form from the geochemistry associated with CO_2 also depend on the availability of Ca^{2+}, $SiO_{2\,(aq)}$, and Al^{3+} aqueous components in formation. These aqueous components are assumed to be the limiting factor for calcite and kaolinite precipitations in our case because amounts of minerals for dissolution and these aqueous components are confined initially in GEM. Initial aqueous components and minerals in formation influence the quantities of mineral precipitations that can possibly form and, therefore, these initial conditions of reservoir formation also decide the likelihood of plugging the CO_2 flow paths due to mineral precipitations.

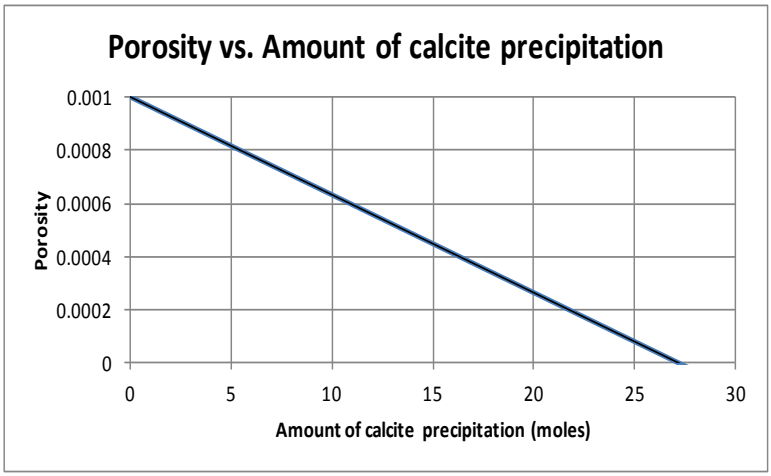

Figure 6-6. Variation in porosity as a function of amount of calcite mineral precipitation for a simulation model with initial porosity of 0.001 and void volume of 1 m^3 for each grid block.

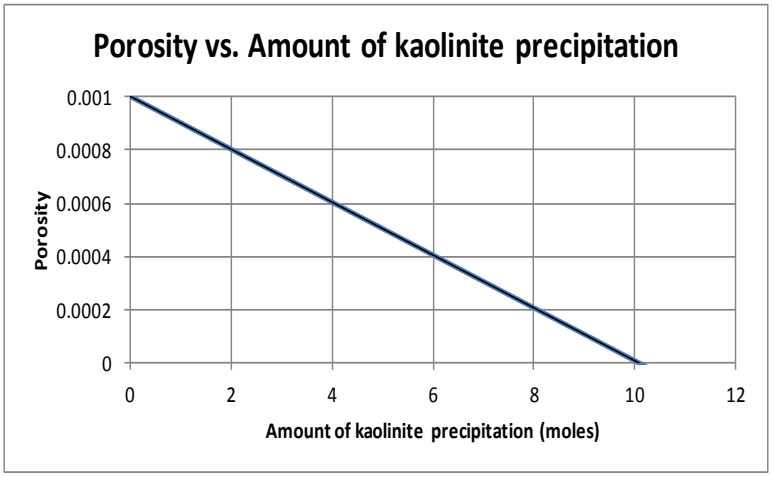

Figure 6-7. Variation in porosity as a function of amount of kaolinite mineral precipitation in a model with initial porosity of 0.001 and void volume of 1 m^3 for each grid block.

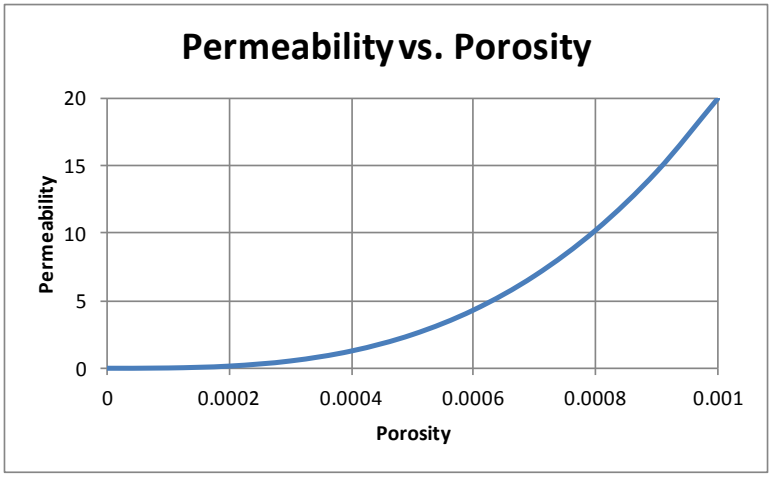

Figure 6-8. Variation in permeability over the range of altered porosity due to mineral precipitation.

	Calcite	Kaolinite
Density (g/cm^3)	2.711	2.6
Molar weight (g/mol)	100.0869	258.2

Table 6-2. Density and molar weight of calcite and kaolinite.

6.5 Percolation Model for Modeling Impact of Geochemical Alterations

Percolation theory has been widely used to understand and model the connectivity characteristics of porous media because it describes the behavior of connected clusters in complex systems (Sahimi, 1994). A porous medium in reality is heterogeneous and is composed of different sizes of pores in a seemingly disordered manner and so it is appropriate to talk about the average connectivity characteristics of rocks with different spatial distribution of pore bodies. It is in this context that percolation theory is applied in this chapter to model the transport phenomena of CO_2 in a complex porous medium with mineral precipitations.

A 2D model with different sizes of pores is constructed using MATLAB; the MATLAB code is included in Appendix B.3.1. The model only contains a total number of 10,000 pores, 100x100 in the x and y directions, due to the computational costs. The pore size distribution used in this chapter is shown in Figure 6-9 and is estimated from the pore size distribution of a Berea sandstone sample obtained by Hg porosimetry (Song, 2010). Using the pore size distribution in Figure 6-9, 10,000 different sizes of pores are sampled randomly and assigned to the site nodes in the percolation model.

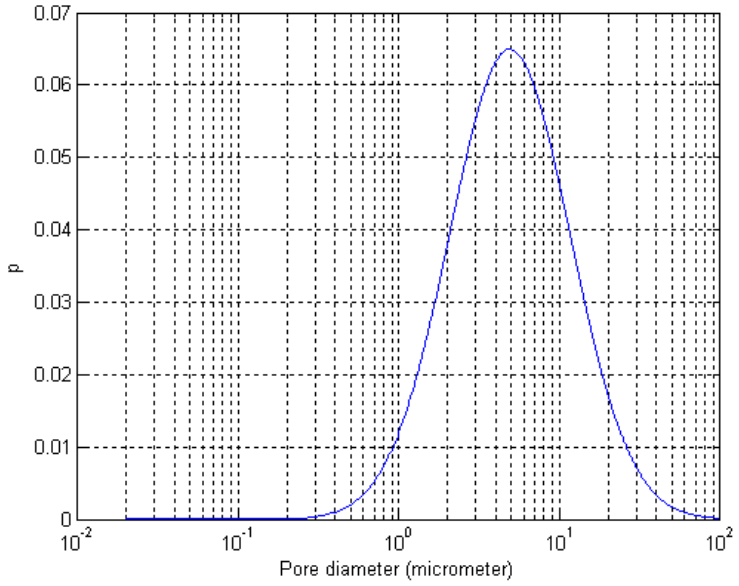

Figure 6-9. The pore size distribution.

All the pores are initially open and connected as shown in Figure 6-10 (left). Then, calcite precipitations occur due to the geochemical reactions with CO_2; the precipitations are assumed to be distributed uniformly throughout the model. Corresponding to a bulk amount of precipitations, a random selection of pores is closed as shown in Figure 6-10 (middle). Then, the disconnected paths due to the precipitations are identified in different colors in Figure 6-10 (right).

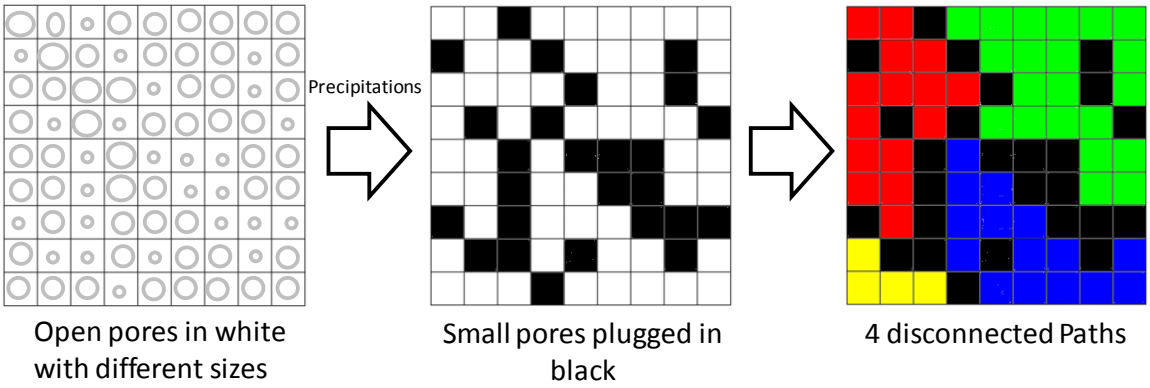

Figure 6-10. Illustration of the Percolation model with precipitations.

Based on the pore diameters, pore volume of the entire model is calculated assuming that the pore is a sphere. Pore volume is estimated to be around 0.0013 cm^3. Then, the maximum amounts of calcite mineral that can be precipitated in this model is computed to be 3.4328×10^{-5} mole which will fill up the entire pore volume of the model. Different amounts of calcite mineral are assumed to be precipitated and the numbers of disconnected paths due to these precipitations are obtained, accordingly. A plot of number of disconnected paths vs. calcite precipitation in gram-mole is obtained in Figure 6-11; as the amount of precipitations increases, the number of disconnected path also increases due to the plugging. Figure 6-12 visualizes the plugged pores in white and the disconnected paths in different colors. Most pores and flow paths are connected up to 3×10^{-7} gram-mole of calcite precipitation; as a result of high flow connectivity, there are countless numbers of the spanning paths, in which fluids can be transported from one end to the other end in this model. However, flow paths start showing lack of connectivity

above 6×10^{-7} gram-mole of calcite precipitation. For example, over 400 disconnected paths are identified with 8×10^{-7} gram-mole of calcite precipitation in Figure 6-12. This is also shown in Figure 4 as disconnected paths in different colors.

It is also verified that the pore volume does not need to be completely plugged in the model to achieve a complete disconnection of flow paths from one end to the other end. Figure 6-13 shows the histogram of the amounts of calcite precipitation that results in complete disconnection of the flows paths from one end to the other end in the north-south and east-west directions from 500 trials. These 500 trials or realizations represent the variability in connectivity characteristics due to the uncertainty in the spatial distribution of plugged pores. The percentage of plugged pores in the model is plotted against the calcite precipitation in Figure 6-14. On the average, about 3.25×10^{-7} gram-mole of calcite precipitation is needed for complete disconnection and zero spanning flow path, and this amount of calcite precipitations plugs about 30% of the initial existing pores based on our analysis. In other words, flow paths do not require all the pores but only about 30% of the pores to be plugged for complete disconnection from one end to the other end in our model. The percolation results indicate that flow re-routing due to mineral precipitations are possible at the pore scale which could possibly lead to lateral migration of CO_2 seeps. In reality, the amount of calcite precipitation required, the percentage of plugged pores, and the time to achieve zero spanning flow path will depend on the size and network of actual CO_2 flow path in a reservoir.

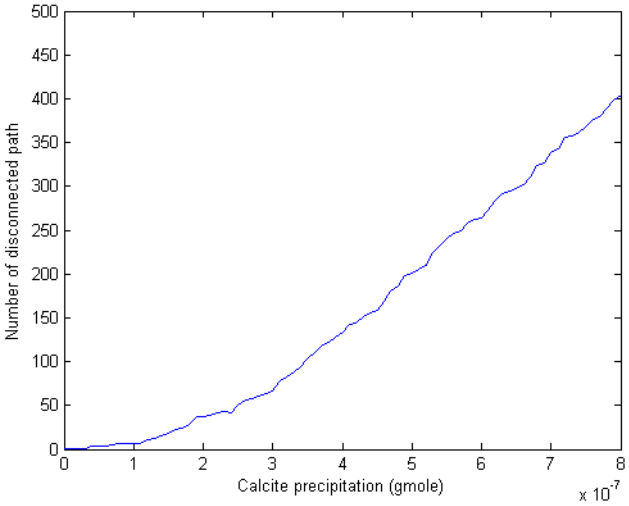

Figure 6-11. Number of disconnected paths vs. calcite precipitation in gram-mole.

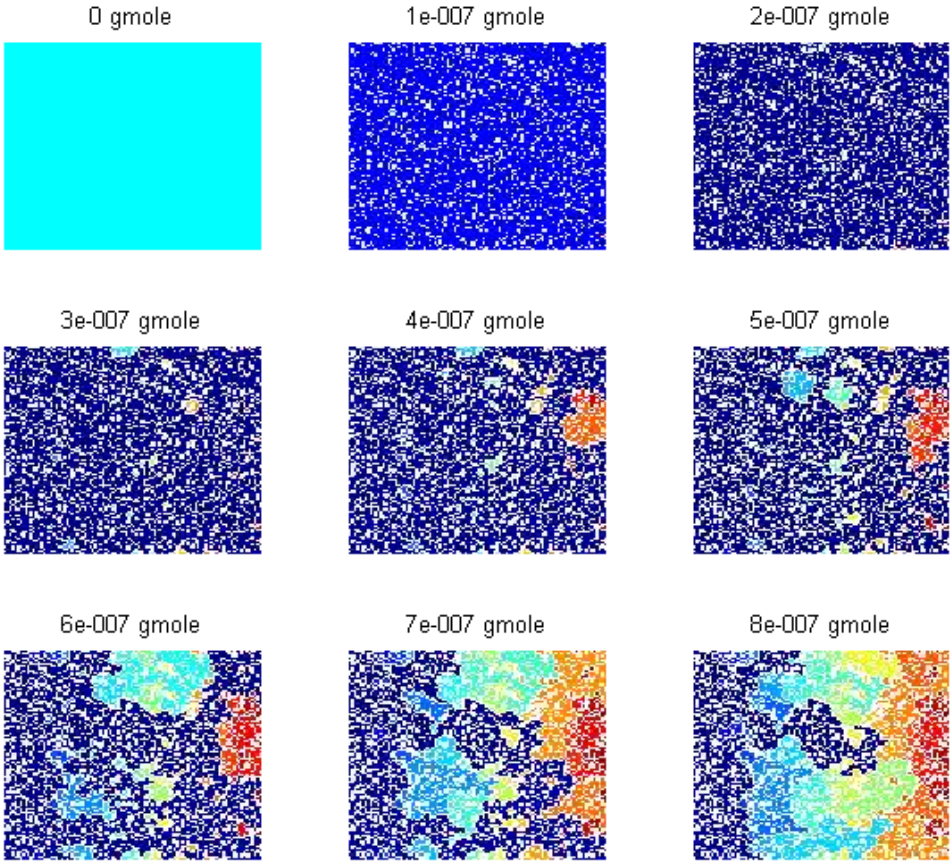

Figure 6-12. Plugged pores in white and disconnected paths in different colors as a function of the amount of calcite precipitations in gram-mole.

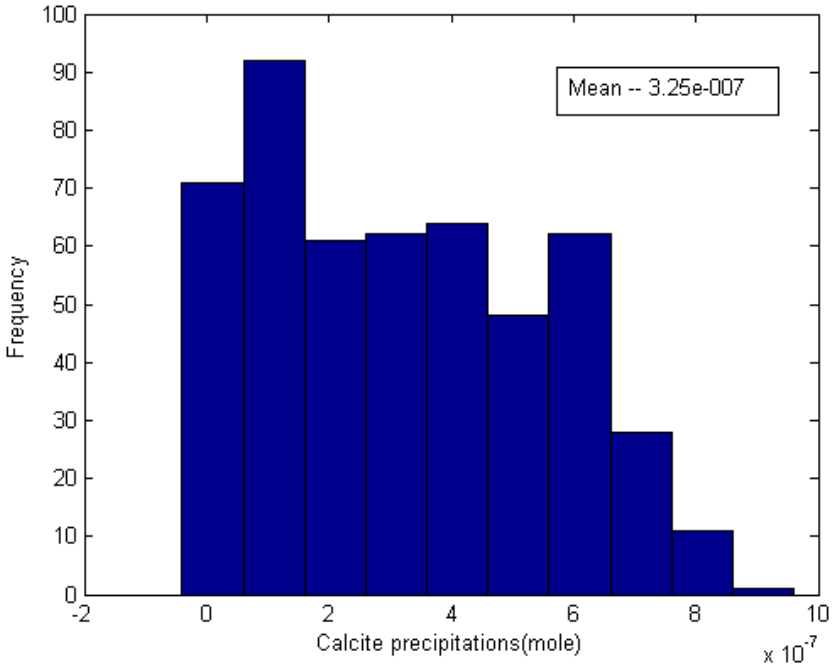

Figure 6-13. Histogram of calcite precipitations over 500 trials that completely disconnect the flow paths from one end to the other end in the percolation model.

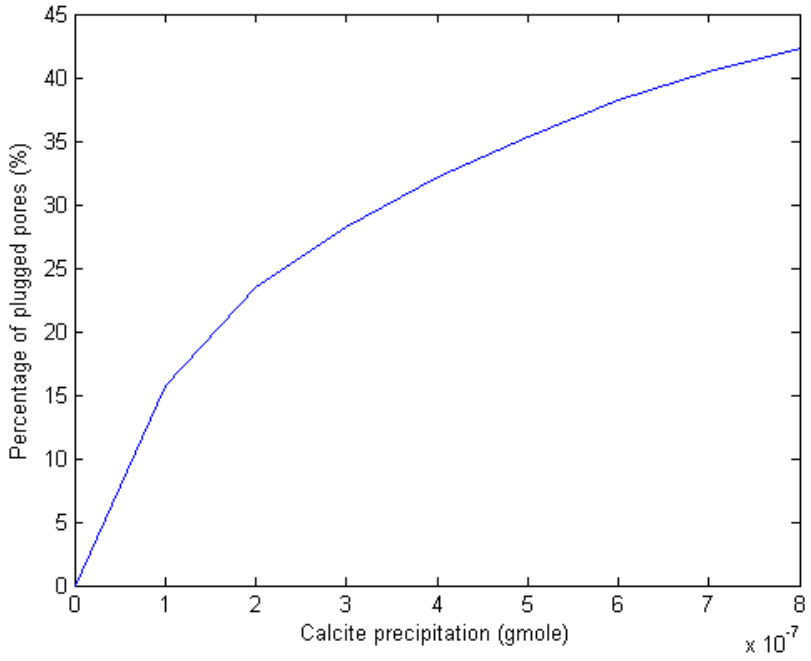

Figure 6-14. Percentage of plugged pores vs. calcite precipitation in gram-mole.

6.6 Conclusions

From the reservoir simulation studies in the 2-D model, it is evident that fluid flow of CO_2 in subsurface could be affected by the mineral precipitations. In reality, if complete plugging of the pore spaces happens due to mineral precipitations, then diversion of CO_2 flow from the original migration path is possible which could results in temporal migration of CO_2 seeps at field site as CO_2 leaks to the surface. However, further modeling and laboratory experiments are required to confirm this phenomenon.

Chapter 7 : Conclusions and Recommendations for Future Work

7.1 Conclusions

Active CO_2 seeps as well as locations of ancient seeps are observed at the Crystal Geyser site. We were interested in these events because they present a surface expression of CO_2 leakage. The key objectives of this research work were:

1. To find the main mechanisms and effects associated with CO_2 flow and transport in the subsurface
2. To model and investigate the spatial and temporal observations of CO_2 seeps at the Crystal Geyser site

The reservoir and geochemical models for the research study were built using the compositional simulator GEM (© Computer Modeling Group). Geological information, such as the stratigraphy of the formation and geochemical reaction parameters including aqueous and mineral compositions, were obtained from the literature and presented in Chapter 3. Based on the surface observation of travertine mounds at the Crystal Geyser site, a suite of probable geochemical reactions were adopted in modeling. For the fulfillment of the first objective, a base cross-sectional model was described in Chapter 4 to simulate CO_2 gas leakage and to study the dissolution mechanism of CO_2 gas when CO_2 is transported through a fault system. The simulation results demonstrate the effect of change in pressure on the solubility of CO_2 in brine when CO_2-saturated brine is flowing through the fault system that results in the ex-solution of CO_2 gas. Sensitivity studies were conducted to determine the effects of fault properties on the amount of CO_2 gas leakage. The effects of fault offset and permeability on CO_2 gas leakage through a fault system are also presented in Chapter 4.

For the second objective, 3-D models with accurate description of the geochemistry associated with CO_2 were built and described in Chapter 5. The fault system is very heterogeneous which is composed of thousands of different sub-segments and materials. A Sequential Gaussian simulation was implemented to characterize the

heterogeneous fault system in these models. Multiple realizations of the fault system were generated for the simulation studies. Two probable sources of CO_2 at the Crystal Geyser site were studied and incorporated in modeling; the deep crustal CO_2 and the regional flow of CO_2-dissolved groundwater. Carbonate mineralization occurred along the fault from the geochemical reactions associated with CO_2 and the mineral precipitations reduced the void pore space and consequently effective porosity. Here is the list of key conclusions in this paper.

- The simulation results from the 2-D model in Chapter 4 suggest that the release of CO_2 gas from groundwater due to the pressure drop during vertical transit through the fault could be a mechanism for CO_2 gas leakage along the fault.
- Different results are observed for the two cases in terms of the surface expression of CO_2 leakage and calcite precipitation. These simulations could be used as the framework for modeling the spatial location of the CO_2 seeps and travertine mounds observed at the Crystal geyser site.
- The GEM model for the diversion of CO_2 flow showed the change in fluid flow velocity from mineral precipitations associated with CO_2 which indicates mineral precipitations influences the flow and transport of CO_2. Furthermore, the percolation results indicate that flow re-routing due to mineral precipitations are possible at the pore scale which could possibly lead to lateral migration of CO_2 seeps.

7.2 Recommendations for Future Work

The work in this thesis is fairly new and requires further research. Based on the results of this thesis and some previous work, here are some recommendations and suggestions for future work:

- The brine composition, initial mineral composition, rock mineralogy, and aqueous components concentrations used for the geochemical modeling of the CO_2 seeps at the Crystal Geyser site were estimated from the other field sites in literature.

Also, significant uncertainty exists in estimating the parameters of heterogeneous geochemical reactions such as surface reactive area and chemical equilibrium constant. Therefore, modeling may not perfectly represent the actual subsurface processes in the field due to a lack of geochemical data. It is recommended to obtain these geochemical parameters by directly performing experiments with rock samples from the field using the brine collected in the field. This would give us a better idea of actual geochemical reactions occurring in subsurface. Ultimately, more accurate modeling would provide much needed information about the CO_2 seeps.

- A fault system has a major role in underground CO_2 leakage. Thus, fault modeling is very important when we model the CO_2 seeps at the Crystal Geyser site. However, a fault system is very heterogeneous and hard to model accurately. In this research, a geostatistical technique, Sequential Gaussian simulation was used to model the spatial variability in the flow properties of the fault system. However, due to a lack of data availability on the fault system, there is still significant uncertainty associated with this model. More data is needed about the fault system. Also, if CO_2 production data and location of both active and inactive CO_2 seeps in the past are available, history matching could be done with multiple realizations of the fault system to find the best match that reproduces both historical and present activity of the CO_2 seeps at the Crystal Geyser site.
- Current and inactive CO_2 seeps indicate that the flow path and migration of CO_2 in subsurface have changed in the past and will change in future as well. Many researchers believe that the change in flow path of CO_2 may be caused by several events including earthquakes, surface deformation, and mineralization. Specifically, surface structure and topography of the field site such as erosion by the meandering river significantly influence the locations of active and inactive CO_2 seeps. Therefore, we recommend incorporating these aspects of topography at the field site accurately for modeling CO_2 seeps.

- An attempt was made to model the plugging of the formation and self-sealing of CO_2 flow pathways due to mineralization in GEM. However, GEM was not able to perfectly model the self-sealing mechanism of CO_2. A percolation model was implemented to better represent the mechanism of flow blockage and diversion. However, that model was essentially at the scale of pore bodies. A systematic scheme for computing the effective flow property of the grid blocks taking into account the plugging mechanism would be imperative to investigate and understand the self-sealing mechanisms associated with CO_2 transport through cracks and faults.

Appendix A: Stochastic Modeling of a Heterogeneous Fault System

A.1 Overview

Any existing fault system is composed of many sub-compartments with various materials which have different properties such as permeability. These properties for the sub-compartments in a fault system are immeasurable because the sub-compartments and its fracture networks are too complex and heterogeneous in subsurface. It is impractical to extract the fault properties such as permeability from direct sampling for each segment and to model the entire fault system. Therefore, a stochastic method is approached to model and characterize the entire heterogeneous fault system in this paper. The Stanford Geostatistical Modeling Software (SGEMS) is used to perform the Geostatistical analysis, a Sequential Gaussian simulation, for characterizing the fault system in modeling.

A.2 Characterization of a Fault System

A stochastic method is used to characterize the fault system in SGEMS; initial permeability values at several locations (hard data) are estimated and variograms at different directions are created to perform a Sequential Gaussian simulation (Deutsch and Journel, 1992) for generating values of the fault permeability at each block.

The grid blocks for the fault system are created in SGEMS. The fault blocks and its locations are shown from a top and 3-D view in Figure A-1 and in Figure A-2, respectively. There are 20 blocks in the x-direction, 3 blocks in the y-direction, and 19 blocks in the z-direction for the fault system: a total 1140 blocks. In SGEMS, a rectangular-shaped grid block with dimensions of 20x3x19 is created for the fault system and shown in Figure A-3. The fault blocks in GEM are slanted from the South-West to the North-East direction as shown in Figure A-1 and Figure A-2, which is not a straight rectangular shape. Thus, the realizations in SGEMS for rectangular-shaped fault system were translated to the fault blocks in GEM. Also, GEM has a different coordinate system from the coordinate system in SGEMS. Therefore, the realizations produced in SGEMS

for permeability values of the fault blocks are re-coordinated into the GEM coordinate system when it's transported to GEM.

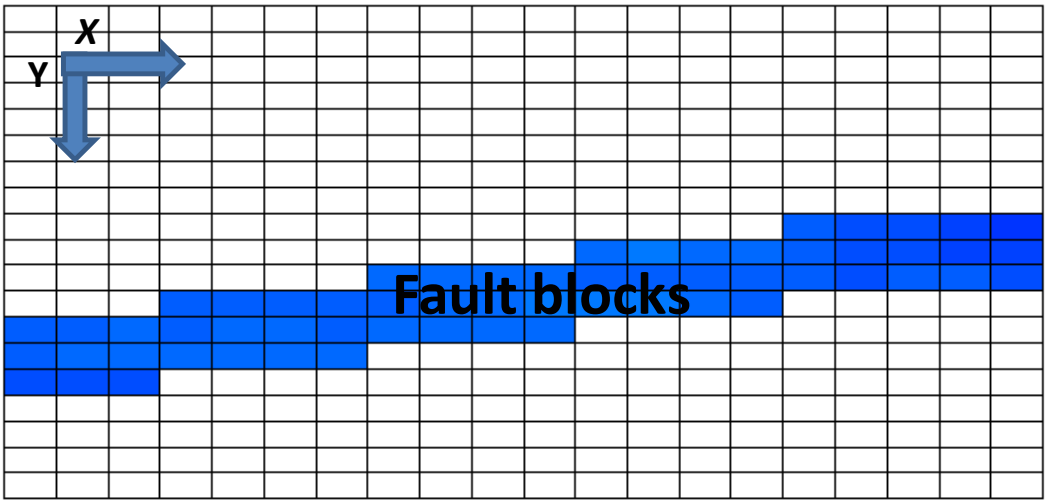

Figure A-1. Fault blocks in a top view.

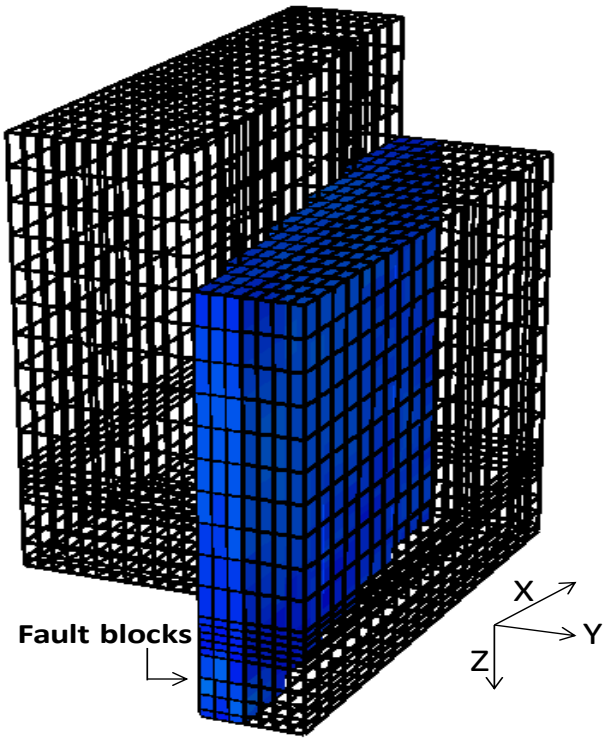

Figure A-2. Fault blocks in a 3-D view.

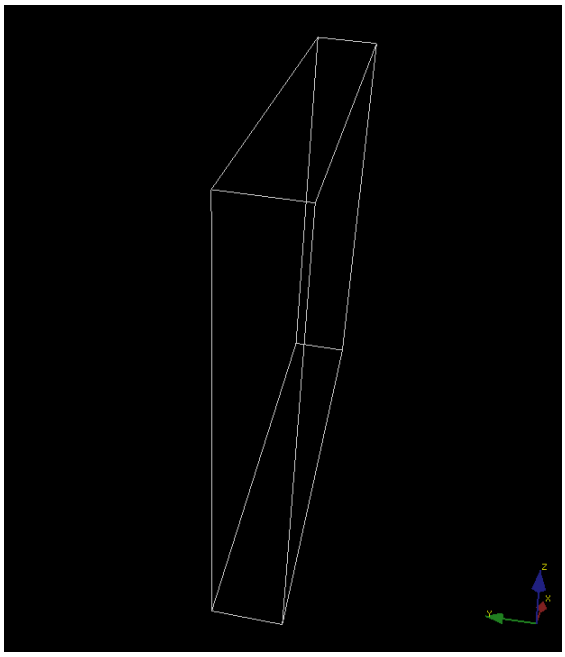

Figure A-3. Rectangular-shape fault grid blocks in SGEMS 3-D view.

A.2.1 Hard Data

Permeability values are estimated at arbitrary locations; by looking at the stratigraphy information around the fault system in Table 3-1. We assume that the fault blocks adjacent to shale layers are more impermeable due to possibility of shale erosion into the fault system than the fault blocks adjacent to sand layers. The input data for the Sequential Gaussian simulation, which is hard permeability values at arbitrary locations, are shown in following.

```
--------------------------
Hard data
4
X
Y
Z
Permeability in Fault (md)
1       1       3       23
5       1       2       20
12      1       0       24
16      1       4       14
19      1       5       20
6       1       15      15
7       1       18      19
9       1       11      17
10      1       6       21
```

```
11      1       8       15
0       1       16      25
15      1       13      16
18      1       17      17
3       1       10      19
17      1       9       22
0       0       18      5
1       0       10      7
2       0       14      3
3       0       12      5
5       0       16      4
8       0       15      1
12      0       11      4
3       2       12      5
1       2       13      8
8       2       10      10
12      2       18      13
17      2       15      14
14      2       9       9
19      2       7       7
2       2       16      6
-----------------------
```

A.2.2 Realizations

The hard data is used to produce variograms at different directions and the Sequential Gaussian simulation is implemented in SGEMS to characterize the fault system. Multiple realizations for the fault blocks could be generated. One of the realizations for the fault characterization is exported from SGEMS into GEM and used in Chapter 5.

Appendix B : Input Files

B.1 Deep Crustal CO_2 Case

```
**------------------------------- Input/Output -------------------------------**

FILENAMES OUTPUT SRFOUT RESTARTOUT INDEXOUT MAINRESULTSOUT
INUNIT SI
INTERRUPT INTERACTIVE
XDR ON
MAXERROR 20
RANGECHECK ON
WRST 365
WPRN WELL TIME
WPRN GRID TIME
WPRN ITER MATRIX
WSRF WELL 1
WSRF GRID TIME
OUTSRF WELL PSPLIT
DIARY CHANGES
OUTPRN WELL ALL
OUTPRN RES NONE
OUTPRN GRID MINERAL 'ANORTHIT' MINERAL 'CALCITE' MINERAL 'KAOLINIT' MOLALITY
'CO2' POROS PRES TEMP W 'CO2' X 'CO2' Y 'CO2'
OUTSRF GRID DENG DENW DPORMNR MINERAL 'ANORTHIT' MINERAL 'CALCITE' MINERAL
'KAOLINIT' MOLALITY 'Al+++' MOLALITY 'CO2' MOLALITY 'CO3--' MOLALITY 'Ca++'
MOLALITY 'H+' MOLALITY 'HCO3-' MOLALITY 'OH-' MOLALITY 'SiO2(aq)' PH POROS PRES
SG SO SW TEMP VELOCRC W 'C1' W 'CO2' X 'C1' X 'CO2' Y 'C1' Y 'CO2' Z 'C1' Z
'CO2'
OUTSRF WELL GHGAQU GHGGAS GHGSCRIT GHGMNR GHGSOL GHGLIQ
OUTSRF RES ALL
RESULTS XOFFSET           0.0000
RESULTS YOFFSET           0.0000
RESULTS ROTATION          0.0000
RESULTS AXES-DIRECTIONS 1.0 -1.0 1.0

**---------------------------------- Grid ----------------------------------**

GRID VARI 20 19 19
KDIR DOWN
DI CON 15
DJ CON 7.5
DK ALL
3800*20 1900*5 380*15 380*11 380*10 380*5
DTOP
0      0      0      0      0      0      0      0      0      0      0      0
0      0      0      0      0      0      0      0      0      0      0      0
0      0      0      0      0      0      0      0      0      0      0      0
0      0      0      0      0      0      0      0      0      0      0      0
0      0      0      0      0      0      0      0      0      0      0      0
0      0      0      0      0      0      0      0      0      0      0      0
0      0      0      0      0      0      0      0      0      0      0      0
0      0      0      0      0      0      0      0      0      0      0      0
0      0      0      0      0      0      0      0      0      0      0      0
0      0      0      0      0      0      0      0      0      0      0      0
0      0      0      0      0      0      0      0      0      0      0      0
0      0      0      0      0      0      0      0      0      0      0      0
0      0      0      0      0      0      0      0      0      0      0      0
```

```
0      80     80     80     80     80     80     80     80     80     80     80
0      80     80     80     80     80     80     80     80     80     80     80
0      80     80     80     80     80     80     80     80     80     80     80
0      80     80     80     80     80     80     80     80     80     80     80
0      80     80     80     80     80     80     80     80     80     80     80
0      0      80     80     80     80     80     80     80     80     80     80
0      0      0      80     80     80     80     80     80     80     80     80
0      0      0      0      80     80     80     80     80     80     80     80
0      0      0      0      80     80     80     80     80     80     80     80
0      0      0      0      80     80     80     80     80     80     80     80
0      0      0      80     80     80     80     80     80     80     80     80
0      0      0      80     80     80     80     80     80     80     80     80
0      0      0      80     80     80     80     80     80     80     80     80
0      0      80     80     80     80     80     80     80     80     80     80
0      0      80     80     80     80     80     80     80     80     80     80
0      0      80     80     80     80     80     80     80     80     80
0      80     80     80     80     80     80     80     80     80     80
0      80     80     80     80     80     80     80     80     80     80
0      80     80     80     80     80     80     80     80     80     80
NULL CON 1
POR CON .2
PERMI ALL
INCLUDE 'perm.dat'
**perm.dat has 7,220 permeability values for all the blocks (20x19x19):
**it includes the heterogeneous fault from Appendix A and both sand and shale
layers
PERMJ EQUALSI
PERMK EQUALSI
PINCHOUTARRAY CON 1
CPOR  MATRIX   1.E-08
PRPOR MATRIX   1000.

**-------------------------- Infinite Acting Boundary ----------------------**

VOLMOD IJK      6 19 13 30000   12 19 15 30000  18 19 17 30000  4 1 11 30000
1 19 11 30000   7 19 13 30000   13 19 15 30000  19 19 17 30000  5 1 11 30000
2 19 11 30000   8 19 13 30000   14 19 15 30000  20 19 17 30000  6 1 11 30000
3 19 11 30000   9 19 13 30000   15 19 15 30000  1 19 19 30000   7 1 11 30000
4 19 11 30000   10 19 13 30000  16 19 15 30000  2 19 19 30000   8 1 11 30000
5 19 11 30000   11 19 13 30000  17 19 15 30000  3 19 19 30000   9 1 11 30000
6 19 11 30000   12 19 13 30000  18 19 15 30000  4 19 19 30000   10 1 11 30000
7 19 11 30000   13 19 13 30000  19 19 15 30000  5 19 19 30000   11 1 11 30000
8 19 11 30000   14 19 13 30000  20 19 15 30000  6 19 19 30000   12 1 11 30000
9 19 11 30000   15 19 13 30000  1 19 17 30000   7 19 19 30000   13 1 11 30000
10 19 11 30000  16 19 13 30000  2 19 17 30000   8 19 19 30000   14 1 11 30000
11 19 11 30000  17 19 13 30000  3 19 17 30000   9 19 19 30000   15 1 11 30000
12 19 11 30000  18 19 13 30000  4 19 17 30000   10 19 19 30000  16 1 11 30000
13 19 11 30000  19 19 13 30000  5 19 17 30000   11 19 19 30000  17 1 11 30000
14 19 11 30000  20 19 13 30000  6 19 17 30000   12 19 19 30000  18 1 11 30000
15 19 11 30000  1 19 15 30000   7 19 17 30000   13 19 19 30000  19 1 11 30000
16 19 11 30000  2 19 15 30000   8 19 17 30000   14 19 19 30000  20 1 11 30000
17 19 11 30000  3 19 15 30000   9 19 17 30000   15 19 19 30000  1 1 13 30000
18 19 11 30000  4 19 15 30000   10 19 17 30000  16 19 19 30000  2 1 13 30000
19 19 11 30000  5 19 15 30000   11 19 17 30000  17 19 19 30000  3 1 13 30000
20 19 11 30000  6 19 15 30000   12 19 17 30000  18 19 19 30000  4 1 13 30000
1 19 13 30000   7 19 15 30000   13 19 17 30000  19 19 19 30000  5 1 13 30000
2 19 13 30000   8 19 15 30000   14 19 17 30000  20 19 19 30000  6 1 13 30000
3 19 13 30000   9 19 15 30000   15 19 17 30000  1 1 11 30000    7 1 13 30000
4 19 13 30000   10 19 15 30000  16 19 17 30000  2 1 11 30000    8 1 13 30000
5 19 13 30000   11 19 15 30000  17 19 17 30000  3 1 11 30000    9 1 13 30000
```

```
10 1 13 30000   10 1 19 30000   1 17 15 30000   20 9 17 30000   20 18 11 30000
11 1 13 30000   11 1 19 30000   1 18 15 30000   20 10 17 30000  1 13 1 30000
12 1 13 30000   12 1 19 30000   1 2 13 30000    20 11 17 30000  2 13 1 30000
13 1 13 30000   13 1 19 30000   1 3 13 30000    20 12 17 30000  3 13 1 30000
14 1 13 30000   14 1 19 30000   1 4 13 30000    20 13 17 30000  4 13 1 30000
15 1 13 30000   15 1 19 30000   1 5 13 30000    20 14 17 30000  5 13 1 30000
16 1 13 30000   16 1 19 30000   1 6 13 30000    20 15 17 30000  6 13 1 30000
17 1 13 30000   17 1 19 30000   1 7 13 30000    20 16 17 30000  7 13 1 30000
18 1 13 30000   18 1 19 30000   1 8 13 30000    20 17 17 30000  8 13 1 30000
19 1 13 30000   19 1 19 30000   1 9 13 30000    20 18 17 30000  9 13 1 30000
20 1 13 30000   20 1 19 30000   1 10 13 30000   20 2 15 30000   10 13 1 30000
1 1 15 30000    1 2 19 30000    1 11 13 30000   20 3 15 30000   11 13 1 30000
2 1 15 30000    1 3 19 30000    1 12 13 30000   20 4 15 30000   12 13 1 30000
3 1 15 30000    1 4 19 30000    1 13 13 30000   20 5 15 30000   1 14 1 30000
4 1 15 30000    1 5 19 30000    1 14 13 30000   20 6 15 30000   2 14 1 30000
5 1 15 30000    1 6 19 30000    1 15 13 30000   20 7 15 30000   3 14 1 30000
6 1 15 30000    1 7 19 30000    1 16 13 30000   20 8 15 30000   4 14 1 30000
7 1 15 30000    1 8 19 30000    1 17 13 30000   20 9 15 30000   5 14 1 30000
8 1 15 30000    1 9 19 30000    1 18 13 30000   20 10 15 30000  6 14 1 30000
9 1 15 30000    1 10 19 30000   1 2 11 30000    20 11 15 30000  7 14 1 30000
10 1 15 30000   1 11 19 30000   1 3 11 30000    20 12 15 30000  8 14 1 30000
11 1 15 30000   1 12 19 30000   1 4 11 30000    20 13 15 30000  1 15 1 30000
12 1 15 30000   1 13 19 30000   1 5 11 30000    20 14 15 30000  2 15 1 30000
13 1 15 30000   1 14 19 30000   1 6 11 30000    20 15 15 30000  3 15 1 30000
14 1 15 30000   1 15 19 30000   1 7 11 30000    20 16 15 30000  4 15 1 30000
15 1 15 30000   1 16 19 30000   1 8 11 30000    20 17 15 30000  4 12 1 30000
16 1 15 30000   1 17 19 30000   1 9 11 30000    20 18 15 30000  5 12 1 30000
17 1 15 30000   1 18 19 30000   1 10 11 30000   20 2 13 30000   6 12 1 30000
18 1 15 30000   1 2 17 30000    1 11 11 30000   20 3 13 30000   7 12 1 30000
19 1 15 30000   1 3 17 30000    1 12 11 30000   20 4 13 30000   8 12 1 30000
20 1 15 30000   1 4 17 30000    1 13 11 30000   20 5 13 30000   9 12 1 30000
1 1 17 30000    1 5 17 30000    1 14 11 30000   20 6 13 30000   10 12 1 30000
2 1 17 30000    1 6 17 30000    1 15 11 30000   20 7 13 30000   11 12 1 30000
3 1 17 30000    1 7 17 30000    1 16 11 30000   20 8 13 30000   12 12 1 30000
4 1 17 30000    1 8 17 30000    1 17 11 30000   20 9 13 30000   13 12 1 30000
5 1 17 30000    1 9 17 30000    1 18 11 30000   20 10 13 30000  14 12 1 30000
6 1 17 30000    1 10 17 30000   20 2 19 30000   20 11 13 30000  15 12 1 30000
7 1 17 30000    1 11 17 30000   20 3 19 30000   20 12 13 30000  16 12 1 30000
8 1 17 30000    1 12 17 30000   20 4 19 30000   20 13 13 30000  8 11 1 30000
9 1 17 30000    1 13 17 30000   20 5 19 30000   20 14 13 30000  9 11 1 30000
10 1 17 30000   1 14 17 30000   20 6 19 30000   20 15 13 30000  10 11 1 30000
11 1 17 30000   1 15 17 30000   20 7 19 30000   20 16 13 30000  11 11 1 30000
12 1 17 30000   1 16 17 30000   20 8 19 30000   20 17 13 30000  12 11 1 30000
13 1 17 30000   1 17 17 30000   20 9 19 30000   20 18 13 30000  13 11 1 30000
14 1 17 30000   1 18 17 30000   20 10 19 30000  20 2 11 30000   14 11 1 30000
15 1 17 30000   1 2 15 30000    20 11 19 30000  20 3 11 30000   15 11 1 30000
16 1 17 30000   1 3 15 30000    20 12 19 30000  20 4 11 30000   16 11 1 30000
17 1 17 30000   1 4 15 30000    20 13 19 30000  20 5 11 30000   17 11 1 30000
18 1 17 30000   1 5 15 30000    20 14 19 30000  20 6 11 30000   18 11 1 30000
19 1 17 30000   1 6 15 30000    20 15 19 30000  20 7 11 30000   19 11 1 30000
20 1 17 30000   1 7 15 30000    20 16 19 30000  20 8 11 30000   20 11 1 30000
1 1 19 30000    1 8 15 30000    20 17 19 30000  20 9 11 30000   12 10 1 30000
2 1 19 30000    1 9 15 30000    20 18 19 30000  20 10 11 30000  13 10 1 30000
3 1 19 30000    1 10 15 30000   20 2 17 30000   20 11 11 30000  14 10 1 30000
4 1 19 30000    1 11 15 30000   20 3 17 30000   20 12 11 30000  15 10 1 30000
5 1 19 30000    1 12 15 30000   20 4 17 30000   20 13 11 30000  16 10 1 30000
6 1 19 30000    1 13 15 30000   20 5 17 30000   20 14 11 30000  17 10 1 30000
7 1 19 30000    1 14 15 30000   20 6 17 30000   20 15 11 30000  18 10 1 30000
8 1 19 30000    1 15 15 30000   20 7 17 30000   20 16 11 30000  19 10 1 30000
9 1 19 30000    1 16 15 30000   20 8 17 30000   20 17 11 30000  20 10 1 30000
```

```
16 9 1 30000    17 9 1 30000    18 9 1 30000    19 9 1 30000    20 9 1 30000

**------------------------------ Fluid Model -------------------------------**

MODEL PR
NC 2 2
COMPNAME 'CO2' 'C1'
HCFLAG
0 0
VISCOR HZYT
MIXVC 1.0000000E+00
VISCOEFF 1.0230000E-01 2.3364000E-02 5.8533000E-02 -4.0758000E-02 9.3324000E-03
PVC3   1.2000000E+00
MW     4.4010000E+01 1.6043000E+01
AC     2.2500000E-01 8.0000000E-03
PCRIT  7.2800000E+01 4.5400000E+01
VCRIT  9.4000000E-02 9.9000000E-02
TCRIT  3.0420000E+02 1.9060000E+02
PCHOR  7.8000000E+01 7.7000000E+01
SG     8.1800000E-01 3.0000000E-01
TB     -7.8450000E+01 -1.6145000E+02
OMEGA  4.5723553E-01 4.5723553E-01
OMEGB  7.7796074E-02 7.7796074E-02
VSHIFT 0.0000000E+00 0.0000000E+00
VISVC  9.4000000E-02 9.9000000E-02
BIN    1.0300000E-01
TRES   20 20 500 40
PHASEID GAS
CW 4.35E-07
REFPW 101.0
SOLUBILITY HENRY
HENRYC 1.9510547E+05 0.0
REFPH  9.4000000E+03 9.4000000E+03
VINFINITY 3.5089333E-02 3.5242646E-02
DERIVATIVEMETHOD NUMERALL
DIFFC-AQU 2.0E-05 0.0
YAQU-RATE-CUTOFF 1.0E-4 100.0
DER-CHEM-EQUIL ANALYTICAL
DER-REACT-RATE ANALYTICAL
ACTIVITY-MODEL B-DOT
SALINITY 0.1
AQUEOUS-DENSITY ROWE-CHOU
AQUEOUS-VISCOSITY KESTIN
NC-AQUEOUS 7
COMPNAME-AQUEOUS
'H+' 'Ca++' 'SiO2(aq)' 'Al+++' 'OH-' 'HCO3-' 'CO3--'
MW-AQUEOUS
1.0079
40.0800
60.0843
26.9815
17.0073
61.0171
60.0092
ION-SIZE-AQUEOUS
9.0 6.0 -0.5 9.0 3.5 4.5 4.5
CHARGE-AQUEOUS
1 2 0 3 -1 -1 -2
NC-MINERAL 3
COMPNAME-MINERAL
```

```
'CALCITE' 'KAOLINIT' 'ANORTHIT'
MW-MINERAL
100.0869
258.1616
278.2082
MASSDENSITY-MINERAL
2710.00
2410.00
2740.00
N-RATE-REACT 3
N-CHEM-EQUIL 3
**REACTION NO.   1: (OH-) + (H+) = H2O
STOICHIOMETRY
    0.000    0.000    1.000   -1.000    0.000
    0.000    0.000   -1.000    0.000    0.000
    0.000    0.000    0.000
LOG-CHEM-EQUIL-COEFS
1.492816E+01 -4.187619E-02  1.973673E-04 -5.549507E-07  7.581087E-10
**REACTION NO.   2: CO2(aq) + H2O = (H+) + (HCO3-)
STOICHIOMETRY
   -1.000    0.000   -1.000    1.000    0.000
    0.000    0.000    0.000    1.000    0.000
    0.000    0.000    0.000
LOG-CHEM-EQUIL-COEFS
 -6.549243E+00  9.001740E-03 -1.021150E-04  2.761879E-07 -3.561421E-10
**REACTION NO.   3: (CO3--) + (H+) = (HCO3-)
STOICHIOMETRY
    0.000    0.000    0.000   -1.000    0.000
    0.000    0.000    0.000    1.000    -1.000
    0.000    0.000    0.000
LOG-CHEM-EQUIL-COEFS
1.060796E+01 -1.276757E-02  1.202580E-04 -3.017310E-07  2.693718E-10
**REACTION NO. 4:  CALCITE + H+ = (Ca++) + (HCO3-)
STOICHIOMETRY
0 0 0 -1 1 0 0 0 1 0
-1 0 0
SPEC-REACT-SURFACE-AREA 1.0E+04
MIN-REACT-SURFACE-AREA 1.0
ACTIVATION-ENERGY 41870.0
REF-TEMP-RATE-CONST 25.0
LOG-CHEM-EQUIL-COEFS
2.068889E+00 -1.426678E-02 -6.060961E-06  1.459215E-07 -4.189284E-10
LOG-TST-RATE-CONSTANT -8.79588
**REACTION NO. 5:  KAOLINITE + 6(H+) = 5(H2O) + 2SiO2(aq) + 2(Al+++)
STOICHIOMETRY
0 0 5 -6 0 2 2 0 0 0
0 -1 0
SPEC-REACT-SURFACE-AREA 1.0E+05
MIN-REACT-SURFACE-AREA 0.0
ACTIVATION-ENERGY 62760.0
REF-TEMP-RATE-CONST 25.0
LOG-CHEM-EQUIL-COEFS
  9.729544E+00 -9.889756E-02  2.915576E-04 -3.270281E-07 -3.311012E-10
LOG-TST-RATE-CONSTANT -13.00
**REACTION NO. 6:  ANORTHITE + 8H+ = 4(H2O) + (Ca++) + 2[SiO2(aq)] + 2(Al++)
STOICHIOMETRY
0 0 4 -8 1 2 2 0 0 0
0 0 -1
SPEC-REACT-SURFACE-AREA 1.0E+04
MIN-REACT-SURFACE-AREA 1.0
```

```
ACTIVATION-ENERGY 67830.0
REF-TEMP-RATE-CONST 25.0
LOG-CHEM-EQUIL-COEFS
3.174573E+01 -2.012538E-01  5.958903E-04 -9.041158E-07  9.153776E-11
LOG-TST-RATE-CONSTANT -12.0
ANNIH-MATRIX
 1.0   0.0   0.0   0.0   0.0   0.0   0.0   0.0   1.0   1.0
 0.0   1.0   0.0   0.0   0.0   0.0   0.0   0.0   0.0   0.0
 0.0   0.0   1.0   0.0   0.0   0.0   0.0   1.0   1.0   1.0
 0.0   0.0   0.0   1.0   0.0   0.0   0.0  -1.0  -1.0  -2.0
 0.0   0.0   0.0   0.0   1.0   0.0   0.0   0.0   0.0   0.0
 0.0   0.0   0.0   0.0   0.0   1.0   0.0   0.0   0.0   0.0
 0.0   0.0   0.0   0.0   0.0   0.0   1.0   0.0   0.0   0.0
OGW_FLASH NO_H2OVAP
TRACE-COMP 2
PERM-VS-POR *K-C
Rf_exponent 3
**-------------------------------- Rock Fluid --------------------------------**

ROCKFLUID
RPT 1 DRAINAGE
** Sw       krw      krow      Pcow
SWT
0.000000  0.000000  0.000000  0.000000
0.050000  0.000000  0.000000  0.000000
0.100000  0.000000  0.000000  0.000000
0.150000  0.000010  0.000000  0.000000
0.200000  0.000150  0.000000  0.000000
0.250000  0.000770  0.000000  0.000000
0.300000  0.002440  0.000000  0.000000
0.350000  0.005950  0.000000  0.000000
0.400000  0.012350  0.000000  0.000000
0.450000  0.022870  0.000000  0.000000
0.500000  0.039020  0.000000  0.000000
0.550000  0.062500  0.000000  0.000000
0.600000  0.095260  0.000000  0.000000
0.650000  0.139470  0.000000  0.000000
0.700000  0.197530  0.000000  0.000000
0.750000  0.272070  0.000000  0.000000
0.800000  0.365950  0.000000  0.000000
0.850000  0.482250  0.000000  0.000000
0.900000  0.624300  0.000000  0.000000
0.950000  0.795620  0.000000  0.000000
1.000000  1.000000  0.000000  0.000000
** Sg       krg      krog      Pcog
SGT
0.000000  0.000000  0.000000  0.000000
0.050000  0.000080  0.000000  0.000000
0.100000  0.000680  0.000000  0.000000
0.150000  0.002330  0.000000  0.000000
0.200000  0.005610  0.000000  0.000000
0.250000  0.011140  0.000000  0.000000
0.300000  0.019610  0.000000  0.000000
0.350000  0.031740  0.000000  0.000000
0.400000  0.048370  0.000000  0.000000
0.450000  0.070420  0.000000  0.000000
0.500000  0.098940  0.000000  0.000000
0.550000  0.136180  0.000000  0.000000
0.600000  0.180650  0.000000  0.000000
0.650000  0.232750  0.000000  0.000000
```

```
0.700000  0.307520  0.000000  0.000000
0.750000  0.395200  0.000000  0.000000
0.800000  0.506570  0.000000  0.000000
0.850000  0.655620  0.000000  0.000000
0.900000  0.954430  0.000000  0.000000
0.950000  0.977220  0.000000  0.000000
1.000000  1.000000  0.000000  0.000000
KROIL STONE2 SWSG

**---------------------------------- Initial ----------------------------------**

INITIAL
VERTICAL BLOCK_CENTER WATER_GAS
ZOIL   0.001 0.999
ZGAS
0.0000001 .9999999
REFPRES
101.
REFDEPTH
0.
DWGC
1.
SWOC
0.999
MOLALITY-AQUEOUS
1.000000D-07   9.118492D-01
2.345433D-08   2.317806D-11   5.456322D-06   2.489299D-02   1.170273D-05
VOLUMEFRACTION-MINERAL
0.0088 0.0176 0.0088

**---------------------------------- Numerical ---------------------------------**

NUMERICAL
NORTH 80
ITERMAX 200
ITERMIN 1
DTMIN .000000000001
NORM PRESS 125
NORM SATUR 0.2
NORM GMOLAR 0.45
NORM AQUEOUS 0.45
MAXCHANGE PRESS 250
MAXCHANGE SATUR 0.4
MAXCHANGE GMOLAR 0.9
CONVERGE MAXRES LOOSER
CONVERGE CEQAQU 1
CONVERGE CEQCHE 1
CONVERGE CEQMNR 1
DTMAX 365
NCHECK-CEQ 5
PRECC 0.05
PIVOT ON

**------------------------------ Well/Date Data -----------------------------**

RUN                                     INCOMP  SOLVENT  1.  0.
DATE 2000 01 01                         OPERATE  MAX  STG  10.  CONT
DTWELL 0.01                             GEOMETRY  I  0.2  0.37  1.  0.
WELL  'Injector-1'                      PERF  GEO  'Injector-1'
INJECTOR 'Injector-1'                   2 14 19  1.  OPEN   FLOW-FROM 'SURFACE'
```

```
OPEN 'Injector-1'

WELL  'Injector-2'
INJECTOR 'Injector-2'
INCOMP  SOLVENT  1.  0.
OPERATE  MAX  STG  10.  CONT
GEOMETRY  I  0.2  0.37  1.  0.
PERF  GEO  'Injector-2'
6 13 19  1.  OPEN   FLOW-FROM 'SURFACE'
OPEN 'Injector-2'

WELL  'Injector-3'
INJECTOR 'Injector-3'
INCOMP  SOLVENT  1.  0.
OPERATE  MAX  STG  10.  CONT
GEOMETRY  I  0.2  0.37  1.  0.
PERF  GEO  'Injector-3'
10 12 19  1.  OPEN  FLOW-FROM 'SURFACE'
OPEN 'Injector-3'
WELL  'Injector-4'
INJECTOR 'Injector-4'
INCOMP  SOLVENT  1.  0.
OPERATE  MAX  STG  10.  CONT
GEOMETRY  I  0.2  0.37  1.  0.
PERF  GEO  'Injector-4'
14 11 19  1.  OPEN  FLOW-FROM 'SURFACE'
OPEN 'Injector-4'

WELL  'Injector-5'
INJECTOR 'Injector-5'
INCOMP  SOLVENT  1.  0.
OPERATE  MAX  STG  10.  CONT
GEOMETRY  I  0.2  0.37  1.  0.
PERF  GEO  'Injector-5'
18 10 19  1.  OPEN  FLOW-FROM  SURFACE'
OPEN 'Injector-5'

WELL  'Brine-Injector-1'
INJECTOR 'Brine-Injector-1'
INCOMP  AQUEOUS  0.0  0.  0.5  0.  0.  0.
0.5  0  0.
OPERATE  MAX  STW  10  CONT
GEOMETRY  I  0.2  0.37  1.  0.
PERF  GEO  'Brine-Injector-1'
2 3 11  1.  OPEN    FLOW-FROM 'SURFACE'
OPEN 'Brine-Injector-1'

WELL  'Brine-Injector-2'
INJECTOR 'Brine-Injector-2'
INCOMP  AQUEOUS  0.0  0.  0.5  0.  0.  0.
0.5  0  0.
OPERATE  MAX  STW  10  CONT
GEOMETRY  I  0.2  0.37  1.  0.
PERF  GEO  'Brine-Injector-2'
2 3 13  1.  OPEN    FLOW-FROM 'SURFACE'
OPEN 'Brine-Injector-2'

WELL  'Brine-Injector-3'
INJECTOR 'Brine-Injector-3'
INCOMP  AQUEOUS  0.0  0.  0.5  0.  0.  0.
0.5  0  0.
OPERATE  MAX  STW  10  CONT
GEOMETRY  I  0.2  0.37  1.  0.
PERF  GEO  'Brine-Injector-3'
2 3 15  1.  OPEN    FLOW-FROM 'SURFACE'
OPEN 'Brine-Injector-3'

WELL  'Brine-Injector-4'
INJECTOR 'Brine-Injector-4'
INCOMP  AQUEOUS  0.0  0.  0.5  0.  0.  0.
0.5  0  0.
OPERATE  MAX  STW  10  CONT
GEOMETRY  I  0.2  0.37  1.  0.
PERF  GEO  'Brine-Injector-4'
2 3 17  1.  OPEN    FLOW-FROM 'SURFACE'
OPEN 'Brine-Injector-4'

WELL  'Brine-Injector-5'
INJECTOR 'Brine-Injector-5'
INCOMP  AQUEOUS  0.0  0.  0.5  0.  0.  0.
0.5  0  0.
OPERATE  MAX  STW  10  CONT
GEOMETRY  I  0.2  0.37  1.  0.
PERF  GEO  'Brine-Injector-5'
2 3 19  1.  OPEN    FLOW-FROM 'SURFACE'
OPEN 'Brine-Injector-5'

WELL  'Prod 1'
PRODUCER  'Prod 1'
OPERATE  MIN  BHP 984.3
GEOMETRY  K  0.2  0.37  1.  0.
PERF  GEO  'Prod 1'
1 14 1  1.  OPEN    FLOW-TO  'SURFACE'
OPEN 'Prod 1'

WELL  'Prod 2'
PRODUCER  'Prod 2'
OPERATE  MIN  BHP 984.3
GEOMETRY  K  0.2  0.37  1.  0.
PERF  GEO  'Prod 2'
4 13 1  1.  OPEN    FLOW-TO  'SURFACE'
OPEN 'Prod 2'

WELL  'Prod 3'
PRODUCER  'Prod 3'
OPERATE  MIN  BHP 984.3
GEOMETRY  K  0.2  0.37  1.  0.
PERF  GEO  'Prod 3'
8 12 1  1.  OPEN    FLOW-TO  'SURFACE'
OPEN 'Prod 3'

WELL  'Prod 4'
PRODUCER  'Prod 4'
OPERATE  MIN  BHP 984.3
GEOMETRY  K  0.2  0.37  1.  0.
PERF  GEO  'Prod 4'
12 11 1  1.  OPEN    FLOW-TO  'SURFACE'
OPEN 'Prod 4'
```

```
WELL  'Prod 5'
PRODUCER  'Prod 5'
OPERATE  MIN  BHP 984.3
GEOMETRY  K  0.2  0.37  1.  0.
PERF  GEO  'Prod 5'
16 10 1  1.  OPEN    FLOW-TO  'SURFACE'
OPEN 'Prod 5'

WELL  'Prod 6'
PRODUCER  'Prod 6'
OPERATE  MIN  BHP 984.3
GEOMETRY  K  0.2  0.37  1.  0.
PERF  GEO  'Prod 6'
20 10 1  1.  OPEN    FLOW-TO  'SURFACE'
OPEN 'Prod 6'


DATE 2000 01 15      DATE 2007 01 01      DATE 2160 01 01      DATE 2340 01 01
DATE 2000 02 29      DATE 2008 01 01      DATE 2170 01 01      DATE 2350 01 01
DATE 2000 03 31      DATE 2009 01 01      DATE 2180 01 01      DATE 2360 01 01
DATE 2000 04 30      DATE 2010 01 01      DATE 2190 01 01      DATE 2370 01 01
DATE 2000 05 31      DATE 2020 01 01      DATE 2200 01 01      DATE 2380 01 01
DATE 2000 06 30      DATE 2030 01 01      DATE 2210 01 01      DATE 2390 01 01
DATE 2000 07 31      DATE 2040 01 01      DATE 2220 01 01      DATE 2400 01 01
DATE 2000 08 31      DATE 2050 01 01      DATE 2230 01 01      DATE 2410 01 01
DATE 2000 09 30      DATE 2060 01 01      DATE 2240 01 01      DATE 2420 01 01
DATE 2000 10 31      DATE 2070 01 01      DATE 2250 01 01      DATE 2430 01 01
DATE 2000 11 30      DATE 2080 01 01      DATE 2260 01 01      DATE 2440 01 01
DATE 2001 01 01      DATE 2090 01 01      DATE 2270 01 01      DATE 2450 01 01
DATE 2001 06 01      DATE 2100 01 01      DATE 2280 01 01      DATE 2460 01 01
DATE 2002 01 01      DATE 2110 01 01      DATE 2290 01 01      DATE 2470 01 01
DATE 2003 01 01      DATE 2120 01 01      DATE 2300 01 01      DATE 2480 01 01
DATE 2004 01 01      DATE 2130 01 01      DATE 2310 01 01      DATE 2490 01 01
DATE 2005 01 01      DATE 2140 01 01      DATE 2320 01 01      DATE 2500 01 01
DATE 2006 01 01      DATE 2150 01 01      DATE 2330 01 01      STOP
```

B.2 CO_2-dissolved Groundwater Case

Input/Output, Grid, Fluid model, Rock fluid, Initial, and Numerical sections are same as in Deep Crustal CO_2 case.

```
**------------------------------ Well/Date Data -------------------------------**

RUN                                     GEOMETRY  I  0.2  0.37  1.  0.
DATE 2000 01 01                         PERF  GEO  'Injector-2'
DTWELL 0.01                             2 3 13  1.  OPEN    FLOW-FROM  'SURFACE'
                                        OPEN 'Injector-2'
WELL  'Injector-1'
INJECTOR 'Injector-1'                   WELL  'Injector-3'
INCOMP  AQUEOUS  0.1  0.  0.45  0.  0.  INJECTOR 'Injector-3'
0.  0.45  0  0.                         INCOMP  AQUEOUS  0.1  0.  0.45  0.  0.
OPERATE  MAX  STW  2  CONT              0.  0.45  0  0.
GEOMETRY  I  0.2  0.37  1.  0.          OPERATE  MAX  STW  2  CONT
PERF  GEO  'Injector-1'                 GEOMETRY  I  0.2  0.37  1.  0.
2 3 11  1.  OPEN    FLOW-FROM  'SURFACE'PERF  GEO  'Injector-3'
OPEN 'Injector-1'                       2 3 15  1.  OPEN    FLOW-FROM  'SURFACE'
                                        OPEN 'Injector-3'
WELL  'Injector-2'
INJECTOR 'Injector-2'                   WELL  'Injector-4'
INCOMP  AQUEOUS  0.1  0.  0.45  0.  0.  INJECTOR 'Injector-4'
0.  0.45  0  0.                         INCOMP  AQUEOUS  0.1  0.  0.45  0.  0.
OPERATE  MAX  STW  2  CONT              0.  0.45  0  0.
```

```
OPERATE  MAX  STW  2  CONT
GEOMETRY  I  0.2  0.37  1.  0.
PERF  GEO  'Injector-4'
2 3 17  1.  OPEN    FLOW-FROM  'SURFACE'
OPEN 'Injector-4'

WELL  'Injector-5'
INJECTOR 'Injector-5'
INCOMP  AQUEOUS  0.1  0.  0.45  0.  0.
0.  0.45  0  0.
OPERATE  MAX  STW  2  CONT
GEOMETRY  I  0.2  0.37  1.  0.
PERF  GEO  'Injector-5'
2 3 19  1.  OPEN    FLOW-FROM  'SURFACE'
OPEN 'Injector-5'

WELL  'Prod 1'
PRODUCER  'Prod 1'
OPERATE  MIN  BHP 984.3
GEOMETRY  K  0.2  0.37  1.  0.
PERF  GEO  'Prod 1'
1 14 1  1.  OPEN    FLOW-TO  'SURFACE'
OPEN 'Prod 1'

WELL  'Prod 2'
PRODUCER  'Prod 2'
OPERATE  MIN  BHP 984.3
GEOMETRY  K  0.2  0.37  1.  0.
PERF  GEO  'Prod 2'
4 13 1  1.  OPEN    FLOW-TO  'SURFACE'
OPEN 'Prod 2'

WELL  'Prod 3'
PRODUCER  'Prod 3'
OPERATE  MIN  BHP 984.3
GEOMETRY  K  0.2  0.37  1.  0.
PERF  GEO  'Prod 3'
8 12 1  1.  OPEN    FLOW-TO  'SURFACE'
OPEN 'Prod 3'

WELL  'Prod 4'
RODUCER  'Prod 4'
OPERATE  MIN  BHP 984.3
GEOMETRY  K  0.2  0.37  1.  0.
PERF  GEO  'Prod 4'
12 11 1  1.  OPEN    FLOW-TO  'SURFACE'
OPEN 'Prod 4'

WELL  'Prod 5'
PRODUCER  'Prod 5'
OPERATE  MIN  BHP 984.3
GEOMETRY  K  0.2  0.37  1.  0.
PERF  GEO  'Prod 5'
16 10 1  1.  OPEN    FLOW-TO  'SURFACE'
OPEN 'Prod 5'

WELL  'Prod 6'
PRODUCER  'Prod 6'
OPERATE  MIN  BHP 984.3
GEOMETRY  K  0.2  0.37  1.  0.
PERF  GEO  'Prod 6'
20 10 1  1.  OPEN    FLOW-TO  'SURFACE'
OPEN 'Prod 6'


DATE 2000 01 15     DATE 2007 01 01     DATE 2160 01 01     DATE 2340 01 01
DATE 2000 02 29     DATE 2008 01 01     DATE 2170 01 01     DATE 2350 01 01
DATE 2000 03 31     DATE 2009 01 01     DATE 2180 01 01     DATE 2360 01 01
DATE 2000 04 30     DATE 2010 01 01     DATE 2190 01 01     DATE 2370 01 01
DATE 2000 05 31     DATE 2020 01 01     DATE 2200 01 01     DATE 2380 01 01
DATE 2000 06 30     DATE 2030 01 01     DATE 2210 01 01     DATE 2390 01 01
DATE 2000 07 31     DATE 2040 01 01     DATE 2220 01 01     DATE 2400 01 01
DATE 2000 08 31     DATE 2050 01 01     DATE 2230 01 01     DATE 2410 01 01
DATE 2000 09 30     DATE 2060 01 01     DATE 2240 01 01     DATE 2420 01 01
DATE 2000 10 31     DATE 2070 01 01     DATE 2250 01 01     DATE 2430 01 01
DATE 2000 11 30     DATE 2080 01 01     DATE 2260 01 01     DATE 2440 01 01
DATE 2001 01 01     DATE 2090 01 01     DATE 2270 01 01     DATE 2450 01 01
DATE 2001 06 01     DATE 2100 01 01     DATE 2280 01 01     DATE 2460 01 01
DATE 2002 01 01     DATE 2110 01 01     DATE 2290 01 01     DATE 2470 01 01
DATE 2003 01 01     DATE 2120 01 01     DATE 2300 01 01     DATE 2480 01 01
DATE 2004 01 01     DATE 2130 01 01     DATE 2310 01 01     DATE 2490 01 01
DATE 2005 01 01     DATE 2140 01 01     DATE 2320 01 01     DATE 2500 01 01
DATE 2006 01 01     DATE 2150 01 01     DATE 2330 01 01     STOP
```

B.3 Diversion of CO_2 Flow Case

Fluid model, Rock fluid, and Initial sections are same as in Deep Crustal CO_2 case.

```
**------------------------------ Input/output -------------------------------**

FILENAMES OUTPUT SRFOUT RESTARTOUT INDEXOUT MAINRESULTSOUT
INUNIT SI
INTERRUPT INTERACTIVE
XDR ON
MAXERROR  20
RANGECHECK ON
WRST 365
WPRN WELL TIME
WPRN GRID TIME
WPRN ITER ALL
WPRN ITER MATRIX
WSRF WELL 1
WSRF GRID TIME
OUTSRF WELL PSPLIT
OUTPRN WELL ALL
OUTPRN RES NONE
OUTPRN GRID MINERAL 'ANORTHIT' MINERAL 'CALCITE' MINERAL 'KAOLINIT' MOLALITY
'CO2' POROS SOLID VELOCRC permeff permint perm rfo rfg rfw kro krg krw
OUTSRF GRID DENG DENW DPORMNR MINERAL 'ANORTHIT' MINERAL 'CALCITE' MINERAL
'KAOLINIT' MOLALITY 'Al+++' MOLALITY 'CO2' MOLALITY 'CO3--' MOLALITY 'Ca++'
MOLALITY 'H+' MOLALITY 'HCO3-' MOLALITY 'OH-' MOLALITY 'SiO2(aq)' PH POROS PRES
SG SO SW TEMP VELOCRC W 'C1' W 'CO2' X 'C1' X 'CO2' Y 'C1' Y 'CO2' Z 'C1' Z
'CO2' rfo rfg rfw
OUTSRF WELL GHGAQU
            GHGGAS
            GHGSCRIT
            GHGMNR
            GHGSOL
            GHGLIQ
OUTSRF RES ALL
DIARY  CHANGES-UNCONV
RESULTS XOFFSET           0.0000
RESULTS YOFFSET           0.0000
RESULTS ROTATION          0.0000
RESULTS AXES-DIRECTIONS 1.0 -1.0 1.0

**---------------------------------- Grid ---------------------------------**

GRID CART 20 9 1
KDIR DOWN
DI CON 10
DJ CON 10
DK CON 10
NULL CON 1
POR CON 0.001
PERMI CON 25
PERMJ EQUALSI
PERMK EQUALSI
PINCHOUTARRAY CON 1
CPOR MATRIX   1.E-08
PRPOR MATRIX   1000.


**----------------------------Infinite acting boundary-----------------------**

VOLMOD IJK 1 1 1 30000       20 2 1 30000                20 5 1 30000
1 9 1 30000                  20 3 1 30000                20 6 1 30000
20 1 1 30000                 20 4 1 30000                20 7 1 30000
```

```
20 8 1 30000
20 9 1 30000
2 1 1 30000
3 1 1 30000
4 1 1 30000
5 1 1 30000
6 1 1 30000
7 1 1 30000
8 1 1 30000
9 1 1 30000
10 1 1 30000
11 1 1 30000
12 1 1 30000
13 1 1 30000
14 1 1 30000
15 1 1 30000
16 1 1 30000
17 1 1 30000
18 1 1 30000
19 1 1 30000
2 9 1 30000
3 9 1 30000
4 9 1 30000
5 9 1 30000
6 9 1 30000
7 9 1 30000
8 9 1 30000
9 9 1 30000
10 9 1 30000
11 9 1 30000
12 9 1 30000
13 9 1 30000
14 9 1 30000
15 9 1 30000
16 9 1 30000
17 9 1 30000
18 9 1 30000
19 9 1 30000
**---------------------------------- Numerical -------------------------------**

NUMERICAL
NORTH 80
ITERMAX 200
ITERMIN 1
DTMIN .000000001
norm unknown
DTMAX 60
PRECC 0.5
SDEGREE 3
PIVOT *ON

**---------------------------------- Recurrent -------------------------------**

RUN
DATE 2000 01 01
DTWELL 0.01
WELL  'Injector-1'
INJECTOR 'Injector-1'
INCOMP  AQUEOUS  0.2  0.  0.4  0.  0.  0
0.4  0  0.
OPERATE  MAX  STW  .1  CONT
GEOMETRY  I  0.2  0.37  1.  0.
PERF  GEO  'Injector-1'
1 5 1  1.  OPEN    FLOW-FROM  'SURFACE'
OPEN 'Injector-1'

WELL  'Prod 1'
PRODUCER  'Prod 1'
OPERATE  MIN  BHP 150.1
GEOMETRY  K  0.2  0.37  1.  0.
PERF  GEO  'Prod 1'
20 1 1  1.  OPEN    FLOW-TO  'SURFACE'
OPEN 'Prod 1'

WELL  'Prod 2'
PRODUCER  'Prod 2'
OPERATE  MIN  BHP 150.1
GEOMETRY  K  0.2  0.37  1.  0.
PERF  GEO  'Prod 2'
20 2 1  1.  OPEN    FLOW-TO  'SURFACE'
OPEN 'Prod 2'

WELL  'Prod 3'
PRODUCER  'Prod 3'
OPERATE  MIN  BHP 150.1
GEOMETRY  K  0.2  0.37  1.  0.
PERF  GEO  'Prod 3'
20 3 1  1.  OPEN    FLOW-TO  'SURFACE'
OPEN 'Prod 3'

WELL  'Prod 4'
PRODUCER  'Prod 4'
OPERATE  MIN  BHP 150.1
GEOMETRY  K  0.2  0.37  1.  0.
PERF  GEO  'Prod 4'
20 4 1  1.  OPEN    FLOW-TO  'SURFACE'
OPEN 'Prod 4'

WELL  'Prod 5'
PRODUCER  'Prod 5'
OPERATE  MIN  BHP 150.1
GEOMETRY  K  0.2  0.37  1.  0.
PERF  GEO  'Prod 5'
20 5 1  1.  OPEN    FLOW-TO  'SURFACE'
OPEN 'Prod 5'

WELL  'prod 6'
PRODUCER  'prod 6'
OPERATE  MIN  BHP 150.1
GEOMETRY  K  0.2  0.37  1.  0.
PERF  GEO  'prod 6'
20 6 1  1.  OPEN    FLOW-TO  'SURFACE'
OPEN 'prod 6'

WELL  'prod 7'
PRODUCER  'prod 7'
OPERATE  MIN  BHP 150.1
```

```
GEOMETRY  K  0.2  0.37  1.  0.
PERF  GEO  'prod 7'
20 7 1  1.  OPEN    FLOW-TO  'SURFACE'
OPEN 'prod 7'

WELL  'prod 8'
PRODUCER  'prod 8'
OPERATE  MIN  BHP 150.1
GEOMETRY  K  0.2  0.37  1.  0.
PERF  GEO  'prod 8'

DATE 2000 01 01     DATE 2006 01 01
DATE 2001 01 01     DATE 2007 01 01
DATE 2001 01 01     DATE 2008 01 01
DATE 2002 01 01     DATE 2009 01 01
DATE 2003 01 01     DATE 2010 01 01
DATE 2004 01 01     Stop
DATE 2005 01 01     **(1st run)
```

```
20 8 1  1.  OPEN    FLOW-TO  'SURFACE'
OPEN 'prod 8'

WELL  'prod 9'
PRODUCER  'prod 9'
OPERATE  MIN  BHP 150.1
GEOMETRY  K  0.2  0.37  1.  0.
PERF  GEO  'prod 9'
20 9 1  1.  OPEN    FLOW-TO  'SURFACE'
OPEN 'prod 9'

DATE 2011 01 01     DATE 2018 01 01
DATE 2012 01 01     DATE 2019 01 01
DATE 2013 01 01     DATE 2020 01 01
DATE 2014 01 01     Stop
DATE 2015 01 01     **(2nd run)
DATE 2016 01 01
DATE 2017 01 01
```

B.3.1 Percolation Model

```
Following is the MATLAB input file for the percolation model.
x=100; y=100;                       %number of pores in the x and y directions
NumOfPore=x*y;                      %total number of pores

%Pore size distribution
m=15;                               %mean of the pore size distribution in um
v=250;                              %variance of the pore size distribution
mu = log((m^2)/sqrt(v+m^2));        %mean in lognormal
sigma = sqrt(log(v/(m^2)+1));       %variance in lognormal
[M,V]= lognstat(mu,sigma);          %pore size distribution based on mu and sigma
R=lognrnd(mu,sigma,[x,y]);          %producing 10,000 pores from the distribution
R_volume=4/3*pi()*((R./10000).^3) %volume of each pore in cm^3
PV=sum(sum(R_volume));              %total pore volume in cm^3

%Pore size distribution plot visualization
figure('Color',[1 1 1]);
x = (0.0:0.02:100);
y = lognpdf(x,mu,sigma);
semilogx(x,y); grid;
xlabel('Pore diameter (micrometer)'); ylabel('p');
%Loop for the Percolation model
Num_Disconnected_Path=zeros(1,81);
calcite_gmole=zeros(1,81);
for p=1:81
calcite_gmole(p)=-0.00000001+0.00000001*p;
%calcite_gmole=[0  0.0000001 0.0000002 0.0000003 0.0000004 0.0000005 0.0000006
0.0000007 0.0000008];               %for path visualization
calcite_density=2.711;              %g/cm^3
calcite_MW=100.0869;                %g/mol
MaxCalcite=calcite_density/calcite_MW*PV; %Maximum amounts of calcite in mole
CalciteInPore(p)=calcite_gmole(p)*calcite_MW/calcite_density/NumOfPore;
%cm^3/pore
threshold = CalciteInPore(p);       %Threshold due to precipitations
Z=R_volume;
for i=1:100
    for j=1:100
if  Z(j,i)>threshold;
```

```
    Z(j,i)=1;
else
    Z(j,i)=0;
end
    end
end
[L,Num_Disconnected_Path(p)] = bwlabel(Z,4);
img = label2rgb(L);
imwrite(img,['data',num2str(p),'.jpg']); %exporting image in jpg file

%Plot NumOfDisconnectedPath vs. calcite precipitations
plot(calcite_gmole,Num_Disconnected_Path,'-');
xlabel('Calcite precipitation (gmole)');
ylabel('Number of disconnected path');
xlim([0 .0000003]);
ylim([0 100])
drawnow

%Path_Visualization graph
figure('Color',[1 1 1]);
for u=1:9
Path=imread(['data',num2str(u),'.jpg']);
subplot(3,3,u), image(Path)
title([num2str(calcite_gmole(u)),' gmole'])
axis off
end

%Calculating calcite amounts for complete disconnectivity and zero spanning path
with 500 samples
for b=1:500
R=lognrnd(mu,sigma,[x,y]);
R_volume=4/3*pi()*((R./10000).^3);
PV=sum(sum(R_volume));
Spanning_Path=200;
p=0;
while Spanning_Path>0
p=p+1;
calcite_gmole(p)=-0.00000001+0.00000001*p;
calcite_density=2.711; %g/cm^3
calcite_MW=100.0869;   %g/mol
MaxCalcite=calcite_density/calcite_MW*PV;
CalciteInPore(p)=calcite_gmole(p)*calcite_MW/calcite_density/NumOfPore;
threshold = CalciteInPore(p); %Due to mineralizations
Z=R_volume;
for i=1:100
    for j=1:100
if  Z(j,i)>threshold;
    Z(j,i)=1;
else
    Z(j,i)=0;
end
    end
end
[L,Num_Disconnected_Path(p)] = bwlabel(Z,4);
img = label2rgb(L);
A=zeros(4,100);
A(1,:)=L(1,:);
A(2,:)=L(100,:);
A(3,:)=L(:,1);
A(4,:)=L(:,100);
```

```
for r=1:100
    if A(2,r)==0
       A(2,r)=-1;
    end
    if A(4,r)==0
       A(4,r)=-1;
    end
    X(p)=sum(A(1,:)==A(2,r));
    Y(p)=sum(A(3,:)==A(4,r));
end
Spanning_Pathnew=X+Y;
Spanning_Path=Spanning_Pathnew(p);
end
Calcite_mole(b)=calcite_gmole(p);
end

%Plot histogram of the calcite precipitation
figure('Color',[1 1 1]);
s=1e-8:1e-7:1e-6;
Mean=mean(Calcite_mole);
hist(Calcite_mole,s)
xlabel('Calcite precipitations(mole)')
ylabel('Frequency')
mnlabel = sprintf('Mean -- %3.2d', Mean);
h = annotation('textbox',[.63 .75 0.1 0.1]);
set(h,'String',{mnlabel});

%Count number of plugged pores
Q=0;
Plug=sum(sum(Z==Q))
Percent_Plug=Plug/NumOfPore %percent
%plot percent of plugged pores vs. calcite precipitation
figure('Color',[1 1 1]);
plot(calcite_gmole,Percent_plug)
xlabel('Calcite precipitation (gmole)');
ylabel('Percentage of plugged pores (%)');
```

Glossary

$\hat{A}_0$	:	initial reactive surface area in m^2 / m^3 of bulk volume of rock
$\hat{A}_S$	:	initial specific reactive surface area in m^2 / m^3 of bulk volume of mineral
aq	:	aqueous phase
E_a	:	activation energy in J/mol
g	:	gas phase
K_{eq}	:	chemical equilibrium constant
k	:	permeability, mD
k^0	:	initial permeability, mD
k_β	:	rate constant of mineral reaction β
k_r	:	relative permeability
k_H	:	Henry's law constant
N_β	:	total moles of mineral β per bulk volume
P	:	pressure, kPa
p	:	partial pressure
r_β	:	reaction rate of mineral β
Q_β	:	activity production of mineral reaction β
S_s	:	super saturation index
T	:	temperature, ˚C
t	:	time, year

X	:	grid coordinate in x-direction
Y	:	grid coordinate in y-direction
Z	:	grid coordinate in z-direction
c_{ϕ}	:	rock compressibility
ρ	:	molar density
ϕ	:	porosity
ϕ^0	:	initial porosity
$\hat{\phi}$	:	porosity with the mineral precipitation/dissolution
μ	:	viscosity, cp

Bibliography

André, L., Audigane, P., Azaroual, M. and Menjoz, A., 2007. Numerical modeling of fluid-rockchemical interactions at the supercritical CO2-liquid interface during CO2 injection into a carbonate reservoir, the Dogger aquifer (Paris Basin, France). *Energy Conversion and Management*, 48, 1782-1797.

Bachu, S., Gunter, W. and Perkins, E., 1994. Aquifer disposal of CO2: hydrodynamic and mineral trapping. *Energy Conversion and Management*, 35, 269-279.

Bennion, B. and Bachu, S., 2005. Relative Permeability Characteristics for Supercritical CO2 Displacing Water in a Variety of Potential Sequestration Zones in the Western Canada Sedimentary Basin, SPE Annual Technical Conference and Exhibition. Society of Petroleum Engineers, Society of Petroleum Engineers.

Bethke, C., 2008. Geochemical and biogeochemical reaction modeling. Cambridge Univ Pr, Cambridge Univ Pr.

Calabrese, M., Masserano, F. and Blunt, M.J., 2005. Simulation of Physical-Chemical Processes During Carbon Dioxide Sequestration in Geological Structures, SPE Annual Technical Conference and Exhibition.

Cantucci, B., Montegrossi, G., Vaselli, O., Tassi, F., Quattrocchi, F. and Perkins, E.H., 2009. Geochemical modeling of CO2 storage in deep reservoirs: The Weyburn Project (Canada) case study. *Chemical Geology*, 265, 181-197.

Chalbaud, C.A., Lombard, J.-M.N., Martin, F., Robin, M., Bertin, H.J. and Egermann, P., 2007. Two Phase Flow Properties of Brine-CO2 Systems in a Carbonate Core: Influence of Wettability on Pc and kr, SPE/EAGE Reservoir Characterization and Simulation Conference. Society of Petroleum Engineers, Society of Petroleum Engineers.

Craig, B., 1996. Geochemical Reaction Modeling. Concepts and applications. Oxford University Press Inc. New York, Oxford University Press Inc. New York.

Dahle, H.K., Celia, M.A. and Majid Hassanizadeh, S., 2005. Bundle-of-tubes model for calculating dynamic effects in the capillary-pressure-saturation relationship. *Transport in porous media*, **58,** 5-22.

Delany, J. and Lundeen, S., 1990. The LLNL Thermodynamic Database. Lawrence Livermore

Deutsch, C.V. and Journel, A.G. (1992) GSLIB: Geostatistical Software Library and User's Guide.Oxford University Press, Oxford, New York, 340 pp.National Laboratory.

Druckenmiller, M.L. and Maroto-Valer, M.M., 2005. Carbon sequestration using brine of adjusted pH to form mineral carbonates. Fuel processing technology, 86, 1599-1614.

Duan, Z. and Sun, R., 2003. An improved model calculating CO2 solubility in pure water and aqueous NaCl solutions from 273 to 533 K and from 0 to 2000 bar. *Chemical Geology*, 193, 257-271.

Emberley, S., Hutcheon, I., Shevalier, M., Durocher, K., Gunter, W. and Perkins, E., 2004. Geochemical monitoring of fluid-rock interaction and CO2 storage at the Weyburn CO2-injection enhanced oil recovery site, Saskatchewan, Canada. *Energy*, 29, 1393-1401.

Gaus, I., Audigane, P., Andre, L., Lions, J., Jacquemet, N., Durst, P., Czernichowski-Lauriol, I. and Azaroual, M., 2008. Geochemical and solute transport modelling for CO2 storage, what to expect from it? *International Journal of Greenhouse Gas Control*, 2, 605-625.

Gouveia, F. and Friedmann, S., 2006. Timing and prediction of CO2 eruptions from Crystal Geyser, UT. Lawrence Livermore National Laboratory (LLNL), Livermore, CA,

Gouveia, F., Johnson, M., Leif, R. and Friedmann, S., 2005. Aerometric measurement and modeling of the mass of CO2 emissions from Crystal Geyser, Utah. Lawrence Livermore National Lab., Livermore, CA (US),

Grigg, R.B., McPherson, B.J. and Svec, R.K., 2006. Laboratory and model tests at reservoir conditions for CO2-brine-carbonate rock systems interactions, 8-11.

Gunter, W., Bachu, S. and LawVinod, D.H.S., 1996. Technical and economic feasibility of CO2 disposal in aquifers within the Alberta Sedimentary Basin, Canada. *Energy Conversion and Management*, 37, 1135-1142.

Gunter, W., Perkins, E. and Hutcheon, I., 2000. Aquifer disposal of acid gases: modelling of water-rock reactions for trapping of acid wastes. *Applied Geochemistry*, 15, 1085-1095.

Gunter, W., Wiwehar, B. and Perkins, E., 1997. Aquifer disposal of CO 2-rich greenhouse gases: Extension of the time scale of experiment for CO 2-sequestering reactions by geochemical modelling. *Mineralogy and Petrology*, 59, 121-140.

Heath, J.E., Lachmar, T.E., Evans, J.P., Kolesar, P.T. and Williams, A.P., 2009. Hydrogeochemical Characterization of Leaking, Carbon Dioxide--Charged Fault Zones in East-Central Utah, With Implications for Geologic Carbon Storage. *Geophysical monograph*, 183, 147-158.

Heidaryan, E., Enayati, M. and Mokhtari, B., 2008. Laboratory Investigations into the Reactive Transport Module of Carbon Dioxide Sequestration and Geochemical Simulation, Canadian International Petroleum Conference.

Izgec, O., Demiral, B., Bertin, H.J. and Akin, S., 2006. Experimental and Numerical Modeling of Direct Injection of CO2 Into Carbonate Formations, SPE Annual Technical Conference and Exhibition. Society of Petroleum Engineers, Society of Petroleum Engineers.

Jessen, K. and Stenby, E.H., 2005. Fluid Characterization for Miscible EOR Projects and CO2 Sequestration, SPE Annual Technical Conference and Exhibition. Society of Petroleum Engineers, Society of Petroleum Engineers.

Johnson, J.W., Nitao, J.J. and Knauss, K.G., 2004. Reactive transport modelling of CO2 storage in saline aquifers to elucidate fundamental processes, trapping mechanisms and sequestration partitioning. *Geological Society, London, Special Publications*, 233, 107.

Kampman, N., Bickle, M., Becker, J., Assayag, N. and Chapman, H., 2009. Feldspar dissolution kinetics and Gibbs free energy dependence in a CO2-enriched groundwater system, Green River, Utah. *Earth and Planetary Science Letters*, 284, 473-488.

Kang, Q., Lichtner, P.C., Viswanathan, H.S. and Abdel-Fattah, A.I., 2010. Pore Scale Modeling of Reactive Transport Involved in Geologic CO 2 Sequestration. *Transport in porous media*, 82, 197-213.

Kharaka, Y., Cole, D., Hovorka, S., Gunter, W., Knauss, K. and Freifeld, B., 2006. Gas-water-rock interactions in Frio Formation following CO2 injection: Implications for the storage of greenhouse gases in sedimentary basins. *Geology*, 34, 577.

Kharaka, Y.K. and Survey, G., 1989. SOLMINEQ. 88, A computer program for geochemical modeling of water-rock interactions. Dept. of the Interior, US Geological Survey, Dept. of the Interior, US Geological Survey.

Kumar, A., Noh, M., Pope, G., Sepehrnoori, K., Bryant, S. and Lake, L., 2004. Reservoir simulation of CO2 storage in deep saline aquifers.

Kwon, C.H., Lee, C.H. and Kang, J.W., 2010. Calculation of phase equilibrium for water+ carbon dioxide system using nonrandom lattice fluid equation of state. *Korean journal of chemical engineering*, 27, 278-283.

Li, L., Peters, C.A. and Celia, M.A., 2006. Upscaling geochemical reaction rates using pore-scale network modeling. *Advances in water resources*, 29, 1351-1370.

Li, L., Steefel, C.I. and Yang, L., 2008. Mineral dissolution kinetics at the pore scale.

Li, Y.K. and Nghiem, L.X., 1986. Phase equilibria of oil, gas and water/brine mixtures from a cubic equation of state and Henry's law. *The Canadian Journal of Chemical Engineering*, 64, 486-496.

Lindeberg, E. and Bergmo, P., 2003. The long-term fate of CO2 injected into an aquifer. *Greenhouse Gas Control Technologies*, 489-494.

Liu, F., Lu, P., Zhu, C. and Xiao, Y., 2010. Coupled reactive flow and transport modeling of CO2 sequestration in the Mt. Simon sandstone formation, Midwest USA. *International Journal of Greenhouse Gas Control*.

Mito, S., Xue, Z. and Ohsumi, T., 2008. Case study of geochemical reactions at the Nagaoka CO2 injection site, Japan. *International Journal of Greenhouse Gas Control*, 2, 309-318.

Model, R.G.T., 2005. Documentation and applications of the reactive geochemical transport model RATEQ. *US Geological Survey*, 94025.

Mohamed, I.M., He, J. and Nasr-El-Din, H.A., 2011. Permeability Change During CO2 Injection in Carbonate Aquifers: Experimental Study, SPE Americas E&P Health, Safety, Security, and Environmental Conference.

Moore, J., Stanitski, C., Jurs, P., 2008. Chemistry: the molecular science: Vol. 2. Edition. 3. Belmont, CA: Thompson.

Moore, J., Adams, M., Allis, R., Lutz, S. and Rauzi, S., 2005. Mineralogical and geochemical consequences of the long-term presence of CO2 in natural reservoirs: An example from the Springerville-St. Johns Field, Arizona, and New Mexico, USA. *Chemical Geology*, 217, 365-385.

Negahban, S., Pedersen, K.S., Sah, P., Basioni, M.A. and Azeem, J., 2010. An EoS Model for a Middle East Reservoir Fluid With an Extensive EOR PVT Data Material, Abu Dhabi International Petroleum Exhibition and Conference. Society of Petroleum Engineers, Society of Petroleum Engineers.

Nghiem, L., Sammon, P., Grabenstetter, J. and Ohkuma, H., 2004. Modeling CO2 Storage in Aquifers with a Fully-Coupled Geochemical EOS Compositional Simulator, SPE/DOE Symposium on Improved Oil Recovery.

Nicot, J.P., Oldenburg, C.M., Bryant, S.L. and Hovorka, S.D., 2009. Pressure perturbations from geologic carbon sequestration: Area-of-review boundaries and borehole leakage driving forces. *Energy Procedia*, 1, 47-54.

Nishi, Y., Ishido, T., Sugihara, M., Tosha, T., Matsushima, N. and Scott, B.J., 2000. Monitoring of geyser activity in Whakarewarewa, New Zealand.

Noh, M., Lake, L., Bryant, S. and Araque-Martinez, A., 2007. Implications of coupling fractional flow and geochemistry for CO2 injection in aquifers. *SPE Reservoir Evaluation & Engineering*, 10, 406-414.

Peng, D.-Y. and Robinson, D.B., 1976. A New Two-Constant Equation of State. *Industrial & Engineering Chemistry Fundamentals*, **15,** 59-64.

Peysson, Y., Bazin, B., Magnier, C., Kohler, E. and Youssef, S., 2011. Permeability alteration due to salt precipitation driven by drying in the context of CO2 injection. *Energy Procedia*, 4, 4387-4394.

Picot, J., Cassard, D., Maldan, F., Greffié, C. and Bodénan, F., 2011. Worldwide potential for ex-situ mineral carbonation. *Energy Procedia*, 4, 2971-2977.

Rojstaczer, S., Galloway, D., Ingebritsen, S. and Rubin, D., 2003. Variability in geyser eruptive timing and its causes: Yellowstone National Park. *Geophysical research letters*, 30, 1953.

Rosenbauer, R.J., Koksalan, T. and Palandri, J.L., 2005. Experimental investigation of CO2-brine-rock interactions at elevated temperature and pressure: Implications for CO2 sequestration in deep-saline aquifers. *Fuel processing technology*, 86, 1581-1597.

Pruess, K., Xu, T., Apps, J. and Garcia, J., 2003. Numerical Modeling of Aquifer Disposal of CO2. *SPE Journal***,** 49-60.

Sahimi, M., 1994. Applications of percolation theory. CRC, CRC.

Sander, R., 1999. Compilation of Henry's law constants for inorganic and organic species of potential importance in environmental chemistry.

Saylor, B., Matisoff, G. and Morrison, P., 2001. Geologic and geochemical evaluation of the potential for CO 2 disposal in deep saline aquifers beneath Ohio, 12.

Selley, R. C. 1998. Elements of Petroleum Geology, 2nd edition, Academic Press.

Scislewski, A. and Zuddas, P., 2010. Estimation of reactive mineral surface area during water-rock interaction using fluid chemical data. *Geochimica et Cosmochimica Acta*.

Shipton, Z.K., Evans, J.P., Kirschner, D., Kolesar, P.T., Williams, A.P. and Heath, J., 2004. Analysis of CO2 leakage through 'low-permeability'faults from natural reservoirs in the Colorado Plateau, east-central Utah. *Geological Society, London, Special Publications*, 233, 43.

Shrivastavar, A., Nghiem, L., Kohse, B. and Sammon, P., 2004. Simulation of CO EOR and Sequestration Processes With a Geochemical EOS Compositional Simulator.

Soave, G., 1972. Equilibrium constants from a modified Redlich-Kwong equation of state. *Chemical Engineering Science*, **27,** 1197-1203.

Song, Y.Q., 2010. Recent progress of nuclear magnetic resonance applications in sandstones and carbonate rocks. *Vadose Zone Journal*, **9,** 828-834.

Soong, Y., Goodman, A., McCarthy-Jones, J. and Baltrus, J., 2004. Experimental and simulation studies on mineral trapping of CO2 with brine. *Energy Conversion and Management*, 45, 1845-1859.

Spiteri, E., Juanes, R., Blunt, M.J. and Orr, F.M., 2005. Relative-Permeability Hysteresis: Trapping Models and Application to Geological CO2 Sequestration, SPE Annual Technical Conference and Exhibition. Society of Petroleum Engineers, Society of Petroleum Engineers.

Urquhart, A., Eichhubl, P., 2011. Structural controls on CO_2 leakage and diagenesis in a natural long-term carbon sequestration analogue: Little Grand Wash fault, Utah.

Vrolijk, P., Myers, R., Sweet, M.L., Shipton, Z.K., Dockrill, B., Evans, J.P., Heath, J. and Williams, A.P., 2005. Anatomy of reservoir-scale normal faults in central Utah: Stratigraphic controls and implications for fault zone evolution and fluid flow. *Interior western United States*, 6, 261.

Wellman, T.P., Grigg, R.B., McPherson, B.J., Svec, R.K. and Lichtner, P.C., 2003. Evaluation of CO2-Brine-Reservoir Rock Interaction with Laboratory Flow Tests and Reactive Transport Modeling, International Symposium on Oilfield Chemistry.

Wiebe, R. and Gaddy, V., 1940. The Solubility of Carbon Dioxide in Water at Various Temperatures from 12 to 40 and at Pressures to 500 Atmospheres. Critical Phenomena. *Journal of the American Chemical Society*, 62, 815-817.

Wigand, M., Carey, J., Schutt, H., Spangenberg, E. and Erzinger, J., 2008. Geochemical effects of CO2 sequestration in sandstones under simulated in situ conditions of deep saline aquifers. *Applied Geochemistry*, 23, 2735-2745.

Xu, T., Apps, J.A. and Pruess, K., 2001. Analysis of mineral trapping for CO2 disposal in deep aquifers.

Xu, T., Apps, J.A. and Pruess, K., 2001. Numerical simulation of CO2 disposal by mineral trapping in deep aquifers. *Applied Geochemistry*, 19, 917-936.

Yang, Q., Dong, Y. and zhou, f., 2005. Short-Term Numerical Simulation of Geological Sequestration of CO2 in the Barrow Sub-Basin, West Australia, SPE Asia Pacific Health, Safety and Environment Conference and Exhibition. Society of Petroleum Engineers, Society of Petroleum Engineers.

Zerai, B., 2005. CO2 Sequestration in Saline Aquifer: Geochemical Modeling, Reactive Transport Simulation and Single-phase Flow Experiment.

Zerai, B., Saylor, B.Z. and Matisoff, G., 2006. Computer simulation of CO2 trapped through mineral precipitation in the Rose Run Sandstone, Ohio. *Applied Geochemistry*, 21, 223-240.